



NATIONAL TECHNICAL UNIVERSITY OF ATHENS
SCHOOL OF ELECTRICAL AND COMPUTER ENGINEERING
COMMUNICATION, ELECTRONIC AND INFORMATION ENGINEERING DIVISION

Liquid Gated Graphene Field Effect Transistors for biomedical applications

DIPLOMA THESIS

of

Georgios Iliopoulos

Supervisor NTUA:

Evangelos V. Hristoforou,
Professor NTUA

Supervisor NCSR “DEMOKRITOS”:

Panagiotis Dimitrakis,
Director of research

Athens, March 2024



NATIONAL TECHNICAL UNIVERSITY OF ATHENS
SCHOOL OF ELECTRICAL AND COMPUTER ENGINEERING
COMMUNICATION, ELECTRONIC AND INFORMATION ENGINEERING DIVISION

Liquid Gated Graphene Field Effect Transistors for biomedical applications

DIPLOMA THESIS

of

Georgios Iliopoulos

Supervisor NTUA: Evangelos V. Hristoforou,
Professor NTUA

Supervisor NCSR “DEMOKRITOS”: Panagiotis Dimitrakis,
Director of research

Approved by the examination committee on 29th of March 2024.

.....
Evangelos V. Hristoforou
Professor
NTUA

.....
Emmanouel Hourdakis
Assistant Professor
NTUA

.....
Panagiotis Dimitrakis
Director of research
NCSR “DEMOKRITOS

.....
Georgios Iliopoulos

Graduate of Electrical and Computer Engineering, NTUA

Copyright © – Georgios Iliopoulos, 2024.

All rights reserved.

The copying, storage and distribution of this diploma thesis, all or part of it, is prohibited for commercial purposes. Reprinting, storage and distribution for non - profit, educational or of a research nature is allowed, provided that the source is indicated and that this message is retained. The content of this thesis does not necessarily reflect the views of the Department, the Supervisor, or the committee that approved it.

Abstract

Graphene's exceptional properties, including strength, flexibility, and electrical conductivity, have propelled it to the forefront of materials science since its isolation in 2004. Graphene field effect transistors (GFETs), and particularly those utilizing liquid gating techniques (LG-GFETs), have emerged as superb tools in biosensing and neural interface technology. This thesis explores the potential of LG-GFET array chips, taking advantage of graphene's unique properties to enable sensitive, real-time detection of biological signals. Through electrical characterization and ion sensitivity experiments the foundation for the integration of LG-GFETs to be integrated into next-generation biosensors and neural signal processing devices has been laid. The presented findings not only deepen the understanding of LG-GFETs but also propel the usage of LG-GFETs in neural cells data acquisition.

Keywords: *graphene, GFET, liquid gate, pH sensor, ion sensitivity, biosensor*

Περίληψη

Οι εξαιρετικές ιδιότητες του γραφενίου, όπως η αντοχή, η ευελιξία και η ηλεκτρική αγωγιμότητα, το έχουν οδηγήσει στο προσκήνιο της επιστήμης των υλικών από την εργαστηριακή απομόνωσή του, το 2004, μέχρι και σήμερα. Τα τρανζίστορ επίδρασης πεδίου με κανάλι γραφενίου (Graphene Field Effect Transistors – GFETs), και ιδιαίτερα αυτά που χρησιμοποιούν τεχνικές υγρής πύλης (Liquid Gate GFETs – LG-GFETs), έχουν αναδειχθεί ως βασικά εργαλεία στην τεχνολογία βιοαισθητήρων και νευρικών διεπαφών. Η παρούσα εργασία διερευνά τις δυνατότητες των τσιπ συστοιχίας LG-GFET σε αυτούς τους τομείς, αξιοποιώντας τις μοναδικές ιδιότητες του γραφενίου για να καταστεί δυνατή η ευαίσθητη ανίχνευση βιολογικών σημάτων σε πραγματικό χρόνο. Μέσω πειραμάτων ηλεκτρικού χαρακτηρισμού και ιοντικής ευαισθησίας τίθενται οι βάσεις ώστε τα LG-GFET να ενσωματωθούν σε βιοαισθητήρες επόμενης γενιάς και συσκευές λήψης νευρικών σημάτων. Τα ευρήματα που παρουσιάζονται όχι μόνο εμβαθύνουν την κατανόηση των LG-GFETs αλλά και προωθούν εξελίξεις στην χρήση LG-GFET για απόκτηση σημάτων από νευρικά κύτταρα.

Λέξεις-κλειδιά: γραφένιο, τρανζίστορ επίδρασης πεδίου γραφενίου, υγρή πύλη, αισθητήρας pH, ιοντική ευαισθησία, βιοαισθητήρας

Acknowledgements

Completing this thesis has been a journey filled with invaluable support and guidance from numerous individuals and institutions, without whom this work would not have been the same. Firstly, Professor Evangelos Hristoforou deserves a special mention for granting me the opportunity to conduct my research at NCSR "DEMOKRITOS". His enthusiasm and way of teaching has also been very inspiring for me. I would like, then, to express my gratitude to Dr. Panagiotis Dimitrakis, my research supervisor, for his unwavering guidance and introduction to the research world, laying a strong foundation for my endeavors. Moreover, I would like to thank PhD candidate Georgia Samara for her constant encouragement and support. The collaboration with the biology laboratory of Dr. Zafroula Georgoussi and Dr. Christos Karoussiotis has significantly enriched this work as it conducted the cells cultivation. Furthermore, I would like to acknowledge the INL – International Iberian Nanotechnology Laboratory for providing the samples through the ASCENT+ project. Lastly, I extend heartfelt thanks to my family and friends for their unwavering support, and a special thank you to Stefania and Ilias for sharing this academic journey with me, making it all the more enriching.

Table of Contents

Abstract	iii
Acknowledgements	vii
Table of Contents	ix
List of Figures	xi
List of Tables	xvii
List of Abbreviations	xix
Extended Greek Abstract.....	1
Main English Part	29
1 Introduction.....	29
2 Graphene	31
2.1 Graphene Structure.....	32
2.1.1 Atomic Bonds in Graphene.....	32
2.1.2 Graphene Lattice	33
2.2 Graphene Properties	35
2.2.1 Electrical Properties	35
2.2.2 Thermal Properties.....	38
2.2.3 Mechanical Properties.....	38
2.2.4 Optical Properties.....	40
2.3 Growth Mechanisms of Graphene.....	41
2.3.1 Mechanical exfoliation.....	41
2.3.2 Chemical vapor deposition	42
2.3.3 Vacuum Epitaxial Growth.....	43
3 Liquid Gated Graphene Field Effect Transistor (LG-GFET)	45
3.1 Basics of GFETs	45
3.2 Liquid gate GFETs	49
3.3 GFET applications.....	49

3.4	INL GFET chip.....	51
4	Electrical Characterization.....	55
4.1	Measurements methodology.....	55
4.1.1	Experimental Setup.....	55
4.1.2	Experimental details.....	57
4.2	INL Chip preparation	58
4.3	Characteristic GFET curves	59
4.3.1	Transfer Characteristic ($I_d - V_g$)	59
4.3.2	Output Characteristic ($I_d - V_d$)	64
4.3.3	Gate Leakage Current (I_g).....	66
4.4	Parameter Extraction	68
4.4.1	Transconductance (g_m).....	68
4.4.2	Output Conductance (g_d)	69
4.4.3	Conductance (G) and Resistance (R).....	70
4.4.4	Carrier Concentration.....	75
4.4.5	Field Effect Mobility (μ_{fe}).....	76
4.5	Measurement and time dependent behavior of GFETs	77
5	Using the INL chip as a pH sensor	81
5.1	pH sensing with LG-FETs.....	81
5.2	Experimental Process	81
6	Cells Cultivation.....	85
7	Conclusions.....	87
	Bibliography.....	89

List of Figures

Figure 2.1: Graphene (upper part) can be rolled into fullerenes (lower left), wrapped into nanotubes (lower center) and stacked into graphite (lower right) 31

Figure 2.2: (a) Electron distribution of a carbon atom, (b) electron distribution of a carbon atom after sp^2 hybridization..... 32

Figure 2.3: (a) The carbon atom's atomic structure, (b) Carbon atoms' outer electron energy levels, (c) The formation of sp^2 hybrids, (d) The crystal lattice of graphene, where A and B are carbon atoms belonging to different sub-lattices, a_1 and a_2 are unit-cell vectors, (e) Sigma bond and pi bond formed by sp^2 hybridization [9] 33

Figure 2.4: The unit cell of graphene with atoms 1 and 2, the basis vectors α_1 and α_2 and the distance between two adjacent carbon atoms (carbon - carbon) acc 33

Figure 2.5: The reciprocal lattice of monolayer graphene, where crosses indicate reciprocal lattice points, and vectors b_1 and b_2 are primitive lattice vectors. The shaded hexagon indicates the first Brillouin zone [11] 34

Figure 2.6: a) Three-dimensional energy band structure, the first Brillouin zone is shown in red, b) zoom in one Dirac point [13]..... 35

Figure 2.7 3D band structure and its projection on k_x close to K point for (a) graphene, (b) bilayer graphene, (c) trilayer graphene and (d) graphite [2] 37

Figure 2.8: Schematic diagrams of the lattice structure of monolayer (a) and bilayer (b) graphene (for bilayer graphene, a pair of higher-energy bands is also present, not shown in the diagram), (c) when an electric field ($E \perp$) is applied perpendicular to the bilayer, a bandgap is opened in bilayer graphene, whose size is modulated by the electric field. [35] 37

Figure 2.9: (a) Loading/unloading curve for a suspended graphene device [38], (b) Schematic illustration of a flexible graphene neural electrode array. In order to communicate with the data acquisition system, patterned graphene electrodes come in contact with Au contact pads. [6] (c) Schematic of a suspended graphene resonator [37] 39

Figure 2.10: Geometric characteristics of graphene lattice [14] 39

Figure 2.11: (a) Photograph of a 50-mm aperture partially covered by monolayer and bilayer graphene, (a - right upper corner) the depicted sample [39], (b) transmittance of graphene

oxide (GO) and reduced GO (graphene) at $\lambda \sim 550nm$ as a function of filtration volume [40].	40
Figure 2.12: Diagrammatic depiction of several graphene growth techniques [41].	41
Figure 2.13: (a) ‘Scotch tape’ graphene synthesis procedure [16], (b) Optical micrograph of multilayer with 1, 2, 3, and 6 layers graphene [42].	42
Figure 2.14: Schematic diagram of a typical CVD equipment [18].	42
Figure 2.15: (a) Thermal and (b) Plasma enhanced CVD diagrams [43].	43
Figure 3.1: Physical structure of the enhancement-type NMOS transistor: (a) perspective view, (b) cross section [45].	45
Figure 3.2: Structure of a GFETs: (a) back-gated, (b) top-gated [22].	46
Figure 3.3: (a) Typical transfer characteristics for two GFETs [22], (b) the change in the Fermi level of graphene with applied gate voltage.	47
Figure 3.4: The effect of $V_g > 0$ in the back gate of a GFET.	48
Figure 3.5: (a) Typical output characteristics for different V_g [22], (b) illustration of the carrier concentration beneath the top-gated region: for $V_{ds} < V_{ds, crit}$ (region I) the channel charge at the drain end begins to decrease as the minimal density point enters the channel, for $V_{ds} = V_{ds, crit}$ (region II) the minimal density point forms at the drain and for $V_{ds} > V_{ds, crit}$ (region III) an electron channel forms at the drain [25].	48
Figure 3.6: Liquid gate GFET configuration with reference gate electrode.	49
Figure 3.7: Sensing principle of GFET biosensor [29].	50
Figure 3.8: Diagram outlining the progress of biosensor development. Stage 0: Initial graphene transistor, Stage 1: Implementation of 1-Dodecanethiol (DDT) gate passivation, Stage 2: Introduction of 1 – pyrenebutyric acid succinimidyl ester (PBSE) linker immobilization, Stage 3: Functionalization with probe DNA, Stage 4: Application of ethanolamine blocking, Stage 5: Initiation of biorecognition process [46].	50
Figure 3.9: (a) representation of the implant placed on the surface of the rat's brain (b) representation of the head of a graphene implant showing a 4×4 graphene transistor array and feed lines, (c) cross section of a flexible graphene transistor with graphene between the source and drain contact that are covered by an insulating SU8 photoresist [32].	51

Figure 3.10: a) 3D illustration of the GFETs chip, b) close-up 3D illustration of the 20 GFETs, c) collage of optical microscope images showing the 20 devices with numbers indicating correspondence to pins, d) illustration of the 20 GFETs and close up of the graphene sheets, e) photograph of the chips, and f) pins to electrodes correspondence mapping. ..	52
Figure 3.11: Graphical summary of the fabrication process for production of LG-GFETs for biosensing at wafer-scale. [26].	54
Figure 4.1: HP 4155A Semiconductor Parameter Analyzer	56
Figure 4.2: Experimental setup for $I - V$ curves.....	56
Figure 4.3: (a) Micromanipulator probe station and (b) placement of the probes on the INL chip.	57
Figure 4.4: HP4284A LCR meter	57
Figure 4.5: (a) INL chip with a drop of distilled water, (b) INL chip with PDMS chamber filled with distilled water, (c) illustration of INL chip with PDMS chamber.....	58
Figure 4.6: Chemical structure of PDMS [47].....	58
Figure 4.7: The relationship between the DOS and the energy (a) in the contacts and in the graphene separately and (b) "just" at the metal/graphene interface.....	59
Figure 4.8: $I_d - V_g$ curves for V_d from 0V to 0.4V for the FET 26_20 with the polymer chamber filled (0.3ml) with distilled water.	60
Figure 4.9: $I_d - V_g$ curves for source grounded (purple line) and drain grounded (grey line)...	61
Figure 4.10: $I_d - V_g$ curves for forward and backward sweep.	61
Figure 4.11: $I_d - V_g$ curves for different gate electrodes, in (b) the curves are shifted by $V_g, dirac$ to show the same profile	62
Figure 4.12: $I_d - V_g$ curves for $V_d = 0.3V$ for the left (a) and the right FETs (b) of the chip 150191.....	63
Figure 4.13: Box charts for gate voltage (a) and drain current (b) at the Dirac point.	63
Figure 4.14: $I_d - V_g$ curves for $V_d = 0.3V$ for the left (a) and the right FETs (b) of the chip 150431.....	64
Figure 4.15: $I_d - V_g$ curves for $V_d = 0.3V$ for the left (a) and the right FETs (b) of the chip 150439.....	64
Figure 4.16: (a) $I_d - V_d$ for V_g from 0V to 1V for the FET 25_20 with the polymer chamber filled (0.3ml) with distilled water.....	65

Figure 4.17: (a) $I_d - V_d$ curve for V_g around $V_g, Dirac$, (b) $I_d - V_d$ curve for $V_g = 0.2V$, where the 3 regions of operation of a GFET are shown: I) triode region, II) unipolar saturation region and III) ambipolar saturation region [24].....	66
Figure 4.18: $I_d - V_d$ curves for $V_g = 0.4V$ for the left (a) and the right FETs (b) of the chip 150191.....	66
Figure 4.19: (a) $I_d - V_g$ curves for V_d from 0V to 0.4V for the FET 26_20 with the polymer chamber filled (0.3ml) with distilled water, (b) Leakage current during the same measurement	67
Figure 4.20: (a) $I_d - V_d$ for V_g from 0V to 1V for the FET 25_20 with the polymer chamber filled (0.3ml) with distilled water, (b) Leakage current during the same measurement ..	67
Figure 4.21: Transconductance curves of GFET 25_20 for different values of drain voltage (V_d).	69
Figure 4.22: $g_d - V_d$ curve for V_g around $V_g, Dirac$	69
Figure 4.23: $G - V_g$ curves for V_d from 0V to 0.4V.	70
Figure 4.24: Resistance curves versus gate voltage (a) and versus gate voltage $-V_g, Dirac$ (b).71	
Figure 4.25: Experimental water – graphene capacitance curve as a function of voltage for frequency 1MHz.	74
Figure 4.26: the fit [33] of eq. (4.6) to the experimental data of the resistance curve versus the gate voltage for (a) $V_d = 0.1V$ and (b) for all the measured drain voltages of the chip 150191 with the polymer chamber filled with water.	74
Figure 4.27: The extracted parameters versus drain voltage and a linear fit: (a) Contact resistance, (b)Residual carrier concentration and (c) effective mobility.	75
Figure 4.28: (a) carrier concentration of graphene due to the applied gate voltage, (b) total carrier concentration.....	76
Figure 4.29: $\mu fe - V_g$ curves	77
Figure 4.30: $I_d - V_g$ curves for recursive measurements in an unused device.	77
Figure 4.31: The under investigation device (a) before any measurements, (b) with the wet membrane right after measurements and removal of liquid and (c) with the dry membrane 1 day after the removal of the liquid.	78
Figure 4.32: The gelatinous membrane is visible on top of the water	78

Figure 4.33: $I_d - V_g$ curves, for the 5_11 device of the chip 150191, across six distinct temporal instances. 1.1: start of day 1, 1.2: end of day 1, 2: start of day 2, 3.1: start of day 3, 3.2 end of day 3 and 4: start of day 4.....	79
Figure 4.34: $I_d - V_g$ curves for forward (solid line) and backward sweep (dashed line).....	80
Figure 4.35: $I_d - V_g$ curves, for the 26_20 device of the chip 150191, across 4 days	80
Figure 5.1: (a) Stirring equipment, (b) pH meter C860.	82
Figure 5.2: Chip 150427 (a) before sampling measurements and (b) after sampling measurements, where the electrochemical etching is obvious in many spots.	83
Figure 5.3: Normalized conductance versus time for solutions of different pH values.....	84
Figure 6.1: Optical microscope images from the cultivation of Neuro-2A cells on graphene	85
Figure 6.2: Optical microscope images from the cultivation of isolated neurons from the embryonic hippocampal region.....	86

List of Tables

Table 2.1: Advantages and Disadvantages of the aforementioned graphene growth techniques

[44] 43

Table 4.1: Constants and device characteristics used for the fit of Figure 4.26..... 73

Table 4.2: Extracted Parameters from the fit presented in the curves of Figure 4.26.b..... 74

List of Abbreviations

Abbreviation	Full Description
AC	Alternating Current
AFM	Atomic Force Microscopy
CVD	Atomic Force Microscopy
DC	Direct Current
DDT	1-Dodecanethiol
DMEM	Dulbecco's Modified Eagle Medium
DNA	Deoxyribonucleic Acid
DOS	Density Of States
EDL	Electrical Double Layer
FBS	Fasting Blood Sugar
FET	Field Effect Transistor
FL	Few Layer
FLG	Few-Layer Graphene
GO	Graphene Oxide
INL	International Iberian Nanotechnology Laboratory
INN	Institute of Nanocience and Nanotechnology
ITO	Indium Tin Oxide
LG	Liquid Gate
LGFET	Liquid Gate Field Effect Transistor
MOSFET	Metal Oxide Semiconductor Field Effect Transistor
NCBI	National Center for Biotechnology Information
NCSR	National Centre for Scientific Research
NEMS	Nano Electromechanical Systems
NMOS	Negative Metal Oxide Semiconductor
OLED	Organic Light-Emitting Diode
PBSE	1 – PyreneButyric acid Succinimidyl Ester
PCB	Printed Circuit Board
PDMS	Polydimethylsiloxane

PECVD	Plasma-Enhanced Chemical Vapor Deposition
PMMA	Poly(Methyl Methacrylate)
PMOS	Positive Metal Oxide Semiconductor
SARS	Severe Acute Respiratory Syndrome
SMU	Source Measure Unit
AC	Alternating Current
AFM	Atomic Force Microscopy
CVD	Atomic Force Microscopy
DC	Direct Current
DDT	1-Dodecanethiol

Extended Greek Abstract

-This passage is an extensive summary in Greek and is not considered complete. The full text can be found in English after this summary.

-Το παρόν χωρίο αποτελεί εκτενή περίληψη στα Ελληνικά και δε θεωρείται πλήρης. Το πλήρες κείμενο παρατίθεται στη συνέχεια στα Αγγλικά.

1	Εισαγωγή	2
2	Το γραφένιο.....	3
2.1	Δομή του γραφενίου	3
2.2	Το πλέγμα του γραφενίου	4
2.3	Ιδιότητες γραφενίου	6
2.4	Τεχνικές σύνθεσης γραφενίου	8
3	Τρανζίστορ επίδρασης πεδίου γραφενίου με υγρή πύλη	10
3.1	Basics of GFETs	10
3.2	Liquid gate GFETs	13
3.3	Εφαρμογές GFETs.....	14
3.4	Το INL chip	15
4	Ηλεκτρικός Χαρακτηρισμός και Εξαγωγή Παραμέτρων.....	17
4.1	Μεθοδολογία	17
4.2	Χαρακτηριστικές καμπύλες.....	17
4.3	Εξαγωγή παραμέτρων	19
5	Χρήση του INL chip ως αισθητήρα pH.....	22
6	Καλλιέργεια Κυττάρων	24
7	Συμπεράσματα.....	26

1 Εισαγωγή

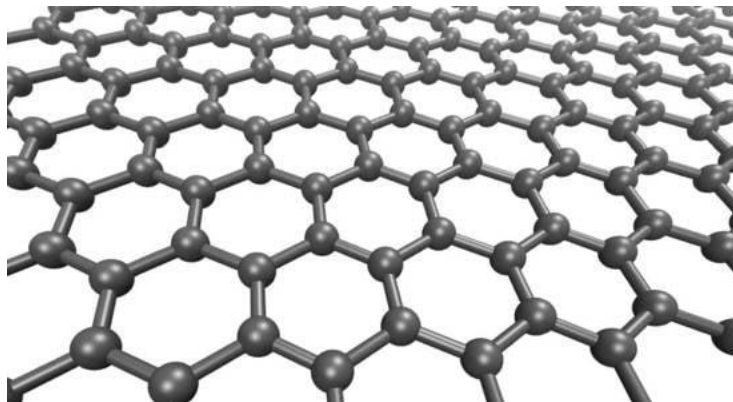
Το γραφένιο, ένα μονοατομικό στρώμα ατόμων άνθρακα διατεταγμένων σε εξαγωνικό πλέγμα, αποτελεί μία ένδειξη της δημιουργικότητας της επιστήμης των υλικών. Η ανακάλυψή του το 2004 [1] άνοιξε μια νέα εποχή δυνατοτήτων, καθώς αυτό το ατομικά λεπτό υλικό παρουσιάζει ασύλληπτες ιδιότητες που δεν συνάδουν με το μικροσκοπικό του μέγεθος. Από την αξιοσημείωτη αντοχή του, που ξεπερνά ακόμη και τον χάλυβα και το διαμάντι, μέχρι την ευκαμψία, τη διαφάνεια και την ηλεκτρική αγωγιμότητα, το γραφένιο συγκέντρωσε και εξακολουθεί να συγκεντρώνει το ενδιαφέρον των ερευνητών και των μηχανικών [2], [3], [4].

Τα τελευταία χρόνια, τα τρανζίστορ επίδρασης πεδίου από γραφένιο (Graphene Field Effect Transistors – GFETs) έχουν αναδειχθεί σε επίκεντρο της έρευνας, ιδίως στον τομέα των βιοαισθητήρων και της λήψης νευρικών σημάτων. Τα GFETs υγρής πύλης (Liquid Gate GFETs – LG-GFETs) έχουν προσελκύσει την προσοχή λόγω της ικανότητάς τους να ενσωματώνονται απρόσκοπτα με βιολογικά περιβάλλοντα, προσφέροντας διασύνδεση των ηλεκτρονικών με βιολογικά συστήματα. Αυτές οι εξελίξεις υπόσχονται όχι μόνο τη βελτίωση της υγειονομικής περίθαλψης μέσω βιοαισθητήρων, αλλά και τη βοήθεια ατόμων με αναπηρίες μέσω αισθητήρων ανάγνωσης νευρικών σημάτων, ανοίγοντας το δρόμο για τη βελτίωση της επικοινωνίας και την αποκατάσταση της κινητικής λειτουργίας [5], [6].

Η παρούσα εργασία έχει ως στόχο να εμβαθύνει στις ιδιαιτερότητες των LG-GFET, παρουσιάζοντας τις βασικές αρχές και τις πιθανές εφαρμογές τους. Μέσω του χαρακτηρισμού των LG-GFET τσιπ που αποκτήθηκαν από το Διεθνές Εργαστήριο Νανοτεχνολογίας της Ιβηρικής (International Iberian Nanotechnology Laboratory – INL), η παρούσα εργασία επιδιώκει να εξάγει τις παραμέτρους που είναι κρίσιμες για την αξιολόγηση και μελέτη της απόδοσής τους. Επιπλέον, αποδεικνύοντας την ευαισθησία τους στα ιόντα και τη συμβατότητά τους με βιολογικά διαλύματα, η έρευνα αυτή θέτει τις βάσεις για μελλοντικές εφαρμογές στον τομέα της βιοηλεκτρονικής και της τεχνολογίας νευρικών διεπαφών.

2 Το γραφένιο

Το γραφένιο είναι ένα δισδιάστατο πλέγμα ατόμων άνθρακα, ατομικού πάχους, δομημένα σε μία ισχυρή κυψελοειδή μορφή [1], [3] και έχει προσελκύσει σημαντικό ενδιαφέρον μετά την εργαστηριακή του ανακάλυψη το 2004 [1]. Με κριτήριο το πάχος του μπορεί να διακριθεί σε τρεις κατηγορίες: το μονοστρωματικό γραφένιο (πάχος ενός ατόμου άνθρακα), το διστρωματικό γραφένιο (πάχος δύο ατόμων άνθρακα) και το πολυστρωματικό γραφένιο (πάχος τριών έως εννέα ατόμων άνθρακα) [1]. Η βιοσυμβατότητα, η υψηλή αγωγιμότητα και η υψηλή μηχανική ανθεκτικότητα είναι χαρακτηριστικά του γραφενίου που το καθιστούν ερευνητικώς ενδιαφέρον υλικό [5]. Τα τελευταία χρόνια χρησιμοποιείται για τη κατασκευή τρανζίστορ, γεγονός που επιδεικνύει την ικανότητά του στην ανίχνευση δυναμικών [7].

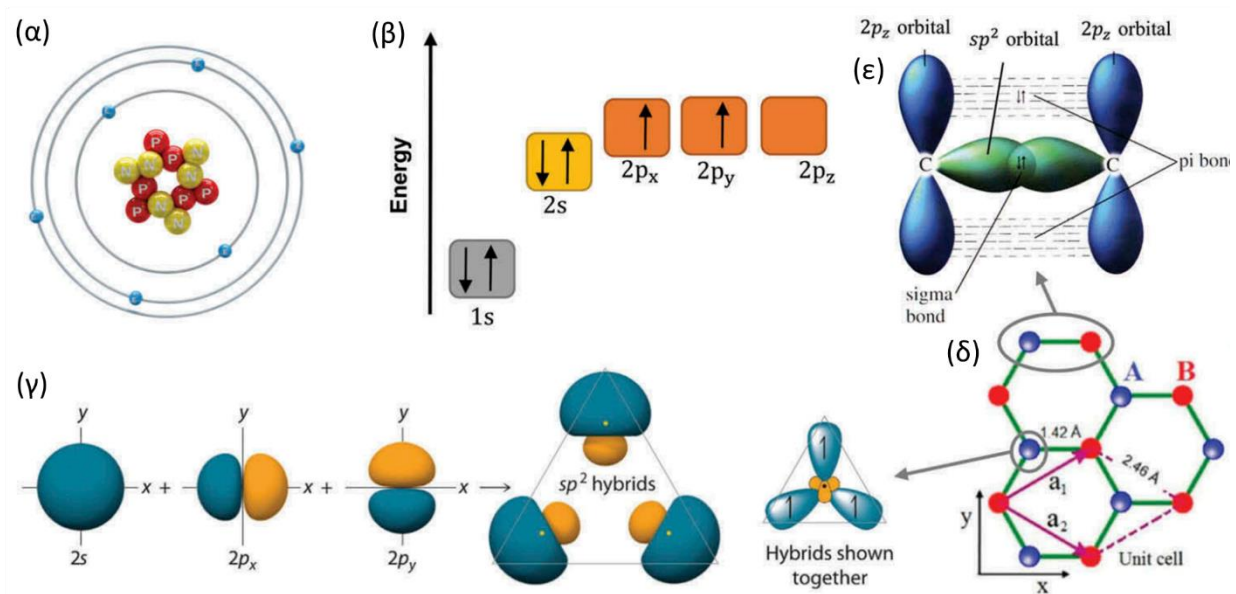


Εικόνα 0.1: γραφική αναπαράσταση γραφενίου [8]

2.1 Δομή του γραφενίου

Οι μοναδικές ιδιότητες του γραφενίου είναι απόρροια της ηλεκτρονικής δομής του που θα αναλυθεί παρακάτω. Το δομικό στοιχείο του γραφενίου, ο άνθρακας (${}_{6}^{12}\text{C}$), είναι το έκτο στοιχείο του περιοδικού πίνακα ($2^{\text{η}}$ περίοδος και $14^{\text{η}}$ ομάδα) και η κατανομή των 6 ηλεκτρονίων του είναι $1s^2 2s^2 2p_x^1 2p_y^1 2p_z^0$ (Εικόνα 0.2(α)). Παρόλο που η ενεργειακή στάθμη $2p_z$ είναι ισοδύναμη με τις στάθμες $2p_x$ και $2p_y$, για ευκολία, διατηρείται κενή. Το άτομο του άνθρακα λοιπόν έχει 4 ηλεκτρόνια σθένους τα οποία είναι ικανά να δημιουργήσουν υβριδικά τροχιακά sp , sp^2 και sp^3 . Στη περίπτωση που δημιουργηθούν sp^2 τροχιακά τότε τρία γειτονικά άτομα άνθρακα μοιράζονται ηλεκτρόνια και έτσι δημιουργείται η χαρακτηριστική κυψελοειδής μορφή του μονοστρωματικού γραφενίου. Κάθε άτομο άνθρακα μοιράζεται μεταξύ τριών κυψελίδων, συνεπώς κάθε κυψέλη έχει θεωρητικά $6/3 = 2$ ολόκληρα άτομα άνθρακα [9].

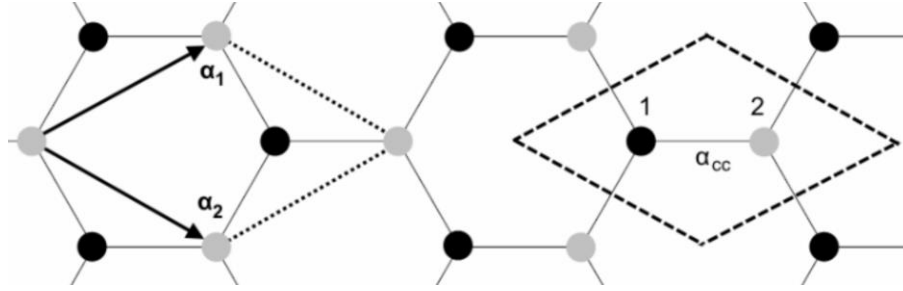
Στην Εικόνα 0.2(ε) φαίνεται πως γίνεται η ένωση μεταξύ δύο γειτονικών ατόμων άνθρακα. Αναλυτικά, δημιουργούνται ένας π δεσμός μεταξύ των $2p_z$ τροχιακών (σε επίπεδο παράλληλο με το επίπεδο του φύλλου γραφενίου) και ένας σ δεσμός μεταξύ των sp^2 υβριδικών τροχιακών. Ο σ δεσμός καταφέρει μία πολύ μικρή ατομική απόσταση μόλις $\sim 1.42\text{\AA}$ που είναι μικρότερη ακόμα και από το δεσμό των sp^3 υβριδικών τροχιακών την ένωσης άνθρακα – άνθρακα στο διαμάντι. Για αυτό το λόγο το μονοστρωματικό γραφένιο έχει πολύ καλές μηχανικές ιδιότητες. Επιπλέον οι π δεσμοί δεν επιτρέπουν να δημιουργηθούν μεγάλες van der Waals δυνάμεις μεταξύ δύο φύλλων γραφενίου στο διστρωματικό και το πολυστρωματικό γραφένιο [9]. Τέλος, στο μονοστρωματικό γραφένιο η ζώνη αγωγιμότητας και η ζώνη σθένους έχουν μηδενικό ενεργειακό κενό λόγω των π και π^* ζωνών που δημιουργούνται [10].



Εικόνα 0.2: Άτομο άνθρακα [9]

2.2 Το πλέγμα του γραφενίου

Ο sp^2 υβριδισμός, που αναλύθηκε παραπάνω, οδηγεί σε μία κυψελοειδή μορφή. Συγκεκριμένα, όπως φαίνεται στην Εικόνα 0.3, η δομή του γραφενίου περιγράφεται ως ένα εξαγωνικό πλέγμα με βάση δύο ατόμων. Η βάση του γραφενίου είναι ρόμβος και περιλαμβάνει δύο άτομα 1 και 2 τα οποία έχουν απόσταση $a_{cc} = 1.42\text{\AA}$ [11].



Εικόνα 0.3: Η μοναδιαία κυψελίδα του γραφενίου με τα άτομα 1 και 2, τα διανύσματα βάσης \vec{a}_1 και \vec{a}_2 και η απόσταση δύο γειτονικών ατόμων άνθρακα (carbon - carbon) a_{cc}

Τα δισδιάστατα διανύσματα βάσης είναι στο ίδιο επίπεδο με το γραφένιο και εκφράζονται αποκλειστικά σε ως προς τις συντεταγμένες x και y . Τα διανύσματα βάσης \vec{a}_1 και \vec{a}_2 του πλέγματος του γραφενίου μπορούν να εκφραστούν ως εξής:

$$\vec{a}_1 = \left(\frac{1}{2}a, \frac{\sqrt{3}}{2}a \right) \text{ και } \vec{a}_2 = \left(\frac{1}{2}a, -\frac{\sqrt{3}}{2}a \right) \quad (0.1)$$

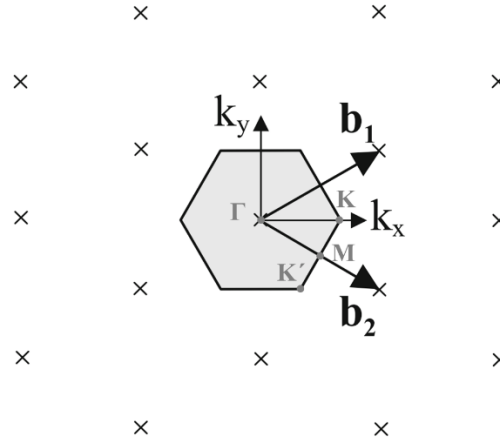
, όπου $a = |\vec{a}_1| = |\vec{a}_2| = 2.46\text{\AA}$ είναι η σταθερά πλέγματος. Η σταθερά πλέγματος είναι η απόσταση μεταξύ μοναδιαίων κελιών και διαφέρει από την απόσταση δύο γειτονικών ατόμων άνθρακα a_{cc} [11].

Τα ενεργειακά διαγράμματα εκφράζονται στον κ -χώρο, ο οποίος είναι ο μετασχηματισμός Fourier του πραγματικού χώρου, οπότε εκτός της ανάλυσης στον πραγματικό χώρο είναι χρήσιμη και η ανάλυση στον κ -χώρο [10].

Τα διανύσματα του πλέγματος ανάστροφου χώρου \vec{b}_1 και \vec{b}_2 που ικανοποιούν τις συνθήκες $\vec{a}_1 \cdot \vec{b}_1 = \vec{a}_2 \cdot \vec{b}_2 = 2\pi$ και συνθήκες $\vec{a}_1 \cdot \vec{b}_2 = \vec{a}_2 \cdot \vec{b}_1 = 0$ δίνονται από τις σχέσεις:

$$\vec{b}_1 = \left(\frac{2\pi}{a}, \frac{2\pi}{\sqrt{3}a} \right) \text{ και } \vec{b}_2 = \left(\frac{2\pi}{a}, -\frac{2\pi}{\sqrt{3}a} \right) \quad (0.2)$$

Στην Εικόνα 0.4 φαίνεται το προκύπτον πλέγμα στον ανάστροφο χώρο. Με γκρίζο χρώμα είναι χρωματισμένη η πρώτη ζώνη Brillouin [11]. Η πρώτη ζώνη Brillouin ορίζεται ως το σύνολο των σημείων του ανάστροφου χώρου που είναι πιο κοντά στο σημείο $(0, 0)$ από ό,τι σε οποιοδήποτε άλλο σημείο του ανάστροφου πλέγματος [12]. Ιδιαίτερης σημασίας για τη περιγραφή της ενεργειακής δομής είναι τα σημεία υψηλής συμμετρίας K , K' και M που φαίνονται στην Εικόνα 0.4 [11].



Εικόνα 0.4: Το αντίστροφο πλέγμα της μονοστρωματικής γραφενίου, όπου οι σταυροί υποδηλώνουν αμοιβαίο πλέγμα και τα διανύσματα b_1 και b_2 είναι πρωταρχικά διανύσματα πλέγματος. Το σκιασμένο εξάγωνο υποδεικνύει την πρώτη ζώνη Brillouin [11]

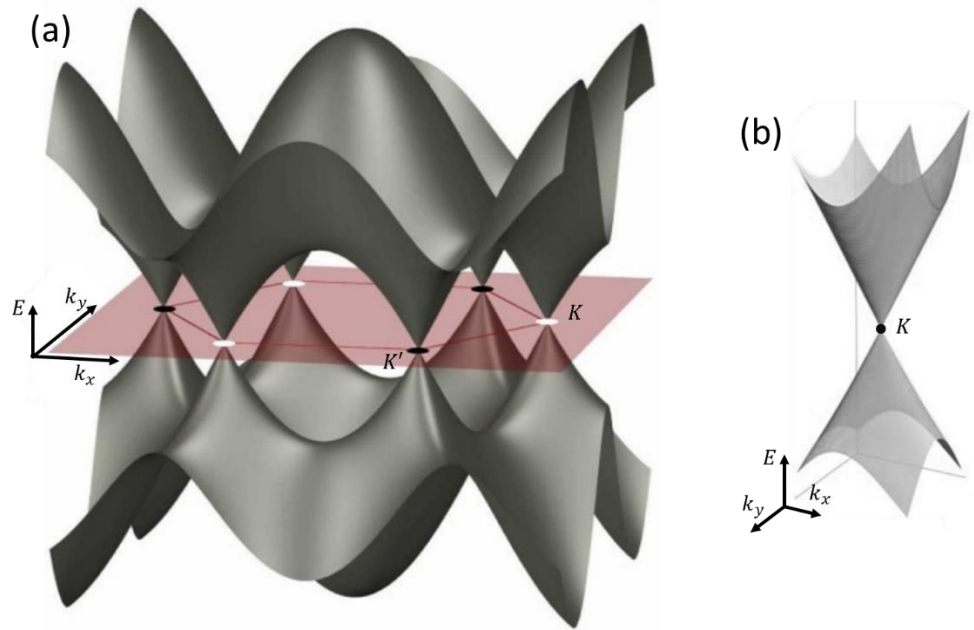
2.3 Ιδιότητες γραφενίου

Η ταχεία υιοθέτηση του γραφενίου ως υλικού ενδιαφέροντος έγκειται στο ποικίλο σύνολο ασυνήθιστων ιδιοτήτων του [4]. Το γραφένιο διαθέτει πολλές εξαιρετικές ιδιότητες όσον αφορά την οπτική διαφάνεια, την ηλεκτρική αγωγιμότητα, μηχανική αντοχή και θερμική αγωγιμότητα [3].

Η ηλεκτρονική δομή του γραφενίου μπορεί να περιγραφεί χρησιμοποιώντας μια Χαμιλτονιανή προσέγγιση ισχυρού δεσμού εξ' αιτίας των αλληλεπιδράσεων των πρώτων γειτόνων (tight-binding Hamiltonian), η οποία οδηγεί σε αναλυτικές λύσεις για την ενεργειακή του διασπορά. Το μοντέλο αυτό καταλήγει την εξής σχέση για την ενέργεια:

$$E_{\pm}(k_x, k_y) = \pm\gamma_0 \cdot \sqrt{1 + 4 \cdot \cos\frac{\sqrt{3} \cdot k_x \cdot a}{2} \cdot \cos\frac{k_y \cdot a}{2} + 4 \cdot \cos^2\frac{k_y \cdot a}{2}} \quad (0.3)$$

, όπου γ_0 η ενέργεια κβαντικής μετάβασης πλησιέστερων γειτόνων (τυπικές τιμές $2.9 - 3.1eV$), $\vec{k} = (k_x, k_y)$ το διάνυσμα της πρώτης ζώνης Brillouin και a η σταθερά πλέγματος. Βάσει της σχέσης (0.3) προκύπτει το πλήρες ενεργειακό διάγραμμα που φαίνεται στην Εικόνα 0.5.



Εικόνα 0.5: α) Τρισδιάστατη δομή ενεργειακών ζωνών, με κόκκινο χρώμα φαίνεται η κυψελίδα του γραφενίου β) μεγέθυνση σε ένα από τα σημεία Dirac [13]

Οι ηλεκτρονικές ιδιότητες του γραφενίου μπορούν έτσι να περιγραφούν από ένα μοντέλο άμαζων φερμιονίων Dirac κοντά στο σημείο ουδετερότητας φορτίου (neutrality point), με γραμμική διασπορά και συμμετρία ηλεκτρονίων - οπών. Αυτοί οι "Dirac κώνοι" φορέων (οπών και ηλεκτρονίων) εμφανίζονται στις γωνίες της ζώνης Brillouin, τα σημεία της οποίας εφάπτονται στο επίπεδο Fermi, όπως απεικονίζεται στην Εικόνα 0.5(α). Τα έξι σημεία όπου οι κώνοι Dirac εφάπτονται, αναφέρονται ως τα σημεία Dirac σημεία [10].

Εκτός των ηλεκτρικών ιδιοτήτων, αξιοσημείωτες είναι και οι μηχανικές ιδιότητες. Όπως ο γραφίτης και το διαμάντι, έτσι και το γραφένιο παρουσιάζει πολύ καλή μηχανική ανθεκτικότητα. Αυτό, σε συνδυασμό με την απλότητα της ενσωμάτωσης του οξειδίου του γραφενίου σε μήτρες και το σχετικά φθινό κόστος του λεπτού γραφίτη, καθιστούν τα υλικά αυτά εξαιρετικές επιλογές για μηχανική ενίσχυση. Από την άλλη πλευρά, το γραφένιο εμφανίζει τόσο υψηλή αντοχή σε ένα μόνο φύλλο, γεγονός που το καθιστά ένα πολλά υποσχόμενο υλικό για εξαιρετικά λεπτές εφαρμογές νανο-ηλεκτρομηχανικών συστημάτων (nano-electromechanical systems – NEMS), όπως αντηχεία και αισθητήρες πίεσης [4]. Εκτός από την εξαιρετική αντοχή, το γραφένιο παρουσιάζει επίσης εξαιρετική αδιαπερατότητα. Αυτό οφείλεται στην υψηλή πυκνότητα ηλεκτρονίων στους αρωματικούς δακτυλίους του και στην ενέργεια των δεσμών άνθρακα-άνθρακα [14].

Η ειδική θερμότητα (C) ορίζεται ως η μεταβολή της ενεργειακής πυκνότητας (U) καθώς η θερμοκρασία (T) μεταβάλλεται κατά $1K$, $C = dU/dT$. Η ειδική θερμότητα καθορίζει τόσο την ποσότητα της θερμικής ενέργειας που αποθηκεύεται σε ένα σώμα όσο και το πόσο γρήγορα το σώμα ψύχεται ή θερμαίνεται, χρόνος ο οποίος ορίζεται θερμική σταθερά χρόνου (τ). Για το μονοστρωματικό γραφένιο η θερμική σταθερά χρόνου είναι περίπου $0,1 ns$, εκατό φορές μικρότερη από την αντίστοιχη σταθερά άλλων νανοδομών [14]. Η εξαιρετική θερμική αγωγιμότητα του γραφενίου το καθιστά πολλά υποσχόμενο για την απαγωγή θερμότητας σε διατάξεις νανοκλίμακας, αλλά υπάρχουν περιορισμοί που προκαλούνται από διεπιφάνειες και υλικά όπως το SiO_2 [15].

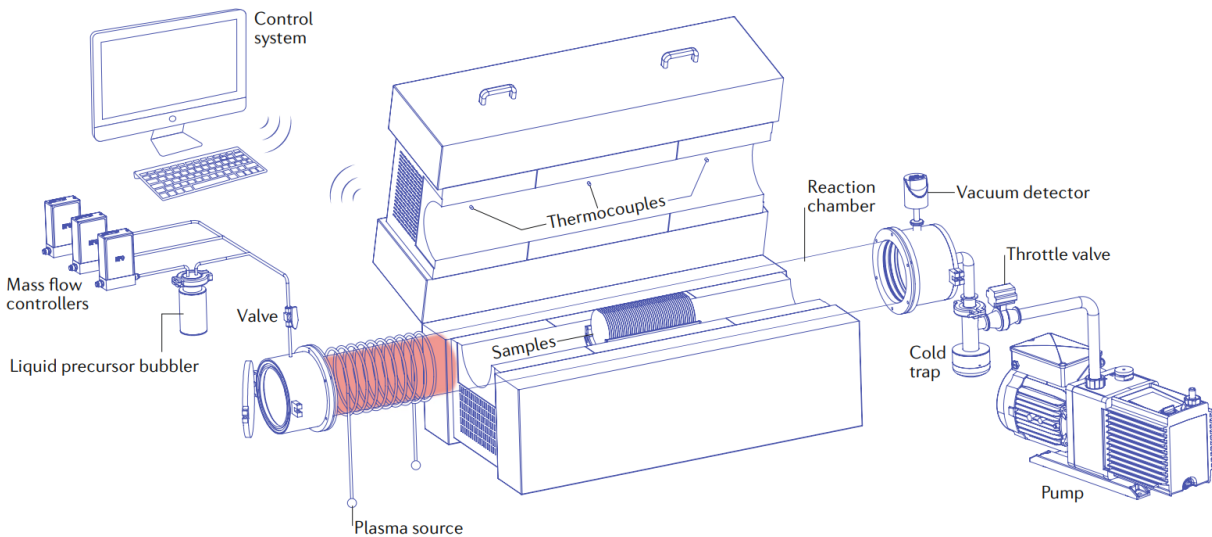
Όταν ο γραφίτης μετατρέπεται σε μονοατομικό γραφένιο, γίνεται πολύ διαφανής. Συνδυάζοντας τα ηλεκτρικά και οπτικά χαρακτηριστικά, το γραφένιο προσφέρει δυνατότητες ως εναλλακτική λύση στο ακριβό κλασικό οξειδίο ινδίου-, κασσιτέρου (Indium Tin Oxide – ITO), που χρησιμοποιείται για διαφανή αγώγιμη επίστρωση για οθόνες. Ο συνδυασμός της υψηλής αγωγιμότητας των υμενίων, της οπτικής διαφάνειας, της χημικής και μηχανικής σταθερότητας και του χαμηλού κόστους του χημικά απολεπισμένου γραφενίου σε σύγκριση με το οξειδίο ινδίου-, κασσιτέρου (Indium Tin Oxide – ITO) υποδεικνύει άμεσα τη χρήση του γραφενίου ως διαφανές ηλεκτρόδιο για υγρούς κρυστάλλους ή ηλιακές κυψέλες καθώς και ως διαφανές εύκαμπτο ηλεκτροδίων για βιολογικούς οργανισμούς [4], [6].

2.4 Τεχνικές σύνθεσης γραφενίου

Το γραφένιο συντίθεται πλέον με διάφορες τεχνικές. Μετά την ανακάλυψή του το 2004 με τη μέθοδο "scotch tape" (μηχανική απολέπιση/αποκόλληση) αναπτύχθηκαν διάφορες μέθοδοι για τη δημιουργία στρωμάτων και λεπτών υμενίων γραφενίου. Η χημική εναπόθεση ατμών (Chemical vapor deposition – CVD), η χημική απολέπιση και η χημική σύνθεση μεταξύ άλλων (Εικόνα 0.6) είναι μερικές από τις ευρέως χρησιμοποιούμενες τεχνικές για τη σύνθεση γραφενίου με τη CVD να είναι η πιο δημοφιλής [16].

Η CVD είναι μια τεχνική σύνθεσης από κάτω προς τα πάνω και χρησιμοποιείται συχνά στη βιομηχανία, καθώς μπορεί να παράγει γραφένιο υψηλής ποιότητας σε μεγάλη κλίμακα. Κατά τη διάρκεια αυτής της διαδικασίας λαμβάνουν χώρα χημικές αντιδράσεις υψηλής θερμοκρασίας μεταξύ αερίων υδρογονανθράκων (π.χ. ακετυλένιο – C_2H_2 και μεθάνιο – CH_4) και μιας

καταλυτικής μεταλλικής επιφάνειας (χαλκός ή νικέλιο) εντός ενός θαλάμου αντίδρασης με ελεγχόμενες συνθήκες θερμοκρασίας, πίεσης και ρυθμού ροής αερίου. Στο Σχήμα 2.14 παρουσιάζεται ένα τυπικό όργανο CVD με όλα τα εξαρτήματά του. Για την ενεργοποίηση της πηγής άνθρακα χρησιμοποιούνται δύο διεργασίες CVD: η θερμική CVD και η ενισχυμένη με πλάσμα CVD (Plasma-Enhanced CVD – PECVD) [16], [17].



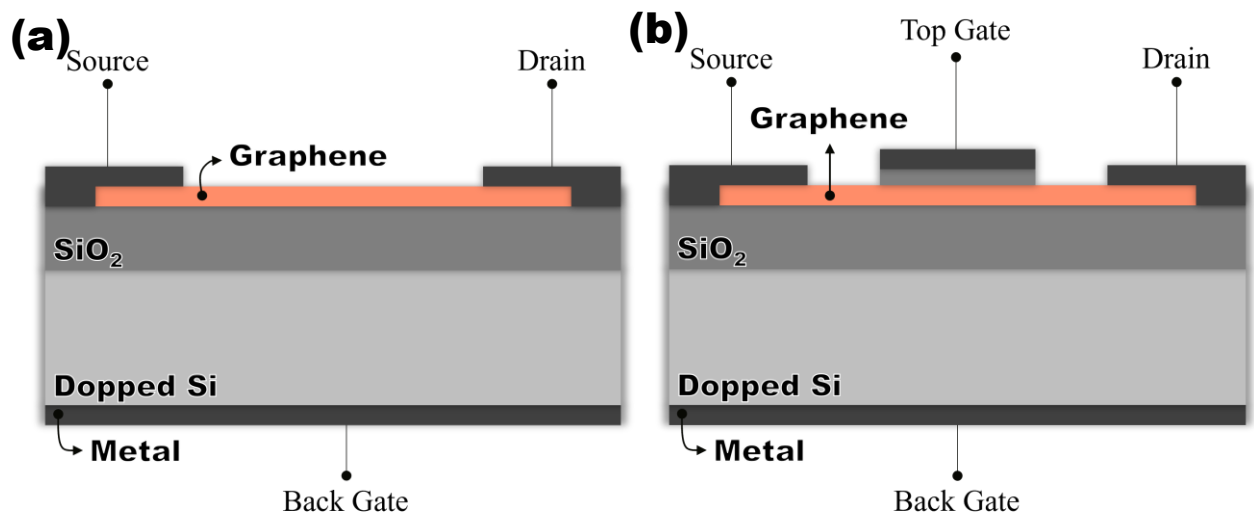
Εικόνα 0.6: Σχηματικό διάγραμμα ενός τυπικού εξοπλισμού CVD [18]

3 Τρανζίστορ επίδρασης πεδίου γραφενίου με υγρή πύλη

3.1 Basics of GFETs

Ένα FET είναι μια ηλεκτρονική διάταξη τριών ακροδεκτών όπου η αγωγιμότητα μεταξύ δύο ακροδεκτών: η πηγή και ο απαγωγός, ρυθμίζεται από το ηλεκτρικό πεδίο που δημιουργείται από τον τρίτο ακροδέκτη, την πύλη. Η πύλη λειτουργεί ως στοιχείο ελέγχου που καθορίζει την αγωγή υψηλού ή χαμηλού ρεύματος, επιτρέποντας τη χρήση του FET ως διακόπτη. Από φυσικής άποψης, ο έλεγχος αυτός επιτυγχάνεται καθώς η πύλη διαμορφώνει την πυκνότητα των ελεύθερων φορέων στο κανάλι μεταξύ της πηγής και του απαγωγού, το οποίο συμβατικά είναι νοθευμένο πυρίτιο [19].

Σε αντίθεση με τα παραδοσιακά MOSFET, στα GFET το κανάλι είναι απλώς γραφένιο. Η πρώτη αναφερόμενη [20] συσκευή FET από γραφένιο απεικονίζεται στην Εικόνα 0.7. Ακολουθώντας τη συμβατική δομή των FET, το διηλεκτρικό πίσω πύλης ήταν ένα στρώμα διοξειδίου του πυριτίου (SiO_2) κάτω από το κανάλι γραφενίου και ένα ντοπαρισμένο υπόστρωμα πυριτίου λειτουργούσε ως πίσω πύλη. Πρόκειται για μια πολύ χρήσιμη συσκευή για σκοπούς απόδειξης της θεωρίας (proof-of-concept), αλλά έχει μεγάλες παρασιτικές χωρητικότητες. Ως εκ τούτου, το 2007 [21] εισήχθη μια νέα δομή, με κορυφαία πύλη [22].

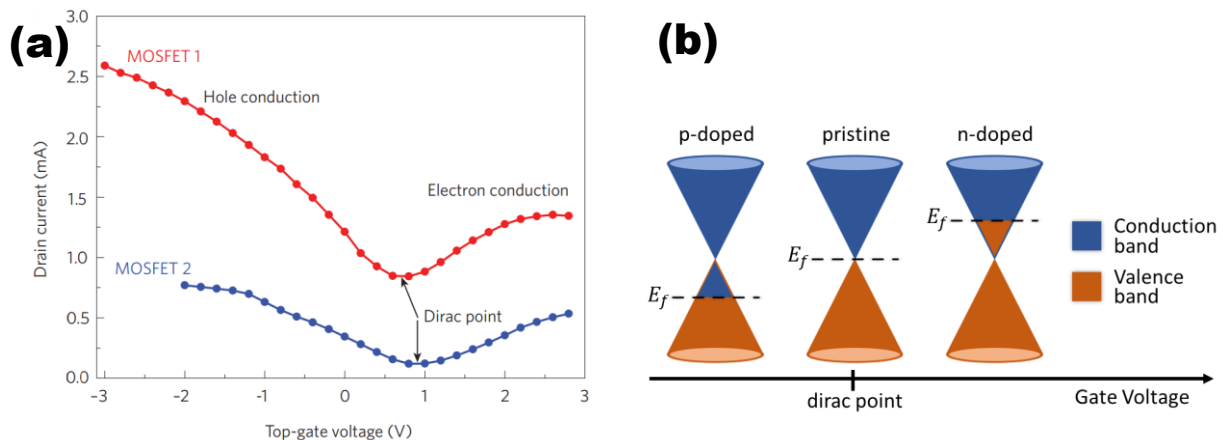


Εικόνα 0.7: Δομή GFETs: (a) πίσω πύλης, (b) διπλής πύλης [22].

Στα συμβατικά FET το ρεύμα ρέει μέσω του καναλιού μόνο με τη παρουσία τάσης πύλης (θετική για την περίπτωση NMOS, αρνητική για την περίπτωση PMOS), αντίθετα το γραφένιο είναι από τη φύση του αγωγίμο και επομένως στα GFET υπάρχει πάντα μια μικρή ροή ρεύματος. Επιπλέον,

στα GFETs το κανάλι γραφενίου ενεργοποιείται τόσο για θετικές όσο και για αρνητικές τάσεις πύλης. Όλα τα προαναφερθέντα φαινόμενα οδηγούν σε μια αμφιπολική χαρακτηριστική μεταφοράς ρεύματος-τάσης (Εικόνα 0.8.a) [22].

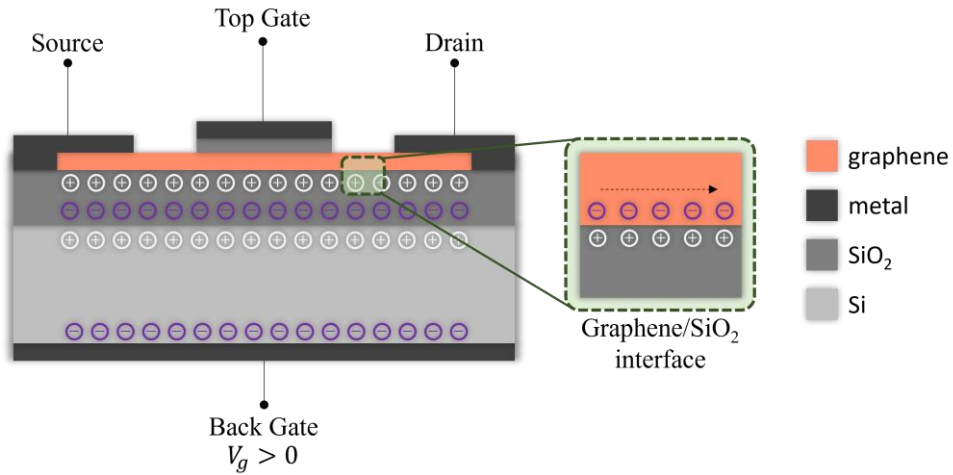
Στα GFET η εφαρμοζόμενη τάση πύλης καθορίζει τον τύπο των φορέων (ηλεκτρόνια ή οπές) στο κανάλι. Μεγάλες θετικές τάσεις πύλης οδηγούν σε συσσώρευση ηλεκτρονίων στο κανάλι, ενώ μεγάλες αρνητικές τάσεις πύλης οδηγούν σε συσσώρευση οπών (απουσία ηλεκτρονίων). Αυτοί οι 2 τύποι αγωγής έχουν ως αποτέλεσμα τους δύο κλάδους της $I_d - V_g$ καμπύλης που χωρίζονται από ένα σημείο ουδετερότητας ρεύματος ή όπως ονομάζεται σημείο Dirac (Εικόνα 0.8.a). Αξιοσημείωτη είναι η αλλαγή του επιπέδου Fermi του γραφενίου (Εικόνα 0.8.b). Για $V_g > V_{g,dirac}$, η ενέργεια Fermi αυξάνεται: η ζώνη σθένους διεισδύει στη ζώνη αγωγιμότητας και οδηγεί σε αγωγή ηλεκτρονίων. Από την άλλη πλευρά, για $V_g < V_{g,dirac}$ η ενέργεια Fermi μειώνεται και η ζώνη σθένους συρρικνώνεται, οδηγώντας σε αγωγιμότητα οπών [23].



Εικόνα 0.8: (a) Τυπικά χαρακτηριστικά μεταφοράς για δύο GFETs [22], (b) η μεταβολή του επιπέδου Fermi του γραφενίου με την εφαρμοζόμενη τάση πύλης

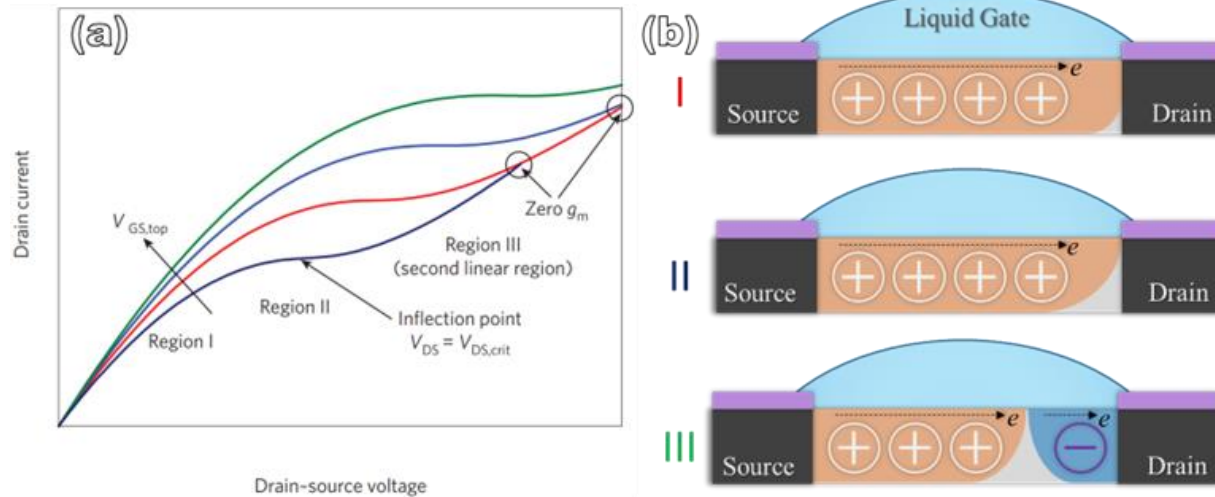
Η θετική τάση που εφαρμόζεται στην πίσω πύλη δημιουργεί ένα ηλεκτρικό πεδίο που προσελκύει ηλεκτρόνια μακριά από τα άτομα άνθρακα. Αυτή η διαδικασία είναι γνωστή ως ηλεκτροστατικό ντόπινγκ. Αναλυτικότερα, η Εικόνα 0.9 απεικονίζει τι συμβαίνει στη συσκευή όταν εφαρμόζεται $V_g > 0$. Η θετική τάση πύλης προσελκύει τα ηλεκτρόνια και, κατά συνέπεια, δημιουργεί θετικά φορτισμένες περιοχές που ονομάζονται "οπές" κάτω από το SiO_2 . Κατά συνέπεια, οι οπές προσελκύουν τα αρνητικά φορτία του SiO_2 αφήνοντας μια αφθονία θετικών φορτίων ακριβώς κάτω από το γραφένιο. Αυτά τα θετικά φορτία προσελκύουν τα ηλεκτρόνια του γραφενίου και έτσι τα απομονώνουν από τα άτομα άνθρακα, επιτρέποντάς τους να κινούνται

υπό την εφαρμογή τάσης απαγωγού. Η εφαρμογή αρνητικής τάσης πύλης έχει το αντίθετο αποτέλεσμα. Στην περίπτωση που χρησιμοποιούνται και οι δύο πύλες, η μία «βοηθάει» την άλλη οδηγώντας σε ορισμένη αγωγιμότητα ρεύματος με χαμηλότερη εφαρμοζόμενη τάση και στις δύο πύλες.



Εικόνα 0.9: Η επίδραση της εφαρμογής $V_g > 0$ στην πίσω πύλη ενός GFET

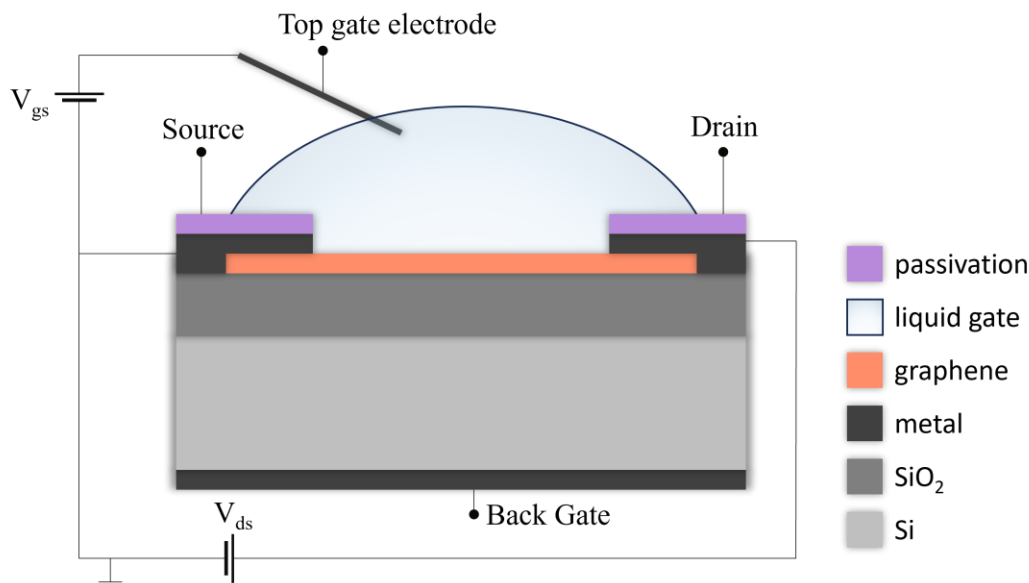
Η εφαρμογή τάσης απαγωγού είναι απαραίτητη για την παρακολούθηση της κίνησης των φορέων. Οι $I_d - V_d$ χαρακτηριστικές του μονοστρωματικού γραφενίου συντίθενται από τρεις ζώνες: τη περιοχή τριόδου, τη μονοπολική περιοχή κορεσμού και την αμφιπολική περιοχή κορεσμού. Η Εικόνα 0.10 απεικονίζει τη διαφορετική συμπεριφορά του καναλιού για τις 3 περιοχές λειτουργίας. Στην περιοχή I (περιοχή τριόδου) το ρεύμα μεταφέρεται από οπές σε όλο το μήκος του καναλιού. Καθώς αυξάνεται η V_{ds} , το ρεύμα απαγωγού φτάνει σε κορεσμό και τελικά το τρανζίστορ λειτουργεί στη μονοπολική περιοχή κορεσμού (περιοχή II) στο σημείο καμπής ($V_{ds} = V_{ds,crit}$). Όταν το V_{ds} ξεπεράσει το $V_{ds,crit}$, το τρανζίστορ εισέρχεται στην αμφιπολική περιοχή κορεσμού (περιοχή III). Εντός αυτής της περιοχής πόλωσης, οι φορείς στο κανάλι είναι ηλεκτρόνια στην πλευρά του απαγωγού και οπές στην πλευρά της πηγής [22], [24], [25].



Εικόνα 0.10: (a) Χαρακτηριστικές μεταφοράς $I_d - V_d$ για διαφορετικά V_g [22], (b) απεικόνιση της συγκέντρωσης φορέων στο κανάλι γραφενίου [25].

3.2 Liquid gate GFETs

Επεκτείνοντας την τεχνολογία των GFET με άνω πύλη, τα συνήθως χρησιμοποιούμενα στερεά διηλεκτρικά μπορούν να αντικατασταθούν από ένα υγρό (liquid-gate GFET, LG-GFET). Σε τέτοιες διατάξεις, το τρανζίστορ είναι ικανό να λειτουργεί σε πολύ χαμηλή τάση, επειδή το δυναμικό πύλης εφαρμόζεται στα πάχους νανομέτρων electrical double-layers (EDL) που σχηματίζονται στις διεπιφάνειες γραφενίου - ηλεκτρολύτη. Η δυνατότητα ανίχνευσης μικρών αλλαγών στις χαρακτηριστικές μεταφοράς των GFET ανοίγει το δρόμο για υπερευαίσθητη βιοανίχνευση [26]. Στην Εικόνα 0.11 απεικονίζεται ένα LG-GFET με εξωτερικό ηλεκτρόδιο άνω πύλης.



Εικόνα 0.11: Διάταξη GFET υγρής πύλης με εξωτερικό ηλεκτρόδιο άνω πύλης

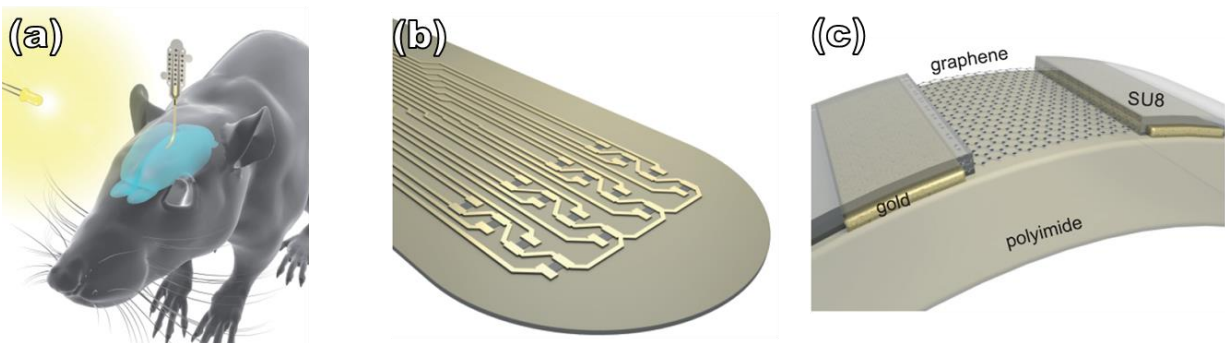
Οι αρχές λειτουργίας των LG-GFET δεν διαφέρουν από τα GFET οπίσθιας πύλης που παρουσιάζονται στην υποενότητα 3.1 στην Εικόνα 0.9. Η διαφορά έγκειται στο γεγονός πως το υγρό δρα ως μονωτής κατά αντιστοιχία με το SiO_2 στα τυπικά GFETs πίσω πύλης. Η ταυτόχρονη χρήση του ηλεκτροδίου της άνω πύλης και της πίσω πύλης μπορεί να ενισχύσει τη λειτουργία της παραπάνω διάταξης, καθώς η ενεργοποίηση των ηλεκτρονίων του γραφενίου θα είναι διπλή.

3.3 Εφαρμογές GFETs

Τα τρανζίστορ επίδρασης πεδίου γραφενίου (GFET) βρίσκονται στην αιχμή της τεχνολογίας βιοαισθητήρων, προσφέροντας μια ευέλικτη πλατφόρμα για την ανίχνευση βιοδεικτών ασθενειών με πολύ καλή ευαισθησία και ακρίβεια. «Λειτουργικοποιώντας» (functionalizing) το γραφένιο με υποδοχείς βιομορίων, όπως αντισώματα ή ανιχνευτές DNA, τα GFETs μπορούν να συνδεθούν επιλεκτικά με βιομόρια-στόχους σε διάλυμα, μεταφράζοντας βιολογικά σήματα σε ηλεκτρικές εξόδους [27]. Αυτή η ικανότητα επέτρεψε την ανάπτυξη προηγμένων βιοαισθητήρων, με παράδειγμα την ανίχνευση του SARS-CoV-2 [28] και διαφόρων άλλων βιομορίων [29], [30], αναδεικνύοντας τις τεράστιες δυνατότητες των GFETs για την επανάσταση στη διάγνωση της υγειονομικής περίθαλψης.

Εκτός από τις ικανότητές τους στη βιοανίχνευση, τα GFETs υπόσχονται πολλά και στον τομέα των νευρωνικών διεπαφών, όπως αποδεικνύεται από την εφαρμογή τους στη χαρτογράφηση της εγκεφαλικής δραστηριότητας [31], [32]. Χρησιμοποιώντας συστοιχίες εύκαμπτων GFETs,

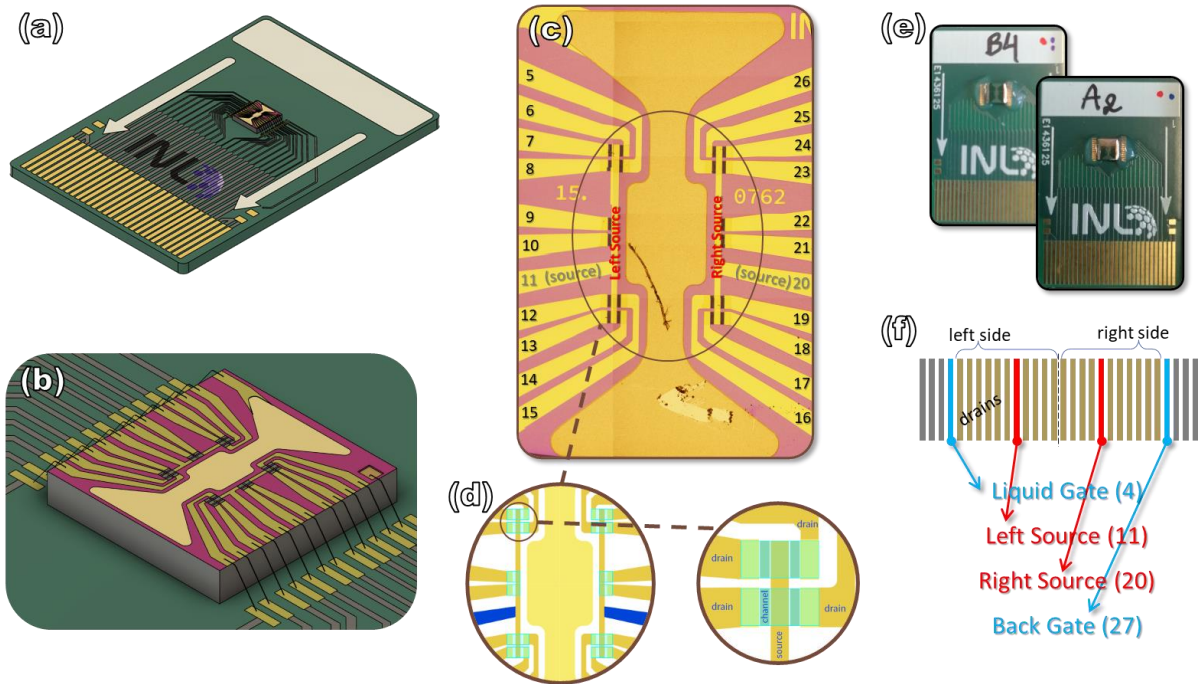
ερευνητές [32] πέτυχαν αξιοσημείωτη επιτυχία στην καταγραφή εγκεφαλικών σημάτων *in vivo*, ανταγωνιζόμενοι τις συμβατικές μεθόδους που βασίζονται σε μικροηλεκτρόδια, ενώ προσφέρουν ξεχωριστά πλεονεκτήματα όπως η ενίσχυση του σήματος και η ενσωμάτωση υψηλής πυκνότητας. Επιπλέον, οι συνεχιζόμενες εξελίξεις στην ενσωμάτωση υλικών, όπως ο συνδυασμός γραφενίου με υποστρώματα νιτριδίου του βορίου, έχουν τη δυνατότητα να βελτιώσουν περαιτέρω την απόδοση των GFET, ανοίγοντας το δρόμο για την άμεση ανίχνευση της δραστηριότητας του εγκεφάλου. Με τη σμίκρυνση, την προσιτή τιμή και τη συμβατότητά τους με τις διαδικασίες κατασκευής ημιαγωγών, οι βιοαισθητήρες GFET είναι έτοιμοι να φέρουν επανάσταση στη διαγνωστική σε σημεία περίθαλψης [27], όπως αποδεικνύεται από τον αυξανόμενο όγκο βιβλιογραφίας που τεκμηριώνει την επιτυχία τους και την εκτεταμένη υιοθέτησή τους στη βιοϊατρική έρευνα.



Εικόνα 0.12: (a) αναπαράσταση ενός εμφυτεύματος που τοποθετείται στην επιφάνεια του εγκεφάλου αρουραίου (b) αναπαράσταση της κεφαλής ενός εμφυτεύματος γραφενίου με διάταξη τρανζίστορ γραφενίου 4×4 και γραμμές τροφοδοσίας, (c) διατομή ενός εύκαμπτου τρανζίστορ γραφενίου με γραφένιο μεταξύ της επαφής πηγής και απαγωγού που καλύπτονται από μονωτικό φωτοανθεκτικό SU8 [32]

3.4 Το INL chip

Στην παρούσα εργασία χρησιμοποιείται και αναλύεται διεξοδικά ένα τσιπ με GFET (Εικόνα 0.13) που κατασκευάστηκε από το Iberian Nanotechnology Laboratory (INL) [26]. Αυτό το τσιπ ενσωματώνει 20 GFETs διπλής πύλης, μειώνοντας την πολυπλοκότητα των ηλεκτρικών μετρήσεων και ενισχύοντας τις δυνατότητες ολοκλήρωσης. Ο πυρήνας του τσιπ (Εικόνα 0.13.b) αποτελείται από ένα υπόστρωμα πυριτίου πάνω στο οποίο κατασκευάζονται τα GFET. Ειδικότερα, η δομή του πυρήνα χωρίζεται συμμετρικά σε δύο πλευρές, καθεμία από τις οποίες διαθέτει ένα κοινό ηλεκτρόδιο πηγής που διασυνδέει 10 GFETs, και υπάρχουν συνολικά 20 διατάξεις σε ένα τσιπ. Μέσω τεχνικών συγκόλλησης καλωδίων και PCB τα ηλεκτρόδια είναι συνδεδεμένα με τους ακροδέκτες του τσιπ (Εικόνα 0.13.f).



Εικόνα 0.13: a) τρισδιάστατη απεικόνιση του τσιπ, b) τρισδιάστατη απεικόνιση των 20 GFETs σε κοντινό πλάνο, c) κολάζ εικόνων οπτικού μικροσκοπίου που δείχνει τις 20 διατάξεις με αριθμούς που υποδεικνύουν την αντιστοιχία με τους ακροδέκτες, d) απεικόνιση των 20 GFETs και κοντινό πλάνο των φύλλων γραφενίου, e) φωτογραφία των τσιπ και f) χαρτογράφηση της αντιστοιχίας των ακροδεκτών με τα ηλεκτρόδια.

Τα LG-GFET κατασκευάζονται συνήθως χωρίς το ηλεκτρόδιο άνω πύλης και στη συνέχεια προστίθεται ένα εξωτερικό μεταλλικό ηλεκτρόδιο για τις μετρήσεις (Εικόνα 0.11). Το συγκεκριμένο τσιπ επιτρέπει τον ευέλικτο σχεδιασμό της διάταξης των τρανζίστορ και την κατασκευή επαφών επίπεδης τεχνολογίας με ενιαία λιθογραφική μάσκα, ενσωματώνοντας το ηλεκτρόδιο πύλης και καθιστώντας το συνεπίπεδο με τα ηλεκτρόδια πηγής και αποστράγγισης [26].

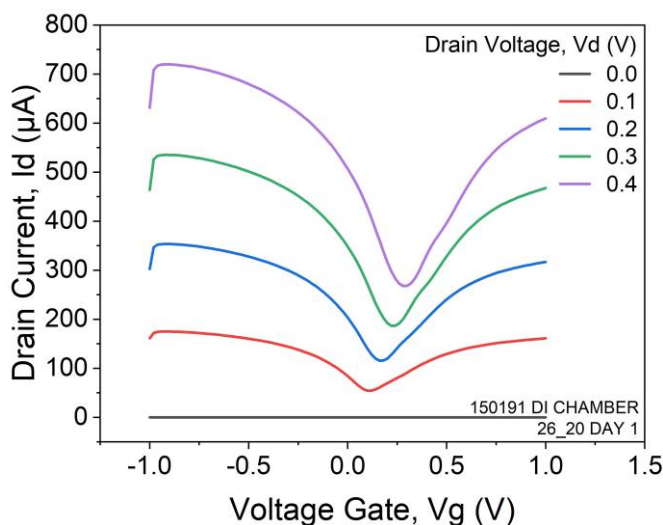
4 Ηλεκτρικός Χαρακτηρισμός και Εξαγωγή Παραμέτρων

4.1 Μεθοδολογία

Όλες οι μετρήσεις που παρουσιάζονται στην παρούσα εργασία πραγματοποιήθηκαν στο "Εργαστήριο Ηλεκτρικού Χαρακτηρισμού" στο INN του ΕΚΕΦΕ "ΔΗΜΟΚΡΙΤΟΣ". Για τις καμπύλες $I - V$ χρησιμοποιήθηκε ο HP 4155A Semiconductor Parameter Analyzer. Ο HP 4155A είναι ένα ηλεκτρονικό όργανο για τη μέτρηση και ανάλυση των χαρακτηριστικών των διατάξεων ημιαγωγών. Μπορεί να εκτελέσει πλήρεις μετρήσεις, καθώς μπορεί να συνδεθεί με λογισμικό LabView ή να χρησιμοποιήσει τις προεγκατεστημένες μορφές μετρήσεων. Το HP4155A ήταν συνδεδεμένο σε έναν microprober manipulator station που βρίσκεται μέσα σε ένα dark box. Επιπλέον, μετρήθηκαν καμπύλες $C - V$ για την πειραματική μέτρηση της χωρητικότητας του υγρού της άνω πύλης προς το ηλεκτρόδιο πύλης. Για τη λήψη αυτών των δεδομένων χρησιμοποιήθηκε το όργανο LCR HP4284A.

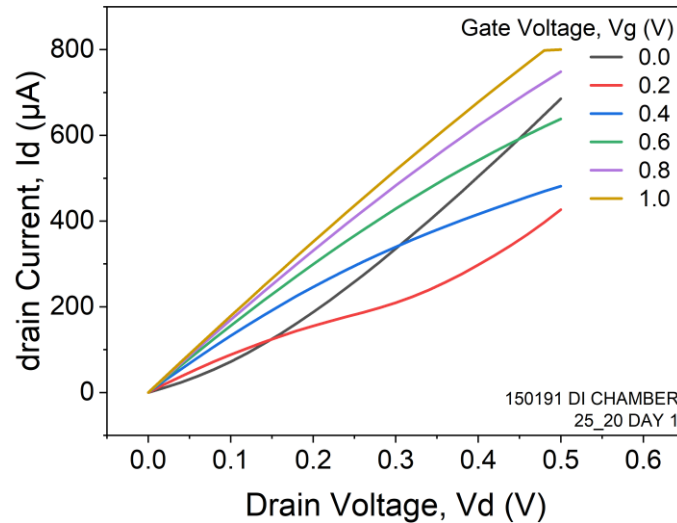
4.2 Χαρακτηριστικές καμπύλες

Στην Εικόνα 0.14 παρουσιάζονται οι καμπύλες $I_d - V_g$ για V_d από 0V έως 0,4V για το FET 26_20 με το πηγάδι πολυμερούς γεμάτο (0,3ml) με απεσταγμένο νερό. Για $V_d = 0V$ το ρεύμα απαγωγού είναι, όπως αναμενόταν, επίσης 0. Το σημείο Dirac μετακινείται προς τα δεξιά με την αύξηση της τάσης αποστράγγισης. Αυτό συμβαίνει λόγω της μείωσης της ενέργειας Fermi καθώς αυξάνεται η τάση στις επαφές. Για διατάξεις με αμφίπολα χαρακτηριστικά, όπως το γραφένιο, το χαμηλότερο ρεύμα εντοπίζεται εκεί όπου η πύλη αλλάζει το επίπεδο Fermi σε βαθμό που η έγχυση φορέων μεταξύ πηγής και αποστράγγισης εξισορροπείται. Δεδομένου ότι η V_d τροποποιεί την έγχυση φορέων, η πύλη στην οποία εντοπίζεται το ελάχιστο ρεύμα θα αλλάξει επίσης [33].



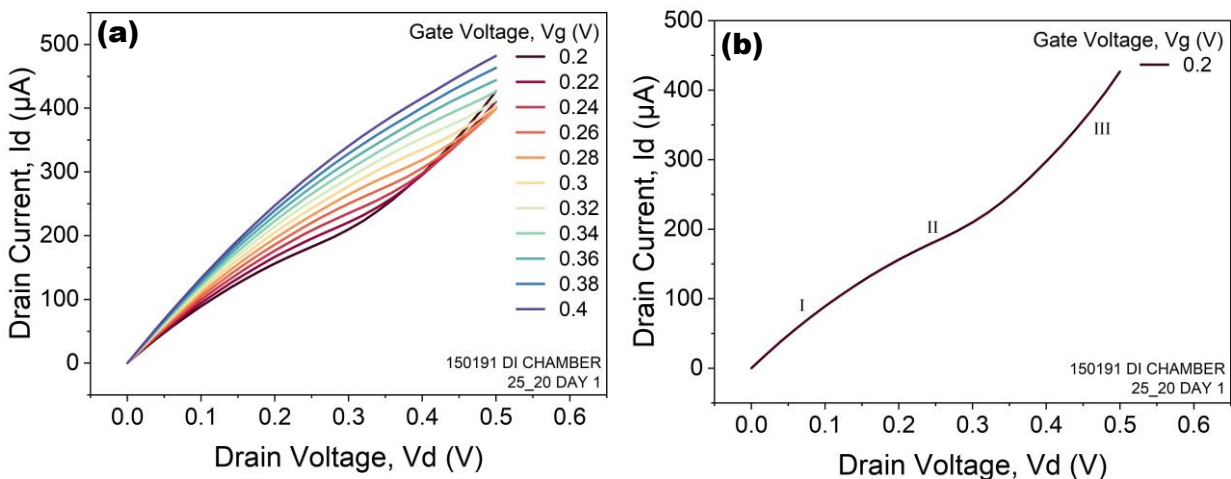
Εικόνα 0.14: $I_d - V_g$ καμπύλες για V_d από 0V μέχρι 0.4V για το FET 26_20

Στην Εικόνα 0.15 παρουσιάζονται οι χαρακτηριστικές καμπύλες $I_d - V_d$ για το FET 26_20 με το θάλαμο πολυμερούς γεμάτο (0,3ml) με απεσταγμένο νερό. Γενικά, εξαιρουμένης της καμπύλης για μηδενική τάση πύλης, με την αύξηση της τάσης πύλης η κλίση της καμπύλης, η οποία ισούται με την αγωγιμότητα, αυξάνεται, δηλαδή η αντίσταση μειώνεται. Αυτό είναι λογικό αφού όσο υψηλότερη είναι η τάση πύλης τόσο μεγαλύτερη είναι η συγκέντρωση φορέων στο γραφένιο και συνεπώς τόσο πιο αγώγιμο γίνεται. Πιο συγκεκριμένα, για διαφορετικές τιμές της V_g παρατηρούνται διαφορετικές συμπεριφορές: για $V_g = 0V$ η καμπύλη είναι κυρτή, για $V_g = 0.2V$ η καμπύλη αλλάζει καμπυλότητα στο μέσο της και για $V_g > 0.2V$ όλες οι καμπύλες έχουν την ίδια μορφή (κοίλες) και τείνουν να φτάσουν σε ένα πλατώ. Καθώς αυξάνεται η εφαρμοζόμενη V_g , η συμπεριφορά της διάταξης γίνεται ωμική (σταθερή κλίση). Η αλλαγή στη συμπεριφορά της καμπύλης από $V_g = 0.2V$ σε $V_g = 0.4V$ δείχνει ότι το σημείο Dirac βρίσκεται μεταξύ αυτών των δύο τιμών.



Εικόνα 0.15: (a) $I_d - V_d$ για V_g από $0V$ μέχρι $1V$ για το FET 25_20

Η Εικόνα 0.16 δείχνει τη διαφορετική συμπεριφορά για $V_g < V_{g,dirac}$ και για $V_g > V_{g,dirac}$. Η τάση $V_{g,dirac} = 0.34V$ είναι η πρώτη στην οποία η καμπύλη δεν αλλάζει καμπυλότητα οπότε το σημείο Dirac βρίσκεται μεταξύ $0,32V$ και $0,34V$. Επίσης, στο Εικόνα 0.16.b φαίνονται οι 3 περιοχές λειτουργίας ενός GFET που συζητήθηκαν στο υποκεφάλαιο 3.1.

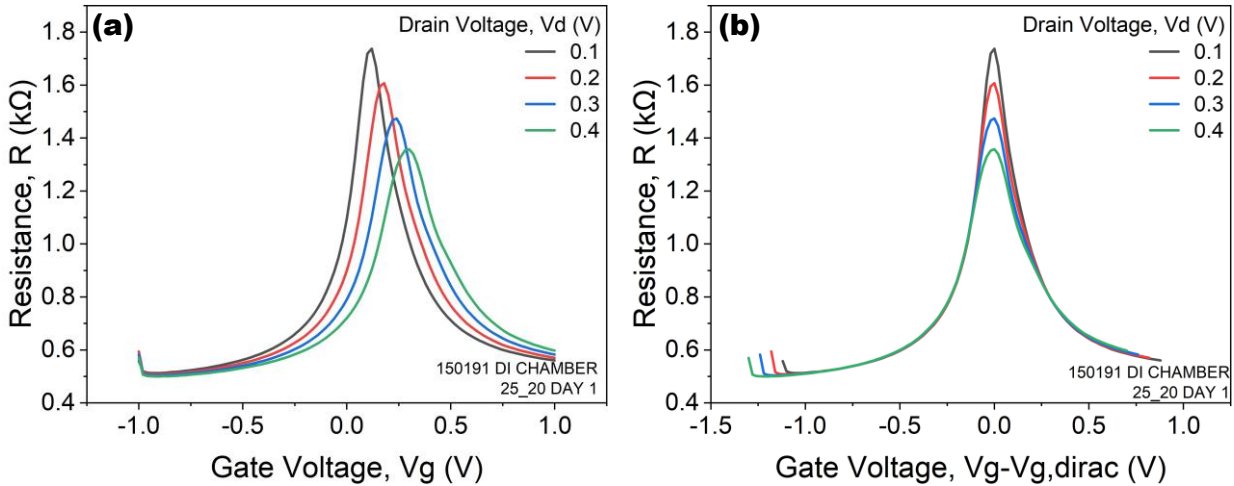


Εικόνα 0.16: (a) $I_d - V_d$ καμπύλη για V_g γύρω από το $V_{g,dirac}$, (b) $I_d - V_d$ καμπύλη για $V_g = 0.2V$, όπου φαίνονται οι 3 περιοχές λειτουργίας ενός GFET: I) περιοχή τριοδίου, II) περιοχή μονοπολικού κορεσμού και III) περιοχή αμφιπολικού κορεσμού [24].

4.3 Εξαγωγή παραμέτρων

Από τις παραπάνω καμπύλες μπορούν να εξαχθούν γραφήματα για τη διαγωγιμότητα, την εξωτερική αγωγιμότητα, την αντίσταση κ.α. καθώς και να εξαχθούν σταθερές παράμετροι για το γραφένιο και τη λειτουργία των τρανζίστορ. Οι καμπύλες αντίστασης μπορούν να προκύψουν από

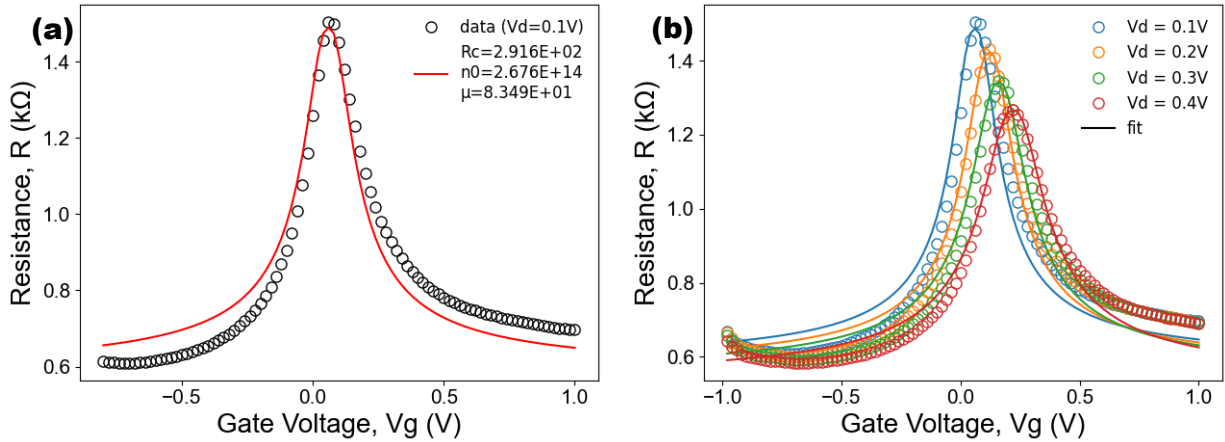
τις καμπύλες $I_d - V_g$. Οι καμπύλες αντίστασης ως προς την τάση πύλης (Εικόνα 0.17) προκύπτουν από τη σχέση $R = V_d/I_d$, αν εφαρμοστεί στις καμπύλες στην Εικόνα 0.14. Καθώς η τάση πύλης πλησιάζει την τάση πύλης στο σημείο Dirac, η αντίσταση αυξάνεται λόγω της μείωσης των φορέων. Η Εικόνα 0.17.b δείχνει τις καμπύλες αντίστασης μετατοπισμένες προς τα αριστερά κατά $V_{g,dirac}$ και έτσι δείχνει ότι η αντίσταση, σε μια περιοχή μακριά από το $V_{g,dirac}$, δεν εξαρτάται από την εφαρμοζόμενη τάση απαγωγού.



Εικόνα 0.17: Καμπύλες αντίστασης συναρτήσει της τάσης πύλης (a) και συναρτήσει της τάσης πύλης $-V_{g,dirac}$ (b).

Η αντίσταση που φαίνεται στην Εικόνα 0.17 είναι η "πλήρης" αντίσταση της διάταξης, συμπεριλαμβανομένης της αντίστασης του γραφενίου και της αντίστασης επαφής. Πιο αναλυτικά [34] η εικονιζόμενη αντίσταση δίνεται από τη σχέση $R_{tot} = R_{channel} + R_{contact}$, όπου $R_{channel}$: η αντίσταση του γραφενίου στην περιοχή που καλύπτεται από την άνω πύλη, $R_{contact}$: η αντίσταση του γραφενίου στην ακάλυπτη περιοχή συν την αντίσταση των επαφών (διεπιφάνεια γραφενίου-επαφής). Στην παρούσα διάταξη υπάρχουν 2 επαφές και καθόλου ακάλυπτο γραφένιο, οπότε $R_{contact} = 2R_c$, μία R_c για κάθε επαφή.

Εικόνα 0.18 δείχνει την προσαρμογή [33] της άνω σχέσης στα πειραματικά δεδομένα.



Εικόνα 0.18: η προσαρμογή [33] της άνω σχέσης στα πειραματικά δεδομένα για (a) $V_d = 0.1V$ και για (b) για όλες τις μετρούμενες τάσεις απαγωγού του τσιπ 150191 με το πηγάδι πολυμερούς γεμάτο με νερό.

Ο Πίνακας 0.1 παρουσιάζει τις εξαγμένες παραμέτρους από τις προσαρμογές στην Εικόνα 0.18.b. Παρατηρείται ότι καθώς αυξάνεται η τάση απαγωγού, η αντίσταση επαφής μειώνεται, η εναπομένουσα συγκέντρωση των φορέων αυξάνεται και η αποτελεσματική κινητικότητα μειώνεται.

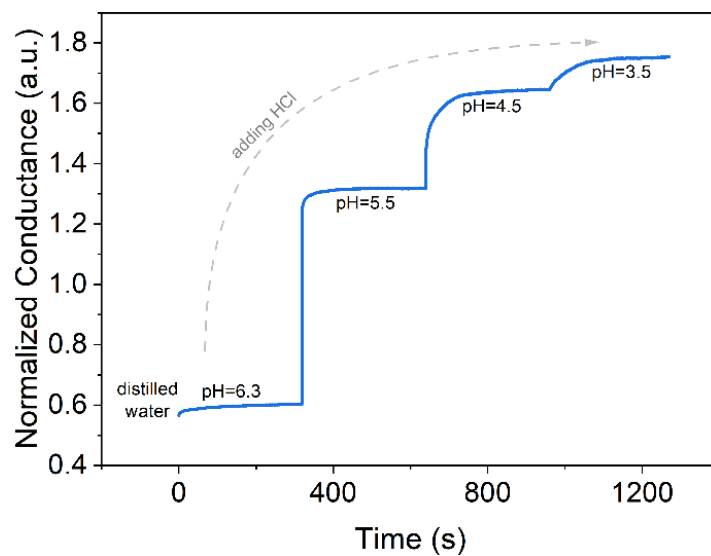
Πίνακας 0.1: παράμετροι που εξάχθηκαν από την προσαρμογή στην Εικόνα 0.18.

$V_d(V)$	Contact Resistance – $R_C (\Omega)$	Residual Carrier Concentration – $n_0 (/m^2)$	Effective Mobility – $\mu_{eff} (m^2/Vs)$
0.1	290.2	$3.14 \cdot 10^{14}$	71.29
0.2	282	$3.48 \cdot 10^{14}$	67.79
0.3	274.4	$3.96 \cdot 10^{14}$	64.52
0.4	264.6	$4.62 \cdot 10^{14}$	59.41

5 Χρήση του INL chip ως αισθητήρα pH

Η δυνατότητα του τσιπ να χρησιμοποιηθεί ως αισθητήρας pH αποτελεί μια σημαντική πρόοδο στο πεδίο των βιοϊατρικών εφαρμογών. Η διακριτική ικανότητα των τσιπ INL να ανιχνεύουν διαφορές στο pH υπογραμμίζει την ευαισθησία τους στα ιόντα και θέτει νέες βάσεις για τη χρήση αυτών των τσιπ INL ως βιοαισθητήρων. Η αγωγιμότητα του γραφενίου στα LG-FETs παρουσιάζει εξάρτηση από το pH του διαλύματος που χρησιμοποιείται ως μέσο πύλης. Το φαινόμενο αυτό μπορεί να αποδοθεί στις θεμελιώδεις αρχές της ηλεκτροχημικής ισορροπίας και στην αλληλεπίδραση μεταξύ του γραφενίου και του ηλεκτρολύτη. Όταν σε ένα υδατικό διάλυμα προστίθεται οξύ, η συγκέντρωση των υδροξονίων (H_3O^+) αυξάνεται σύμφωνα με τη χημική ισορροπία που διέπει τη διάλυση των όξινων ειδών. Ένα παράδειγμα αυτής της διαδικασίας μπορεί να παρατηρηθεί στην αντίδραση μεταξύ χλωριούχου υδρογόνου (HCl) και νερού: $HCl + H_2O \rightarrow H_3O^+ + Cl^-$. Αυτή η μετατόπιση ισορροπίας έχει ως αποτέλεσμα υψηλότερη πυκνότητα φορέων φορτίου στο διάλυμα. Κατά συνέπεια, όταν εφαρμόζεται τάση πύλης, ένας αυξημένος πληθυσμός φορτίων συσσωρεύεται στη διεπιφάνεια μεταξύ του ηλεκτρολύτη και της επιφάνειας του γραφενίου. Αυτά τα πρόσθετα ιόντα διαμορφώνουν την πυκνότητα φορέων φορτίου εντός του καναλιού γραφενίου και έτσι αυξάνουν την αγωγιμότητά του.

Για την απόδειξη αυτή, αρχικά παρασκευάστηκαν τρία υδατικά διαλύματα υδροχλωρίου (HCl) με τιμές pH 3,4, 4,5 και 5,5. Τα διαλύματα αυτά προέκυψαν με τη διαδικασία της αραίωσης από ένα αρχικό διάλυμα HCl που χαρακτηρίστηκε από pH 1. Η αραίωση έγινε υπό συνεχή ανάδευση και το pH μετρήθηκε με ηλεκτρονικό μετρητή pH. Έτσι, στο τέλος αυτής της διαδικασίας, υπήρχαν 4 διαλύματα: τα 3 προαναφερθέντα διαλύματα και το απεσταγμένο νερό, το pH του οποίου μετρήθηκε σε 6,3. Κατά τη διάρκεια των μετρήσεων του ρεύματος απαγωγού συναρτήσεως του χρόνου (δειγματοληψία) μία σταγόνα από κάθε διάλυμα τοποθετήθηκε στο τσιπ. Οι 3 ακίδες άγγιζαν τη σταγόνα, την πηγή και τον απαγωγό. Κατά τη διάρκεια της δειγματοληψίας μετρήθηκε το ρεύμα απαγωγού, ενώ εφαρμοζόταν σταθερή τάση πύλης, για την επιτάχυνση της κίνησης των φορέων του διαλύματος στην επιφάνεια του γραφενίου, και τάση πόλωσης αποστράγγισης. Για να μειωθεί η επίδραση από διαφορετικές τάσεις απαγωγού, η κανονικοποιημένη αγωγιμότητα $\left(\frac{G(t)-G(V_{g,1},V_{d,1})}{G(V_{g,1},V_{d,1})}\right)$ είναι το μέγεθος που παρουσιάζεται. Μετά τις μετρήσεις δειγματοληψίας, τα δεδομένα συνδυάστηκαν στην Εικόνα 0.19.



Εικόνα 0.19: Κανονικοποιημένη αγωγιμότητα προς χρόνο για διαλύματα διαφορετικών τιμών pH

6 Καλλιέργεια Κυττάρων

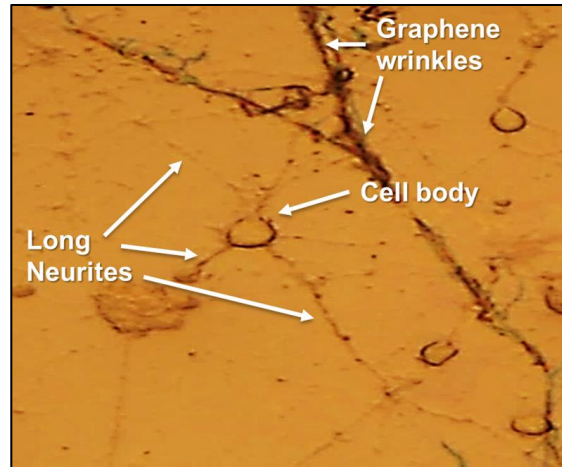
Μετά την επιβεβαίωση της ευαισθησίας των τσιπ INL σε ιόντα, η προσοχή μετατοπίζεται τώρα στην απόδειξη της βιοσυμβατότητάς του. Για να επιτευχθεί αυτό, καλλιεργήθηκαν κύτταρα Neuro-2A για 4 ημέρες και απομονωμένοι νευρώνες από την εμβρυϊκή περιοχή του ιππόκαμπου (E16,5) για 10 ημέρες πάνω σε φύλλα γραφενίου μεταφερμένα σε 300nm SiO₂.

Αναλυτικότερα, τα κύτταρα Neuro-2A καλλιεργήθηκαν σε θρεπτικό μέσο (DMEM-FBS 2%) παρουσία ρετινοϊκού οξέος (10μM) για 4 ημέρες και αξιολογήθηκε η νευριτική τους ανάπτυξη. Η καλλιέργεια έγινε σε 5 δείγματα για τη στατιστική μελέτη της ανάπτυξης των νευρικών κυττάρων. Την 4η ημέρα το 46,28% των κυττάρων είχε διαφοροποιηθεί με μέση ανάπτυξη νευριτών 3,027μm. Στην Εικόνα 0.20 παρουσιάζεται ένα παράδειγμα των αναπτυσσόμενων νευρώνων.



Εικόνα 0.20: Εικόνα οπτικού μικροσκοπίου από την καλλιέργεια κυττάρων Neuro-2A σε γραφένιο

Επιπλέον, απομονωμένοι νευρώνες από την εμβρυϊκή περιοχή του ιππόκαμπου καλλιεργήθηκαν για 10 ημέρες (Εικόνα 6.2). Οι πρωτογενείς καλλιέργειες νευρώνων του ιππόκαμπου παρουσίασαν φυσιολογική ανάπτυξη στο δείγμα γραφενίου, επιβεβαιώνοντας τη δυνατότητά του ως μέσο για την καλλιέργεια και διαφοροποίηση νευρωνικών κυττάρων. Τα πειράματα αυτά συμβάλλουν σημαντικά προς την κατεύθυνση της τεκμηρίωσης της βιοσυμβατότητας των τσιπ INL, ανοίγοντας το δρόμο για την εφαρμογή τους στη νευροβιολογία και σε συναφείς τομείς.



Εικόνα 0.21: Εικόνα οπτικού μικροσκοπίου από την καλλιέργεια απομονωμένων νευρώνων από την εμβρυϊκή περιοχή του ιππόκαμπου

7 Συμπεράσματα

Σκοπός της παρούσας εργασίας ήταν ο ηλεκτρικός χαρακτηρισμός συστοιχιών τρανζίστορ επίδρασης πεδίου γραφενίου υγρής πύλης. Οι χαρακτηριστικές μεταφοράς και εξόδου $I_d - V_g$ και $I_d - V_d$ και οι κατάλληλες τεχνικές εξαγωγής παραμέτρων, όπως η παραγωγή και η προσαρμογή καμπυλών, επέτρεψαν την εξαγωγή πολύτιμων τιμών – όπως η αντίσταση επαφής, η συγκέντρωση φορέων, η αποτελεσματική κινητικότητα και άλλα – για τη λειτουργία των τσιπ. Οι μετρήσεις σε όλα τα LG-GFET πολλών τσιπ επέτρεψαν τη στατιστική αξιολόγηση των υπό διερεύνηση διατάξεων και έδειξαν τον τρόπο με τον οποίο επηρεάζονται από συνθήκες, όπως η υγρασία και η μόλυνση από την ατμόσφαιρα. Επιπλέον, οι μετρήσεις που λήφθηκαν για υδατικά διαλύματα διαφορετικών τιμών pH, τα οποία χρησιμοποιήθηκαν ως υγρή πύλη, κατέδειξαν μια σαφή ευαισθησία των LG-GFET σε ιόντα. Τέλος, η επιτυχής καλλιέργεια κυττάρων σε γραφένιο ανοίγει νέους δρόμους για εφαρμογές που χρησιμοποιούν το συγκεκριμένο τσιπ. Η καταγραφή νευρικών σημάτων και η μελέτη της επίδρασης των κυττάρων στις χαρακτηριστικές καμπύλες είναι μόνο παραδείγματα της έρευνας που θα μπορούσε να ακολουθήσει. Το γεγονός ότι υπάρχει μια συστοιχία τρανζίστορ και όχι μια μεμονωμένη διάταξη επιτρέπει την εξάλειψη του θορύβου καθώς και την ταυτόχρονη μελέτη της συμπεριφοράς των κυττάρων από διαφορετικά σημεία.

Ωστόσο, κατά τη διάρκεια αυτής της εργασίας παρατηρήθηκαν ορισμένες αστοχίες όσον αφορά το τσιπ. Πρώτον, η συμπεριφορά των LG-GFET φαίνεται να διαφέρει πολύ από τσιπ σε τσιπ και επίσης από FET σε FET εντός του ίδιου τσιπ. Αυτό δεν επιτρέπει μια συνεκτική μελέτη, καθώς δεν υπάρχει κοινό σημείο αναφοράς όταν αλλάζουν οι μεταβλητές. Επιπλέον, τα τσιπ φαίνεται να είναι πολύ ευαίσθητα, ακόμη και με αποσταγμένο νερό, έχοντας υποβαθμιστική επίδραση σε διάστημα λίγων μόνο ημερών. Μάλιστα, όταν έρχονται σε επαφή με πιο όξινα διαλύματα, παρατηρείται ηλεκτροχημική εγχάραξη, γεγονός που υποδηλώνει κακή μόνωση των μετάλλων. Πιθανές βελτιώσεις θα ήταν, μια καλύτερη και πιο σταθερή διαδικασία κατασκευής, για την εξάλειψη της διακύμανσης της λειτουργίας, και ένα καλύτερο πιο ανθεκτικό στρώμα παθητικοποίησης. Η δοκιμή διαφορετικών υλικών για το συνεπίπεδο ηλεκτρόδιο της άνω πύλης, θα ήταν επίσης μια καλή πρόταση, καθώς το Au/Cr, το οποίο χρησιμοποιείται, δεν φαίνεται να αλληλεπιδρά καλά με το απεσταγμένο νερό.

Συνολικά, η εργασία αυτή έθεσε τις βάσεις για περαιτέρω έρευνα και για πολλές βιοϊατρικές εφαρμογές που θα μπορούσαν να χρησιμοποιούν το υπό μελέτη τσιπ LG-GFET της INL. Πριν

από τη χρήση σε τελικές εφαρμογές εφαρμογή θα πρέπει να εκτελεστούν περαιτέρω μετρήσεις και μελέτη θορύβου, που είναι πραγματικά σημαντική όταν έχουμε να κάνουμε με νευρικά κύτταρα, που αποδίδουν πολύ χαμηλά σήματα.



Main English Part

1 Introduction

Graphene, a single layer of carbon atoms arranged in a hexagonal lattice, serves as testament of material science's creativity. Its discovery in 2004 [1] welcomed a new era of possibilities, as this atomically thin substance showcased unimaginable properties that do not align with its petite size. From its remarkable strength, surpassing even steel and diamond, to its flexibility, transparency and electrical conductivity, graphene has captured the focus of researchers and engineers.

The versatility of graphene knows no bounds, finding applications across diverse sectors such as electronics, energy storage, healthcare, and beyond. Its conductivity, both electrically and thermally, has motivated innovations ranging from conductive inks and paints for electronic circuits to advanced heat-dissipating gels. Moreover, the lightweight nature of graphene presents prospects for industries seeking to reduce the environmental footprint of their products, from automotive to airplanes [2], [3], [4].

In recent years, graphene field effect transistors (GFETs) have emerged as a focal point of research, particularly in the realm of biosensing and neural signal acquisition. Liquid gated GFETs (LG-GFETs) have attracted notice for their ability to seamlessly integrate with biological environments, offering opportunities for interfacing electronics with living systems. These advancements hold promise not only for enhancing healthcare through biosensors but also for helping individuals with disabilities through neural signal reading sensors, paving the way for improved communication and motor function restoration [5], [6].

This thesis aims to delve into the intricacies of LG-GFETs, showcasing their underlying principles and potential applications. Through the characterization of GFET chips, that are obtained from the International Iberian Nanotechnology Laboratory (INL), this work seeks to extract the parameters critical for their performance. Furthermore, by demonstrating their ion sensitivity and compatibility with biological solutions, this research lays the groundwork for future endeavors in the realm of bioelectronics and neural interface technology.

2 Graphene

Graphene is a two-dimensional atomically thick lattice of carbon atoms, arranged into a honeycomb form [1], [3] and it has attracted significant interest after its laboratory discovery in 2004 [1]. 0D fullerenes, 1D nanotubes and 3D graphite are all derived from graphene (Figure 2.1) [1]. Based on the number of layers, it can be classified into three categories: single-layer or monolayer graphene (1 layer), double-layer graphene (2 layers) and few-layer graphene (3 – 9 layers) reaching the limit of graphite (10 layers) [1]. The combination of graphene's outstanding electrical properties, transparency, flexibility, mechanical strength, and biocompatibility is making graphene an intriguing research topic [5]. During the last years it has been used in transistor fabrication indicating its ability to detect potentials [7].

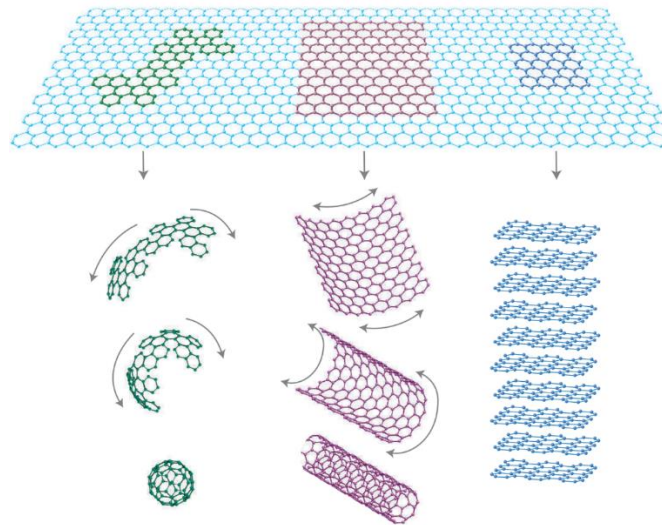


Figure 2.1: Graphene (upper part) can be rolled into fullerenes (lower left), wrapped into nanotubes (lower center) and stacked into graphite (lower right)

It is noteworthy that, till 2004 it was believed that 2D crystals could not exist freely in nature due to thermodynamic instability. However, in 2004 this theory was disproved by A. K. Geim and K. S. Novoselov as they succeeded in experimentally isolating a 2D graphite sheet, which they named graphene [1]. This discovery was awarded in 2010 with a Physics Nobel.

2.1 Graphene Structure

2.1.1 Atomic Bonds in Graphene

The unique properties of graphene are a result of its electronic structure, which will be discussed below. The building block of graphene, carbon (${}^6_6\text{C}$), is the sixth element of the periodic table (2th period and 14th group) and its electron distribution is $1s^2 2s^2 2p_x^1 2p_y^1 2p_z^0$ (Figure 2.2.a). Although the energy level $2p_z$ is equivalent to the levels $2p_x$ and $2p_y$, for convenience, it is kept empty. The carbon atom therefore has 4 valence electrons which are capable of creating hybrid orbitals sp , sp^2 and sp^3 . In case that sp^2 orbitals are created then three neighbor carbon atoms share electrons, and thus create the characteristic cellular form of monolayer graphene. Each carbon atom is shared between three cells, so each cell theoretically has $6/3 = 2$ whole carbon atoms [9].

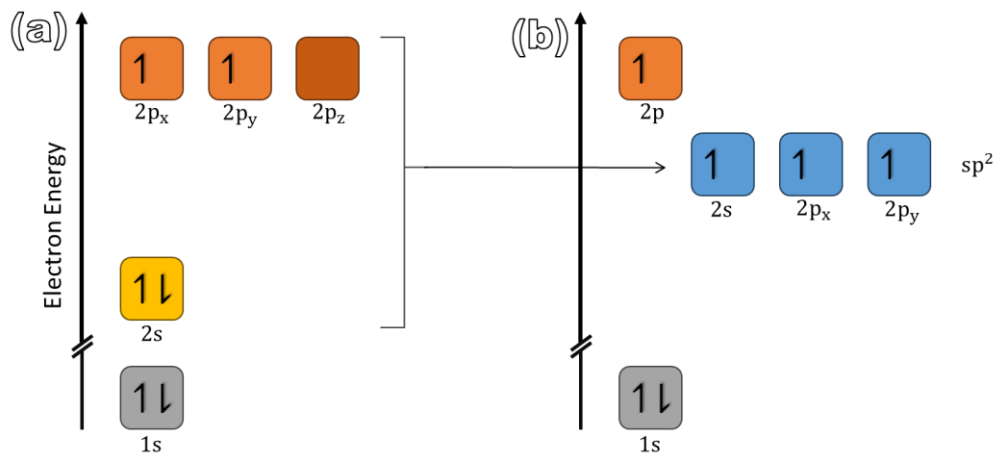


Figure 2.2: (a) Electron distribution of a carbon atom, (b) electron distribution of a carbon atom after sp^2 hybridization.

Figure 2.3.e shows how two adjacent carbon atoms in the graphene monolayer lattice are connected. In detail, a π bond between the $2p_z$ orbitals (in a plane parallel to the plane of the graphene sheet) and a σ bond between the sp^2 hybrid orbitals are created. The σ bond achieves very short atomic distance of just $\sim 1.42\text{\AA}$ which is even smaller than the bond of the sp^3 hybrid orbitals in the carbon-carbon bond in diamond, the hardest naturally occurring material known to man. This is why monolayer graphene has very good mechanical properties. In addition, the π bonds do not allow large van der Waals forces to exist between two graphene sheets in bilayer and

multilayer graphene and it allows electrons to move with ease in the graphene lattice [9]. Finally, in monolayer graphene the conduction band and the valence band have zero energy gap due to the π and π^* zones created [10].

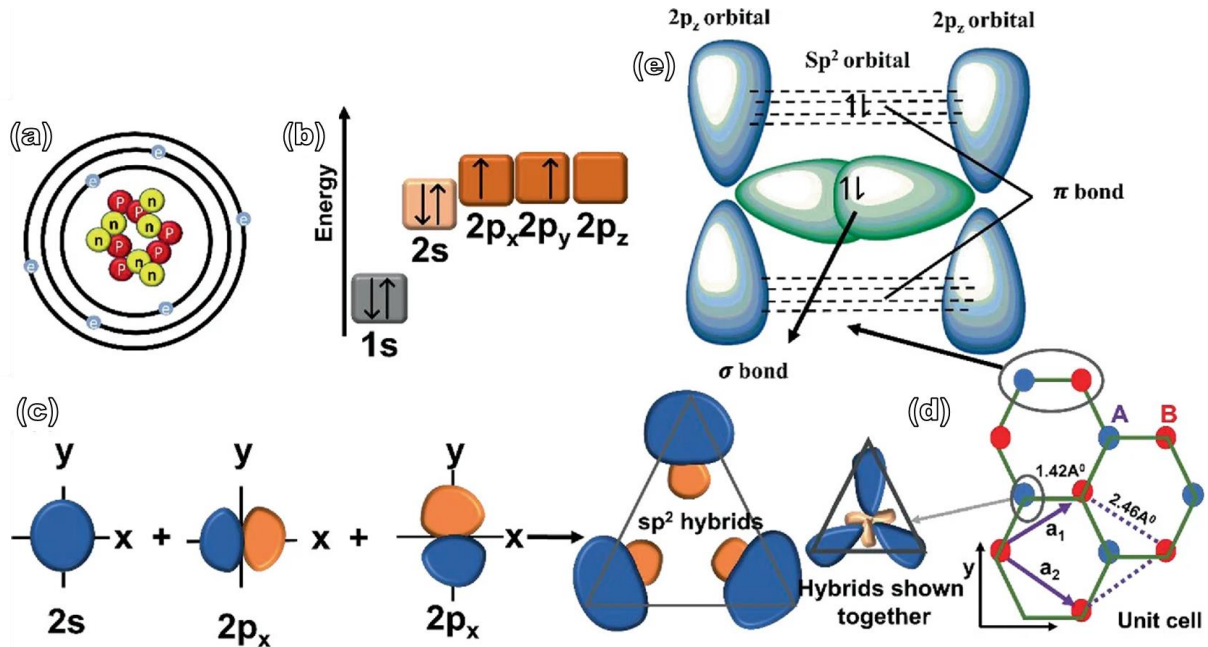


Figure 2.3: (a) The carbon atom's atomic structure, (b) Carbon atoms' outer electron energy levels, (c) The formation of sp^2 hybrids, (d) The crystal lattice of graphene, where A and B are carbon atoms belonging to different sub-lattices, a_1 and a_2 are unit-cell vectors, (e) Sigma bond and pi bond formed by sp^2 hybridization [9]

2.1.2 Graphene Lattice

The sp^2 hybridization of the carbon atoms, which has been discussed above, leads to a cellular form. In particular, as shown in Figure 2.4, the structure of graphene is described as a hexagonal lattice with a basis of two atoms. The graphene base is rhombic and includes two atoms 1 and 2 with a $a_{cc} = 1.42\text{\AA}$ distance between them [11].

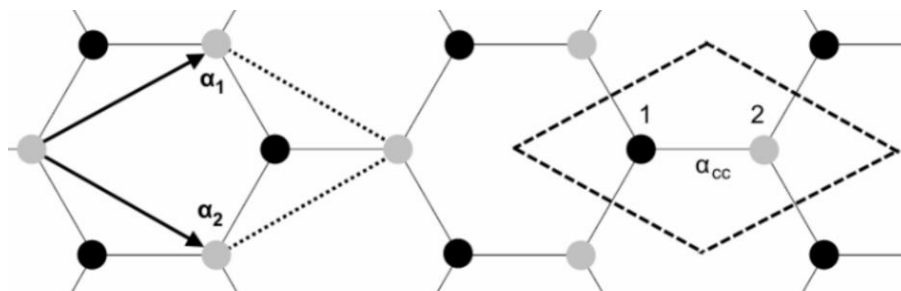


Figure 2.4: The unit cell of graphene with atoms 1 and 2, the basis vectors $\vec{\alpha}_1$ and $\vec{\alpha}_2$ and the distance between two adjacent carbon atoms (carbon - carbon) a_{cc}

2.1 Graphene Structure

The two-dimensional basis vectors are in the same plane as the graphene and are expressed exclusively in terms of the x and y coordinates. The basis vectors $\vec{\alpha}_1$ and $\vec{\alpha}_2$ of the graphene lattice can be expressed as follows:

$$\vec{\alpha}_1 = \left(\frac{1}{2}\alpha, \frac{\sqrt{3}}{2}\alpha \right) \text{ and } \vec{\alpha}_2 = \left(\frac{1}{2}\alpha, -\frac{\sqrt{3}}{2}\alpha \right) \quad (2.1)$$

Where $\alpha = |\vec{\alpha}_1| = |\vec{\alpha}_2| = 2.46\text{\AA}$ is the lattice constant. The lattice constant (α) is the distance between unit cells and differs from the distance between two adjacent carbon atoms (a_{cc}) [11].

Energy diagrams are expressed in k-space, which is the Fourier transform of real space, so in addition to analysis in real space, analysis in k-space is useful [10]. The vectors of the reciprocal space grid \vec{b}_1 and \vec{b}_2 satisfying the conditions $\vec{\alpha}_1 \cdot \vec{b}_1 = \vec{\alpha}_2 \cdot \vec{b}_2 = 2\pi$ and conditions $\vec{\alpha}_1 \cdot \vec{b}_2 = \vec{\alpha}_2 \cdot \vec{b}_1 = 0$ are given by the relations:

$$\vec{b}_1 = \left(\frac{2\pi}{\alpha}, \frac{2\pi}{\sqrt{3}\alpha} \right) \text{ and } \vec{b}_2 = \left(\frac{2\pi}{\alpha}, -\frac{2\pi}{\sqrt{3}\alpha} \right) \quad (2.2)$$

Figure 2.5 shows the resulting grid in reciprocal space, where the first Brillouin zone is colored in grey [11]. The first Brillouin zone is defined as the set of points in reciprocal space closest to the point (0, 0) than at any other point on the reciprocal grid [12]. Of particular importance for the description of the energy structure are the high symmetry points Γ , K , K' and M shown in Figure 2.5 [11].

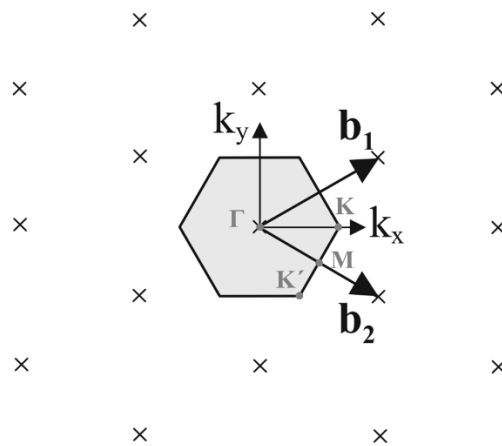


Figure 2.5: The reciprocal lattice of monolayer graphene, where crosses indicate reciprocal lattice points, and vectors b_1 and b_2 are primitive lattice vectors. The shaded hexagon indicates the first Brillouin zone [11]

2.2 Graphene Properties

The rapid growth of interest in graphene as a material lies in its diverse set of unusual properties [4]. Graphene has many excellent properties in terms of optical transparency, electrical conductivity, mechanical strength and thermal conductivity [3].

2.2.1 Electrical Properties

The electronic band structure of monolayer graphene can be described using a tight-binding Hamiltonian approach, which gives analytical solutions for its energy distribution. This model concludes to:

$$E_{\pm}(k_x, k_y) = \pm\gamma_0 \cdot \sqrt{1 + 4 \cdot \cos\frac{\sqrt{3} \cdot k_x \cdot a}{2} \cdot \cos\frac{k_y \cdot a}{2} + 4 \cdot \cos^2\frac{k_y \cdot a}{2}} \quad (2.3)$$

Where γ_0 , the transfer integral, is the nearest neighbor hopping energy (typical values 2.9 – 3.1eV), $\vec{k} = (k_x, k_y)$ is the vector of the first Brillouin zone and a is the lattice constant. Plotting the (2.3) results in the complete energy diagram shown in Figure 2.6.

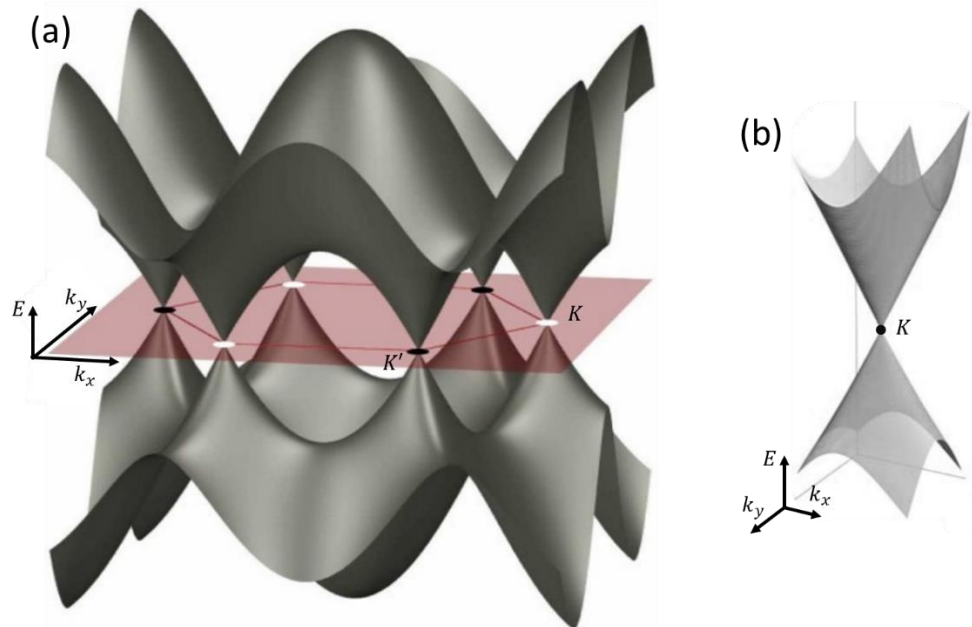


Figure 2.6: a) Three-dimensional energy band structure, the first Brillouin zone is shown in red, b) zoom in one Dirac point [13]

An important reason for the interest in graphene is the special and unique nature of its carriers. Typically, the Schrödinger equation is what is enough to describe electronic properties of materials

in condensed matter physics. However, graphene is an exception — instead of beginning with the Schrödinger equation, its charge carriers more naturally and easily approximate relativistic particles and can be explained using the Dirac equation. While electrons flowing around carbon atoms are not inherently relativistic, new quasiparticles are created when they interact with the periodic potential of the honeycomb lattice in graphene. These quasiparticles, referred to as massless Dirac fermions, can be considered as either neutrinos that took the electron charge e or as electrons that have lost their rest mass m_0 [1].

The electrical properties of graphene can thus be described by a Dirac model of fermions near the charge neutrality point, with linear dispersion and electron-hole symmetry. These "Dirac cones" of carriers (holes and electrons) appear at the corners of the Brillouin zone, whose points are tangent to the Fermi plane, as illustrated in Figure 2.6(a). The six points per honeycomb, where the Dirac cones are touching are referred to as the Dirac points [10].

The term graphene theoretically refers to monolayer graphene and sometimes is also used for bilayer graphene, as both of them are semimetals with no overlap between the valence and conduction bands. The electronic structure of few-layer graphene (FLG, number of layers from 3 to < 10), is more intricate due to the emergence of charge carriers from several layers. As shown in Figure 2.7 the band structure diagrams for different layers of graphene are similar, with the two bands meeting. The difference lies in the fact that as the layers increase, higher-energy bands are also present, the "total" band has a more and more parabolic behavior and the characteristic Dirac point of monolayer graphene is nonvisible [9]. More intriguingly, bilayer and FL graphene a band gap can be formed with the application of a perpendicular electrical (Figure 2.8.c) [35].

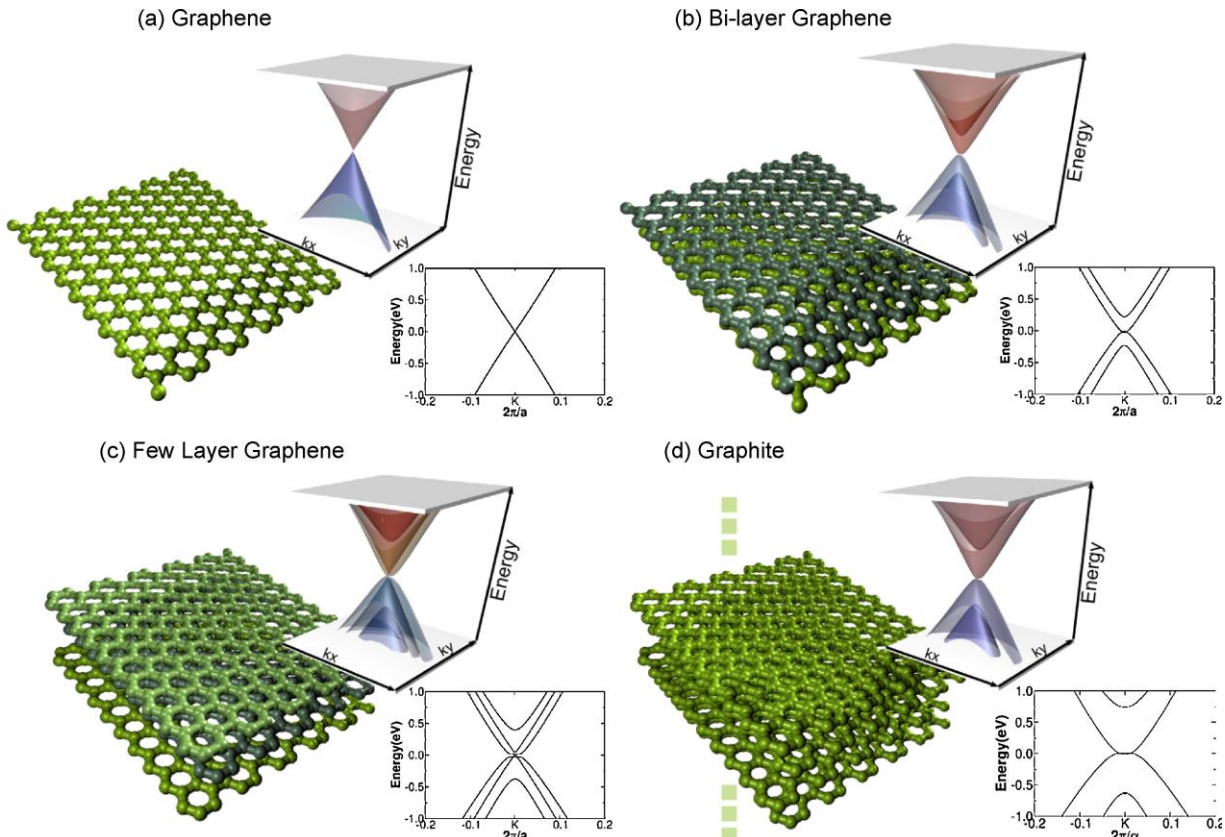


Figure 2.7 3D band structure and its projection on k_x close to K point for (a) graphene, (b) bilayer graphene, (c) trilayer graphene and (d) graphite [2]

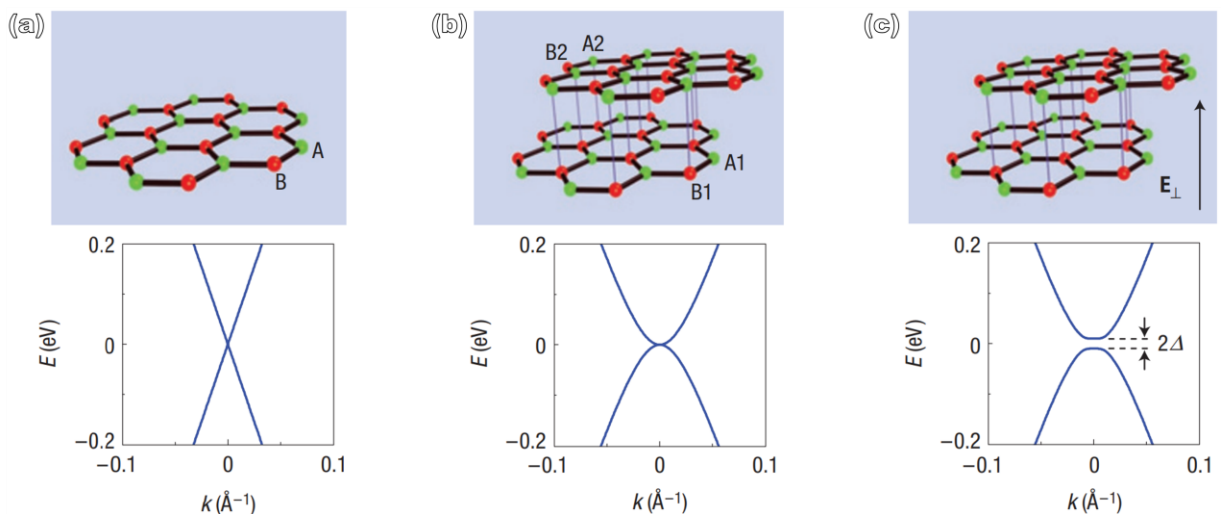


Figure 2.8: Schematic diagrams of the lattice structure of monolayer (a) and bilayer (b) graphene (for bilayer graphene, a pair of higher-energy bands is also present, not shown in the diagram), (c) when an electric field (E_{\perp}) is applied perpendicular to the bilayer, a bandgap is opened in bilayer graphene, whose size is modulated by the electric field. [35]

2.2.2 Thermal Properties

The specific heat (C) is defined as the change in energy density (U) as the temperature (T) changes by $1K$, $C = dU/dT$. The specific heat determines both the amount of thermal energy stored in a body and how quickly the body cools or heats, which is the thermal time constant (τ) of the body, $\tau \approx RCV$, where R is the thermal resistance and V the volume of the body. For monolayer graphene the thermal time constant is about 0.1 ns , a hundred times lower than the corresponding constant of other nanostructures [15].

Experimental studies at the University of California, Riverside, utilized optothermal Raman techniques to investigate the thermal conductivity (K) of graphene, revealing values exceeding $\sim 3000 \text{ WmK}^{-1}$ near room temperature, surpassing bulk graphite. Further studies confirmed high K values for suspended graphene, with estimates ranging from 1500 to 5000 WmK^{-1} . The data for suspended or partially suspended graphene proved closer to intrinsic K due to reduced thermal coupling to the substrate, enabling a clearer understanding of graphene's thermal behavior. Conversely, supported graphene, attached to the substrate along its entire length, exhibited lower K values, around 600 WmK^{-1} near room temperature, attributed to graphene – substrate coupling effects. Despite variations, graphene consistently demonstrates remarkable thermal conductivity properties, holding significant promise for diverse applications [36]. Graphene's excellent thermal conductivity makes it promising for heat sinking in nanoscale devices, but dissipation limitations caused by interfaces and materials like SiO_2 require additional engineering. This includes exploring thermoelectric cooling at metal contacts to manage device temperature effectively [15].

2.2.3 Mechanical Properties

Like graphite and diamond, graphene has also established a breakthrough for mechanical resilience. Figure 2.9.a shows how the elastic stress – strain response was measured with AFM nanoindentation. A defect-free graphene sheet has a stiffness of the order of $300 - 400 \text{ N/m}$, a breaking strength of about 42 N/m and a Young's modulus of roughly $0.5 - 1.0 \text{ TPa}$. These characteristics, along with the simplicity of integrating graphene oxide into matrices and the relatively cheap cost of thin graphite, make these materials excellent choices for mechanical reinforcement. On the other hand, graphene exhibits such a high sustainable tension in a single sheet, which makes it a highly promising material for ultra-thin nano-electromechanical systems (NEMS) applications like resonators and pressure sensors [4]. Mechanically exfoliated single- and

multilayer graphene sheets positioned over gaps in a SiO₂ substrate were contacted to create graphene-based NEMS (Figure 2.9.c) [37].

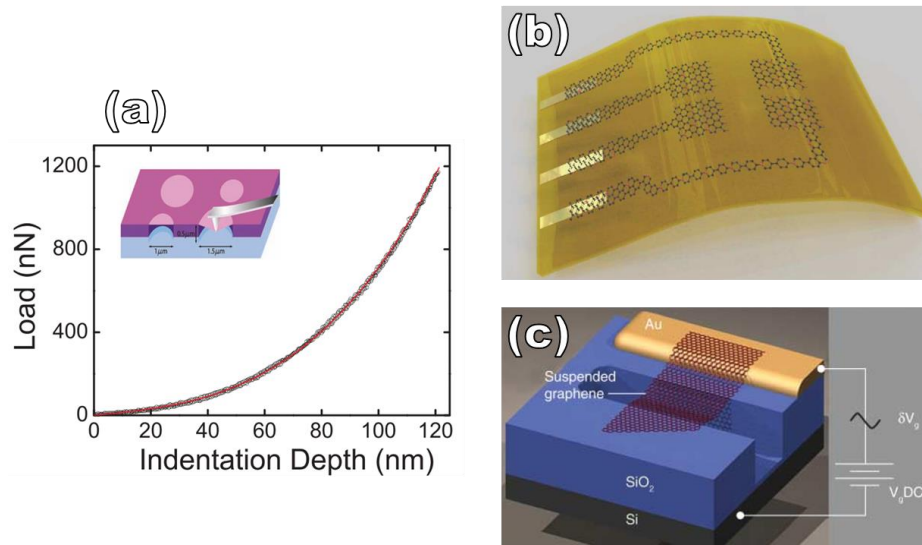


Figure 2.9: (a) Loading/unloading curve for a suspended graphene device [38], (b) Schematic illustration of a flexible graphene neural electrode array. In order to communicate with the data acquisition system, patterned graphene electrodes come in contact with Au contact pads. [6] (c) Schematic of a suspended graphene resonator [37]

In addition to excellent strength, graphene also exhibits excellent impermeability. In particular, it is the thinnest material that is impermeable, but it also has the best impermeability of all materials known to man. This is due to its very high resistance to externally applied forces, the high electron density in its aromatic rings and the energy of the carbon-carbon bonds. In Figure 2.10 an isolated Graphene cell is illustrated [14].

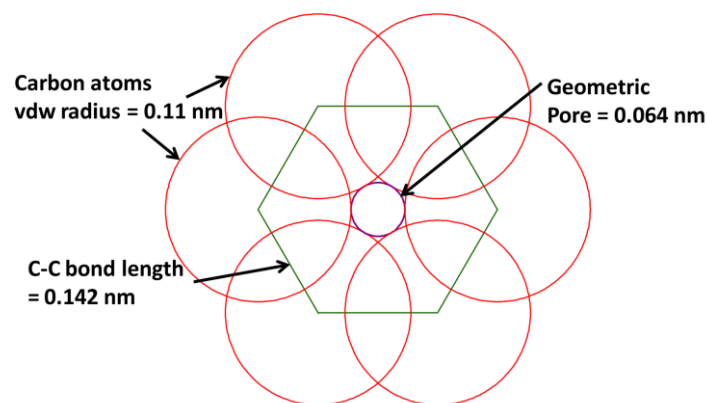


Figure 2.10: Geometric characteristics of graphene lattice [14]

As can be seen in Figure 2.10, the empty space left free (geometric pore) for any atoms of other materials to pass through has a diameter of only 0.064 nm . By comparing the radius of the geometric pore with that of molecules of various materials, it is observed that even Hydrogen ($H\text{ radius} = 0.314\text{ nm}$) and Helium molecules ($He\text{ radius} = 0.280\text{ nm}$) cannot penetrate the aromatic bonds of the graphene cell. Due to their high impermeability, graphene films are promising for use in protective coating and separation applications [14]. Additionally, graphene's flexibility makes it ideal for flexible electrodes used for biological signals acquisition (Figure 2.9.b) [6].

2.2.4 Optical Properties

As seen in Figure 2.11.a, when graphite is reduced down to a graphene monolayer, it really becomes very transparent. Combining the great electrical and optical characteristics, graphene offers potential as an alternative to the expensive traditional Indium Tin Oxide (ITO), used for transparent conductive coating for displays (e.g. liquid crystal displays, OLED displays, plasma displays, touch panels). Actually, as the number of graphene layers increases, the transparency decreases linearly (Figure 2.11.b). The transmittance is greater than 95% for 2-nm thick films and stays over 70% for 10-nm thick films [4].

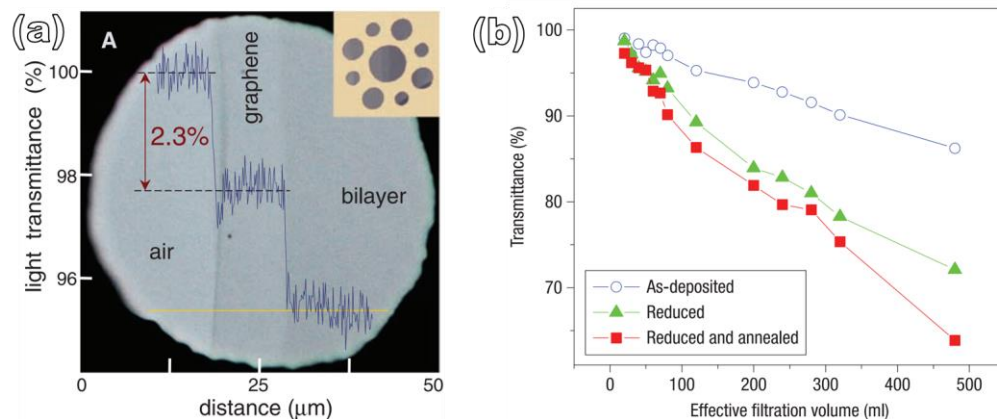


Figure 2.11: (a) Photograph of a 50-mm aperture partially covered by monolayer and bilayer graphene, (a - right upper corner) the depicted sample [39], (b) transmittance of graphene oxide (GO) and reduced GO (graphene) at $\lambda \sim 550\text{ nm}$ as a function of filtration volume [40].

The combination of high film conductivity, optical transparency, chemical and mechanical stability, and low cost of chemically exfoliated graphene when compared to ITO straightaway indicates using graphene as a transparent electrode for liquid crystal or solar cells as well as a processable transparent flexible electrode material [4], [6].

2.3 Growth Mechanisms of Graphene

Graphene is now synthesized using a variety of techniques. Several methods were developed to create graphene layers and thin films following its isolation in 2004 with the “scotch tape” method (mechanical exfoliation/cleavage). Chemical vapor deposition (CVD), chemical exfoliation and chemical synthesis among others (Figure 2.12) are few of the widely used techniques for synthesizing graphene. The number of layers, thickness, kind, and average size of the graphene materials determine if top-down or bottom-up techniques are more appropriate to be used. In top-down growth mechanisms, graphene sheets are produced by exfoliation/separation of graphite and its derivatives including graphite oxide (GO). In the contrary, in bottom-up techniques graphene is grown on top of other materials [16].

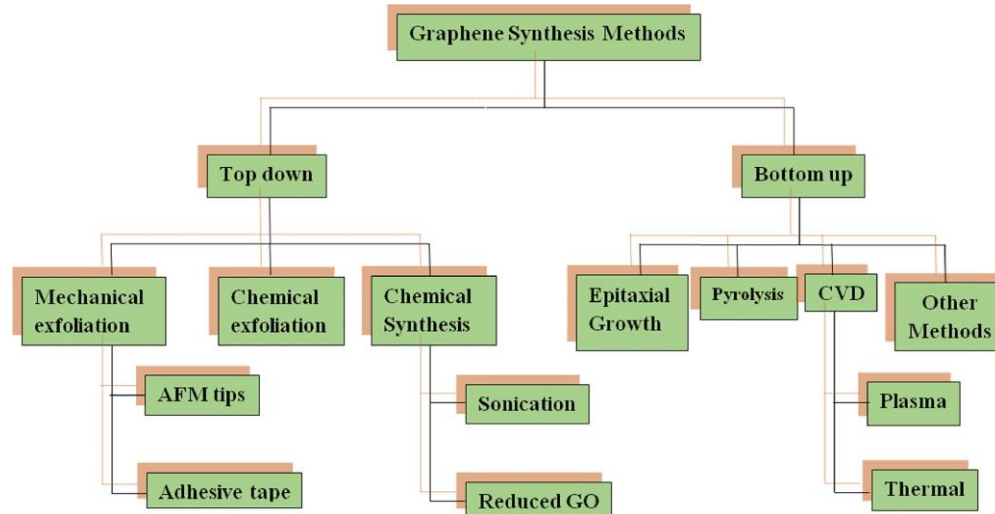


Figure 2.12: Diagrammatic depiction of several graphene growth techniques [41]

2.3.1 Mechanical exfoliation

Mechanical exfoliation is alternatively referred to as Scotch tape or peel-off method. Novoselov and Geim [1] were the ones that introduced this technique to produce graphene for the first time, using an adhesive tape to break the weak Van der Waals bonds of graphite [41] and separate the graphene layers (Figure 2.13.a). In this process, multiple layers of graphene adhere to the tape with the initial peel, but with multiple peeling, graphene flakes are the end product. To separate the flakes from the tape, a certain substrate (acetone) is used and the final flakes of different sizes and shaped can be observed on SiO₂/Si substrates (Figure 2.13.b). Due to the slow and inaccurate

nature of this technique, it is mostly used to study graphene properties rather than being employed for commercial purposes [16].

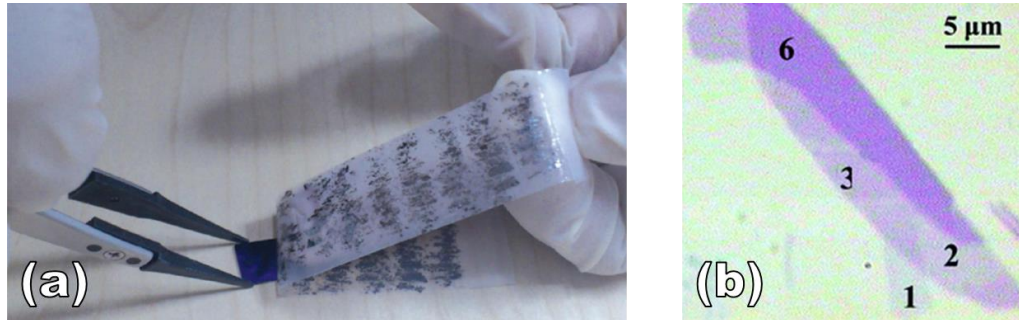


Figure 2.13: (a) ‘Scotch tape’ graphene synthesis procedure [16], (b) Optical micrograph of multilayer with 1, 2, 3, and 6 layers graphene [42]

2.3.2 Chemical vapor deposition

Chemical vapor deposition (CVD) is a bottom-up synthesis technique and it is commonly met in industry as it can produce high-quality graphene on a large-scale basis. During this process high-temperature chemical reactions occur between hydrocarbon gases (e.g. acetylene – C_2H_2 and methane – CH_4) and a catalytic metal surface (copper or nickel) inside a reaction chamber with controlled temperature, pressure, and gas flow rate conditions. Figure 2.14 shows a typical CVD instrument with all of its components. Two CVD processes are used to activate the carbon source: thermal CVD and plasma-enhanced CVD (PECVD) [16], [17].

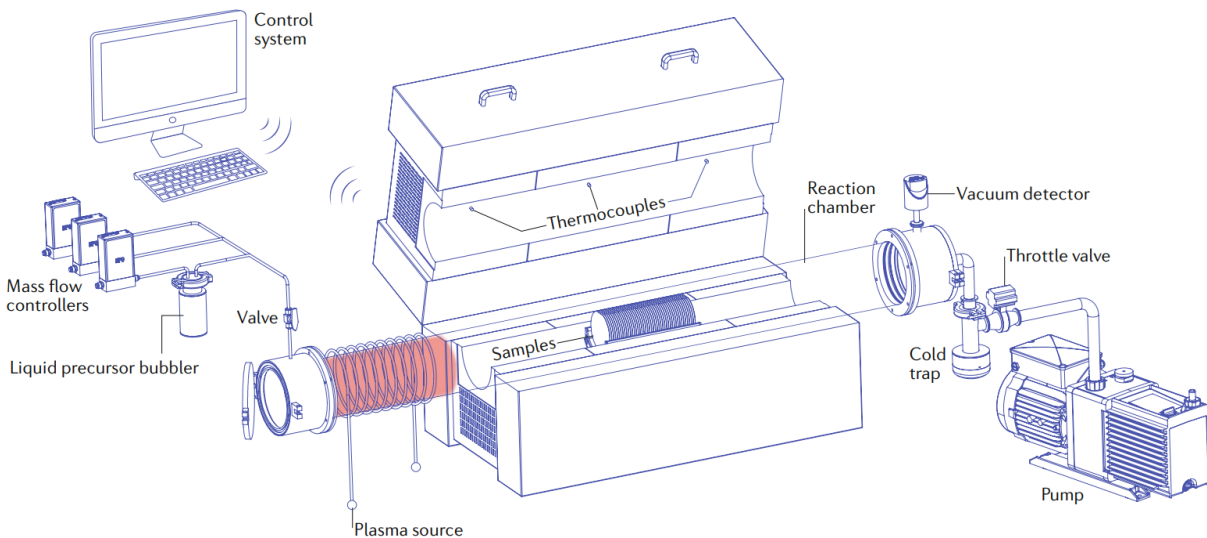


Figure 2.14: Schematic diagram of a typical CVD equipment [18]

In thermal CVD a high-temperature heating furnace ($900 - 1100^{\circ}C$) activates the carbon-containing gasses reactants and is the main driving criterion for the reaction. In PECVD, the

decomposition of the gas source is accomplished by plasma. The ability of PECVD to produce graphene at low pressure and temperature gives it an advantage over thermal CVD [16], [43].

Figure 2.15 shows thermal-CVD and plasma-enhanced CVD methods schematically.

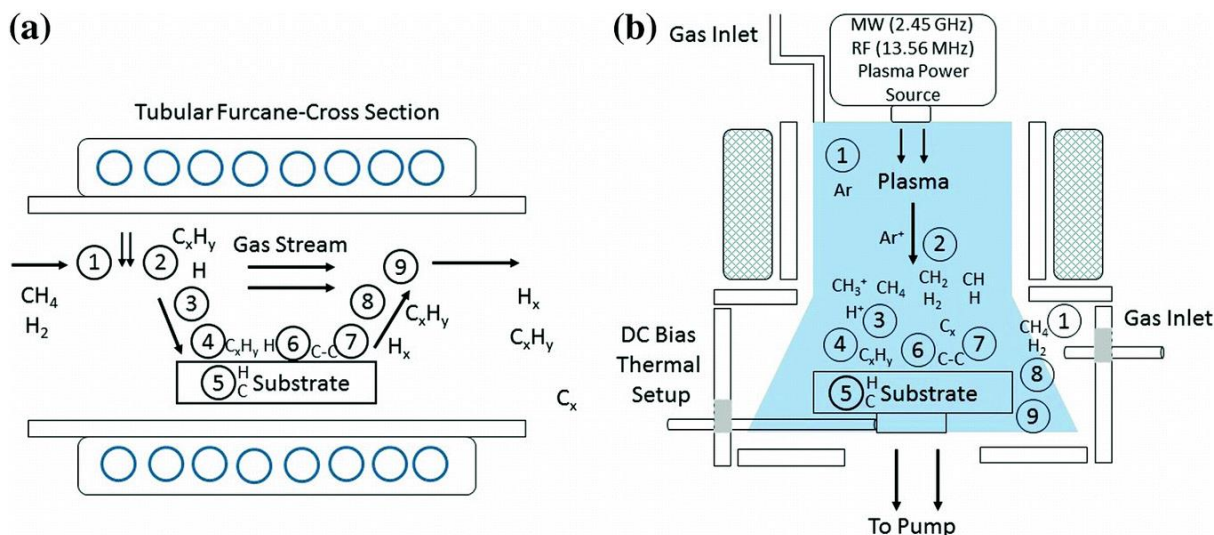


Figure 2.15: (a) Thermal and (b) Plasma enhanced CVD diagrams: 1. Forced convection reactant transport, 2. Thermal (a) plasma or (b) activation, regulation of kinetic parameters, 3. Transport of reactants to the substrate, 4. Reactant adsorption on the surface of the substrate, 5. Depending on the physical characteristics and solubility of the substrate, species will dissolve and diffuse in bulk, 6. Growth of the graphene film: chemical catalytic reaction, surface activation, bonding, and heterogeneous surface reactions 7. Desorption of by-products. 8. Transport of by-products to main gas stream 9. Removing by-products off the deposition region [43]

2.3.3 Vacuum Epitaxial Growth

Using the epitaxial growth approach is another method of producing graphene. For this method silicon carbide (SiC) coated on a silicon wafer is the initial material. Applying high temperatures forces silicon and carbon atoms to break apart. To prevent contamination, the heating process – either resistive or e-beam heating – takes place in a vacuum. Temperatures exceeding 1000° K cause the silicon atoms to evaporate, leaving just carbon atoms and eventually, graphene is formed on the substrate. Regardless, structural flaws are inevitable since carbon atoms are easily burnt due to the high temperatures, resulting in contamination of the graphene with oxygen and hydrogen [17].

Table 2.1: Advantages and Disadvantages of the aforementioned graphene growth techniques [44]

Production method	Advantages	Disadvantages
-------------------	------------	---------------

2.3 Growth Mechanisms of Graphene

Top down	Mechanical exfoliation	<ul style="list-style-type: none"> • Easy and affordable • Good for presenting purposes • Enough to study properties of graphene 	<ul style="list-style-type: none"> • Not efficient for large quantity production • Produces primarily few-layer to many-layer graphene • Dimensions limited by original crystal size
Bottom up	Chemical Vapor deposition	<ul style="list-style-type: none"> • Large area graphene production • Large single-crystal growth • Single or few layers graphene • Transferable to arbitrary substrate with ease 	<ul style="list-style-type: none"> • Still slightly costly • Transfer can damage and contaminate graphene sheets
	Vacuum Epitaxial Growth	<ul style="list-style-type: none"> • Large area graphene production • Single or few layers graphene • Growth on insulating substrate • Transferable to arbitrary substrate with ease 	<ul style="list-style-type: none"> • Requires really specialized facilities • Very expensive • Single crystal size limited to SiC size

3 Liquid Gated Graphene Field Effect Transistor (LG-GFET)

Graphene's electric field effect was one of the remarkable findings presented by Novoselov et al. [20]. Consequently, a great amount of study has been done on graphene field effect transistors (GFETs), where the channel material is graphene. Initially, graphene on Si/SiO₂ substrate was used to create back-gate devices, with silicon and silicon dioxide acting as the back gate electrode and dielectric, respectively, following the usual structure of traditional FETs. It did not take long for the first top-gate graphene field effect device to appear in 2007 [21].

In this chapter, the foundational principles of GFETs operation will be presented and compared to classic FETs. The attention is mainly directed towards liquid gated GFETs, which hold significant promise for biomedical and biosensing applications. Furthermore, an in-depth analysis of the structure of the INL chip, used in this work, will be provided.

3.1 Basics of GFETs

A FET is a three terminal electronic device where the conductivity between two terminals: the source and the drain, is regulated by the electric field created by the third gate terminal. The gate functions as a control that allows high current or low current conduction, enabling the FET to be used as a switch. In terms of physics, this control is accomplished as the gate modulates the free carrier density in the channel between the source and the drain, which conventionally is doped silicon [19]. In Figure 3.1 the structure of a traditional metal oxide semiconductor FET (MOSFET) is depicted [45].

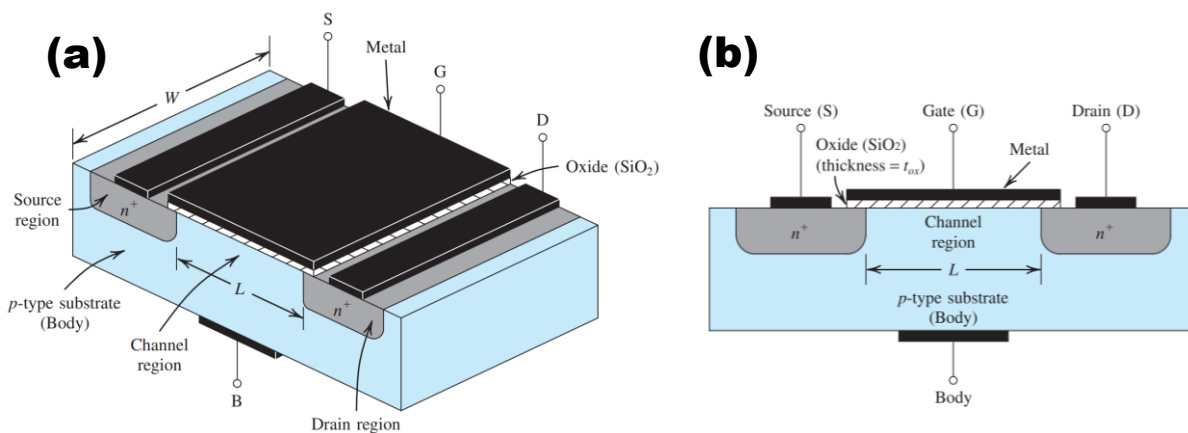


Figure 3.1: Physical structure of the enhancement-type NMOS transistor: (a) perspective view, (b) cross section [45].

Unlike traditional MOSFETs, in GFETs the channel is just graphene. The first reported [20] graphene FET device is depicted in Figure 3.2.a. Following the conventional FET structure, the back-gate dielectric was a SiO_2 layer below the graphene channel and a doped silicon substrate acted as the back-gate. This is a very useful device for proof-of-concept purposes, but it has large parasitic capacitances. Therefore, in 2007 [21] a new structure, with top-gate, was introduced [22].

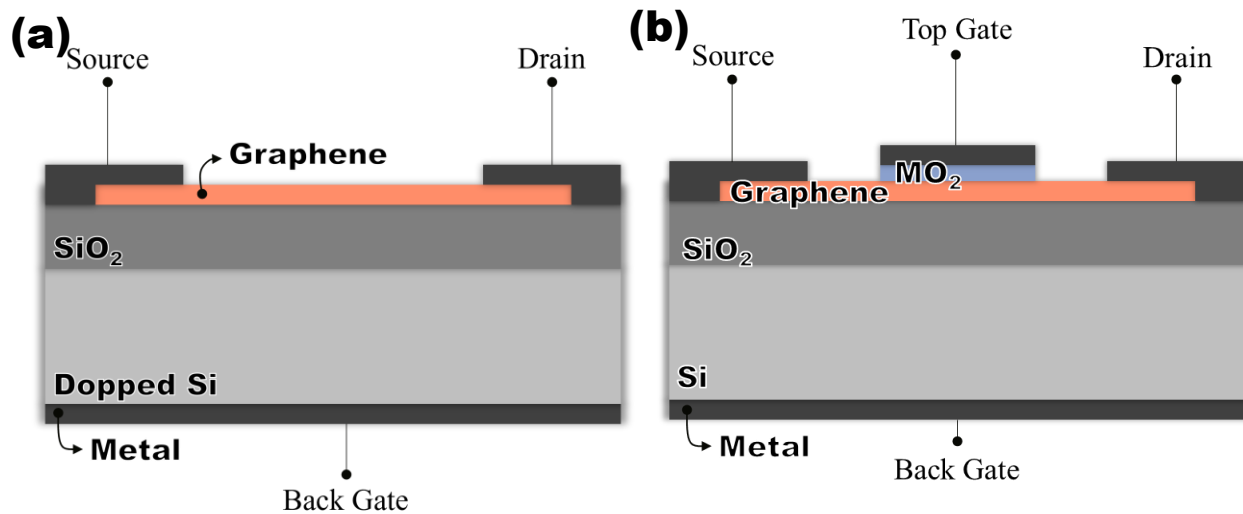


Figure 3.2: Structure of a GFETs: (a) back-gated, (b) top-gated [22].

In conventional FETs current flows through the channel only in the presence of gate voltage (positive for NMOS occasion, negative for PMOS occasion), on the contrary graphene is conductive by nature and therefore in GFETs there is always a small current flow. Additionally, in GFETs the graphene channel is activated for both positive and negative gate voltages. All the aforementioned phenomena lead to a unique current-voltage transfer characteristic (Figure 3.3.a) [22].

In GFETs the applied gate voltage determines the type of the carriers (electrons or holes) in the channel. Large positive gate voltages result in electron accumulation in the channel, while large negative gate voltages lead to hole accumulation (absence of electrons). These 2 types of conduction result in the two branches of the $I_d - V_g$ curve separated by a charge neutrality point or as called Dirac point (Figure 3.3.a). The Dirac point's location is determined by several factors: the type and density of the charges at the interfaces at the top and bottom of the channel, and any doping of the graphene. For FET devices with large-area graphene channels, on-off ratios have been reported in the 2–20 range, that is way too low for them to be used in logic circuits [22].

The change of the graphene's fermi level (Figure 3.3.b) is noteworthy. For $V_g > V_{g,dirac}$, the fermi energy increases: the valence band penetrates into the initial conduction band and leads to electron conduction. On the other hand, for $V_g < V_{g,dirac}$ the fermi energy decreases and the valence band shrinks, leading to holes conduction [23].

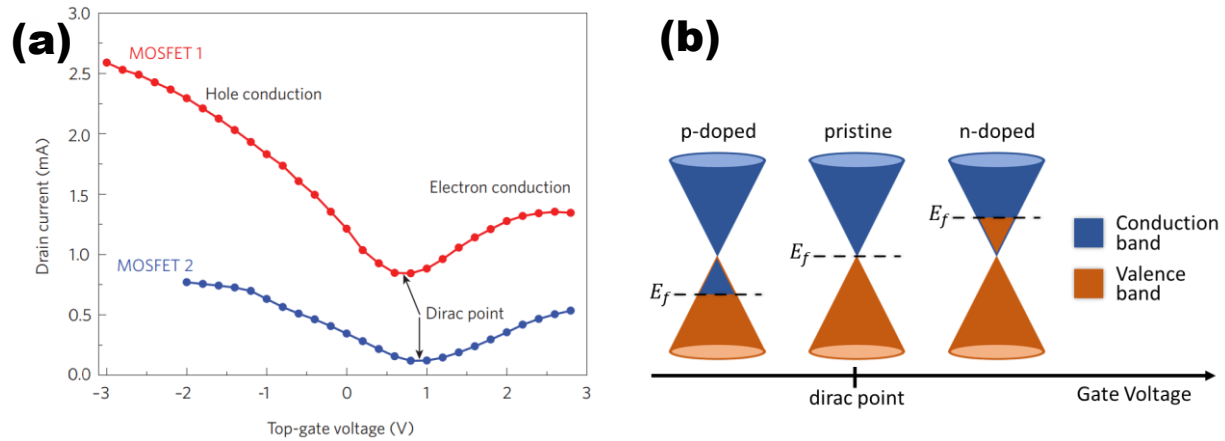


Figure 3.3: (a) Typical transfer characteristics for two GFETs [22], (b) the change in the Fermi level of graphene with applied gate voltage

The positive voltage applied to the back gate creates an electric field that attracts electrons away from the carbon atoms. This process is known as electrostatic doping. In more detail, Figure 3.4 illustrates what happens to the device when $V_g > 0$ is applied. The positive gate voltage attracts the electrons and, consequently, generates positively charged carriers called "holes" below the SiO_2 . Accordingly, the holes attract the negative charges of the SiO_2 leaving an abundance of positive induced charges just under the graphene. These positive charges attract the electrons of the graphene, and thus isolates them off the carbon atoms, allowing them to move under the application of a bias drain voltage. Applying a negative gate voltage has the opposite effect and leads to holes conduction. In the occasion where both gates are being used, the one "helps" the other leading to same current conduction with lower applied voltage at both gates.

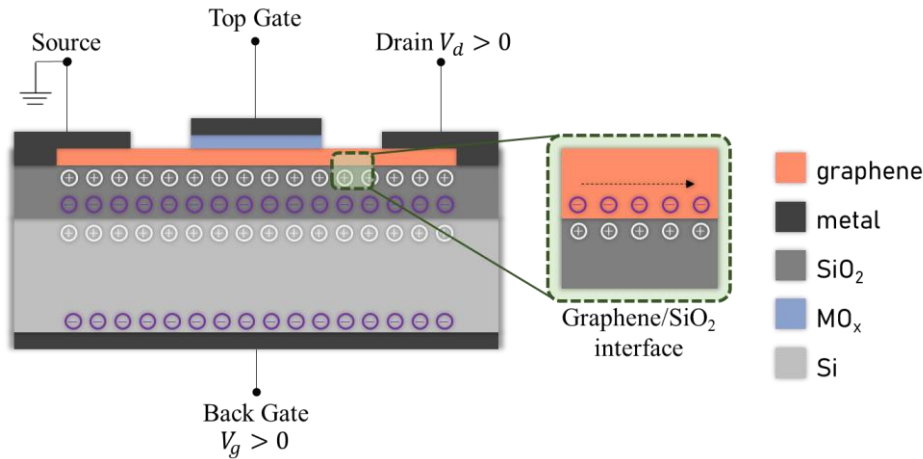


Figure 3.4: The effect of $V_g > 0$ in the back gate of a GFET

The application of drain voltage is necessary to observe the movement of the carriers. There are three zones that make up the $I_d - V_d$ characteristic of monolayer graphene: the triode region, the unipolar saturation region, and the ambipolar saturation region. Figure 3.5 illustrates the phenomena in each section. In region I (triode region) current is carried by either holes or electrons throughout the length of the channel, the curve is linear and so the graphene acts as an ohmic resistor. As V_{ds} increases, the drain current saturates and eventually reaches the unipolar saturation region (region II) at the inflection point ($V_{ds} = V_{ds,crit}$) and the channel is pinched at the drain end. When V_{ds} surpasses $V_{ds,crit}$, the transistor enters the ambipolar saturation region (region III). Within this bias range, the carriers in the channel are both electrons and holes [22], [24], [25].

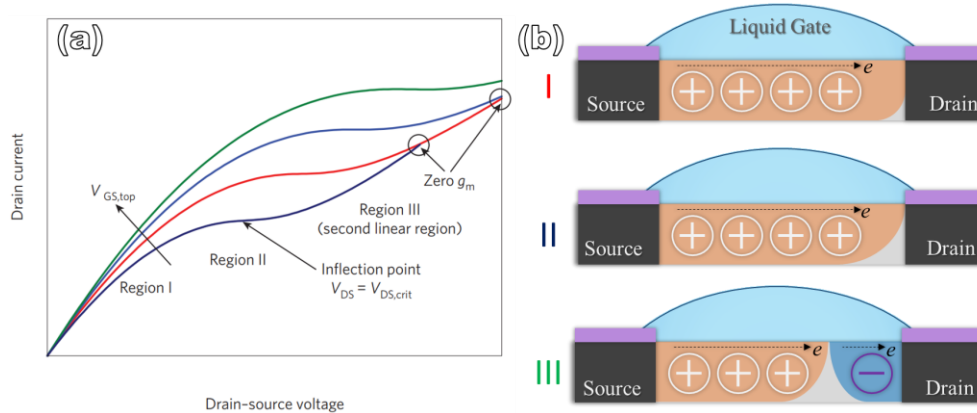


Figure 3.5: (a) Typical output characteristics for different V_g [22], (b) illustration of the carrier concentration beneath the top-gated region: for $V_{ds} < V_{ds,crit}$ (region I) the channel charge at the drain end begins to decrease as the minimal density point enters the channel, for $V_{ds} = V_{ds,crit}$ (region II) the minimal density point forms at the drain and for $V_{ds} > V_{ds,crit}$ (region III) an electron channel forms at the drain [25].

3.2 Liquid gate GFETs

Expanding the top gate GFET technology, the commonly used solid dielectrics can be replaced by a liquid (liquid-gate GFET, LG-GFET). In such configurations, the transistor is capable to operate at very low voltage, because the gate potential is applied in the nanometer-thick electrical double-layers (EDL) forming at the solid – electrolyte interfaces. The possibility of detecting small changes in GFET transfer characteristics paves the way for ultrasensitive biosensing [26]. In Figure 3.6 a LG-GFET with a reference gate electrode is displayed.

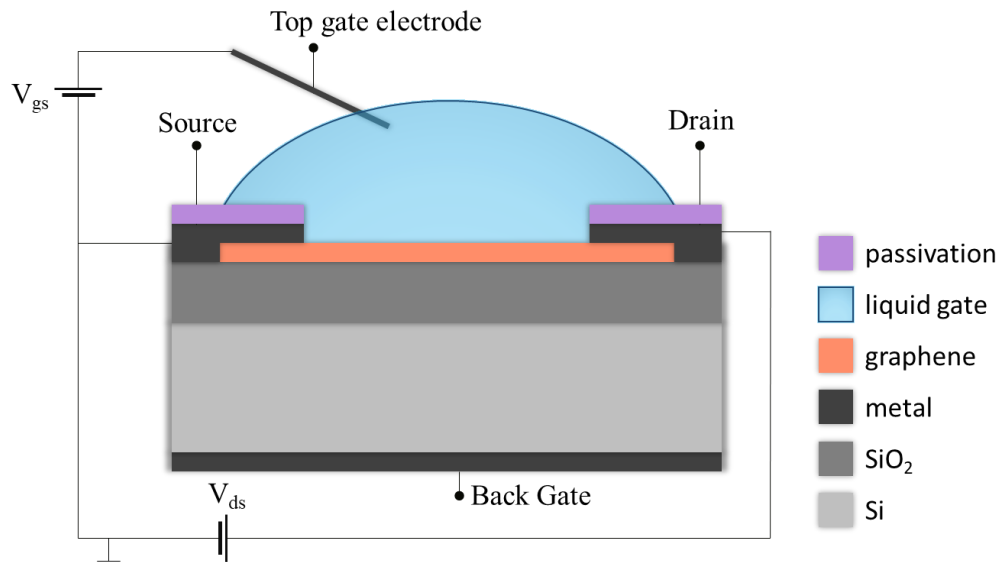


Figure 3.6: Liquid gate GFET configuration with reference gate electrode

The principles of operation for LG-GFETs do not differ from back-gate GFETs presented in subchapter 3.1 in Figure 3.4. In LG-GFETs the liquid acts as an insulator accordingly to the SiO₂ in back-gate GFETs. The synchronous use of the top gate electrode and the back gate can enhance the operation of the above configuration as the activation of graphene's electrons will be double.

3.3 GFET applications

GFETs exhibit a diverse array of applications, spanning from biosensors tailored for specific targets to the acquisition of neural signals. Particularly noteworthy is their ability to detect disease biomarkers, often present at ultra-low concentrations during the initial stages of illness manifestation. GFETs offer an optimal solution for biosensing, as they present a wide linear detection ranges, better sensitivity, and rapid detection making them ideal to be used as sensing devices [27].

Exploring further into the implementation, biomolecule receptors that can selectively bind to the target biomolecules in a solution, such as antibodies or single-strand DNA probes, can be used to chemically functionalize graphene. As the target biomolecules attach to their acceptors, changes in characteristic curves of GFETs can be noticed (Figure 3.7). Consequently, the chemical modified GFET can transduce the biological signal into an electrical signal and detect the binding events [27]. An example development of a GFET biosensor is presented in Figure 3.8. This principle can be expanded to detect SARS-CoV-2 [28] and other biomolecules [29], [30].

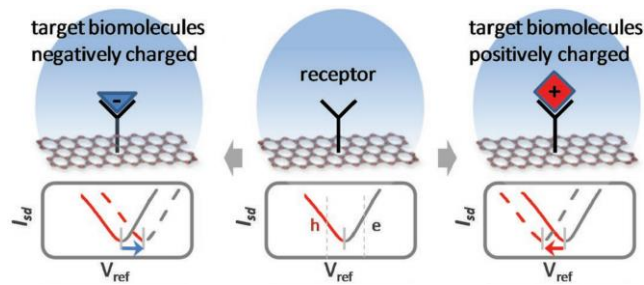


Figure 3.7: Sensing principle of GFET biosensor [29].

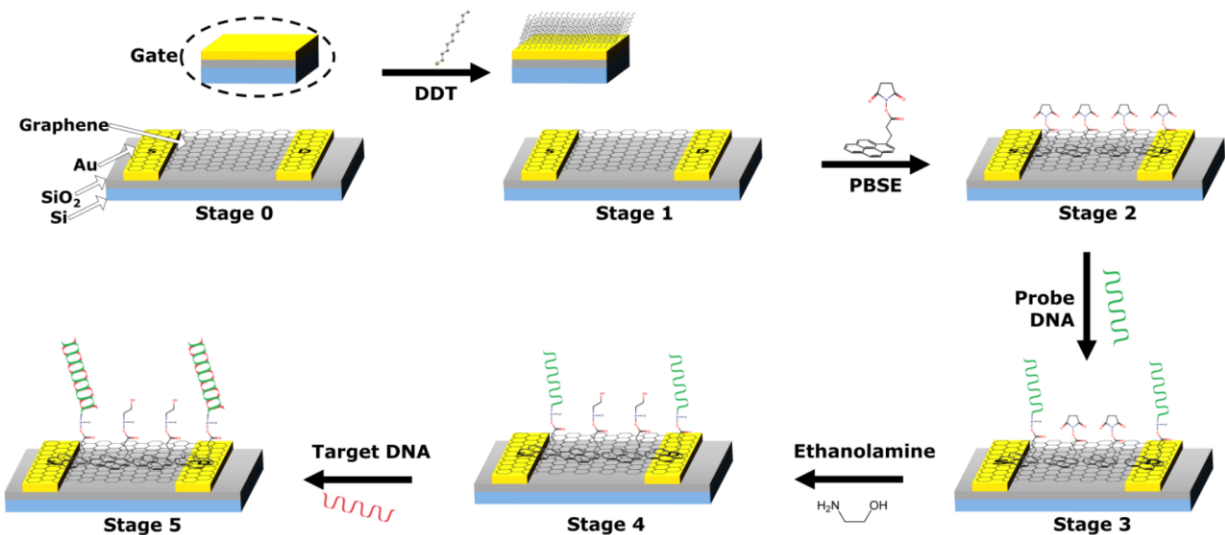


Figure 3.8: Diagram outlining the progress of biosensor development. Stage 0: Initial graphene transistor, Stage 1: Implementation of 1-Dodecanethiol (DDT) gate passivation, Stage 2: Introduction of 1-pyrenebutyric acid succinimidyl ester (PBSE) linker immobilization, Stage 3: Functionalization with probe DNA, Stage 4: Application of ethanolamine blocking, Stage 5: Initiation of biorecognition process [46].

Beyond biosensors, GFETs have also shown promising applications in the field of neural interfaces [31], [32]. The research conducted by Blaschke et al. [32] represents a significant

milestone in the field of neural prostheses by utilizing arrays of flexible graphene field-effect transistors (GFETs) for mapping brain activity. The successful recording of in vivo brain activity demonstrates the potential of GFET technology to compete with existing microelectrode-based recording methods while offering unique advantages such as intrinsic signal amplification and the ability for high-density integration. Furthermore, the combination of graphene with other 2D materials like boron nitride substrates is expected to further improve the mobility and decrease noise in flexible LGFETs, potentially enabling the detection of single unit activity directly from the brain surface [32].

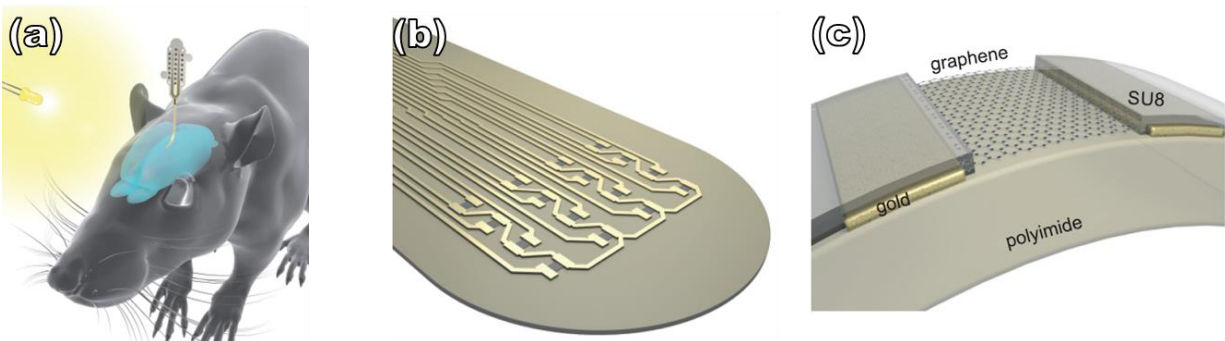


Figure 3.9: (a) representation of the implant placed on the surface of the rat's brain (b) representation of the head of a graphene implant showing a 4×4 graphene transistor array and feed lines, (c) cross section of a flexible graphene transistor with graphene between the source and drain contact that are covered by an insulating SU8 photoresist [32]

Concluding, GFET biosensors are especially appealing for point-of-care diagnostics because of their miniaturization, low manufacturing costs and compatibility with semiconductor manufacturing processes. It is for these reasons that many GFET biosensors have already been created and documented in literature [27]. Actually, a search for "graphene field effect transistors" in the NCBI PubMed Central database¹ turned up 1686 results and more than 6597 results were found when the search was generalized to "graphene biosensors".

3.4 INL GFET chip

In the present work a chip with GFETs (Figure 3.10) manufactured from the Iberian Nanotechnology Laboratory (INL) [26] is used and thoroughly analyzed. This chip incorporates 20 double gate GFETs consolidating the complexity of electrical measurements and enhancing

¹ <https://pubmed.ncbi.nlm.nih.gov/>

integration capabilities. The core of the chip (Figure 3.10.b) consists of a silicon substrate on top of which the GFETs are manufactured. Notably, the core structure is symmetrically divided into two sides, each featuring a shared source electrode interconnecting 10 GFETs, summing up to in total 20 devices in one chip. Through wire bonding and PCB techniques the electrodes are wired to the pins of the chip (Figure 3.10.f).

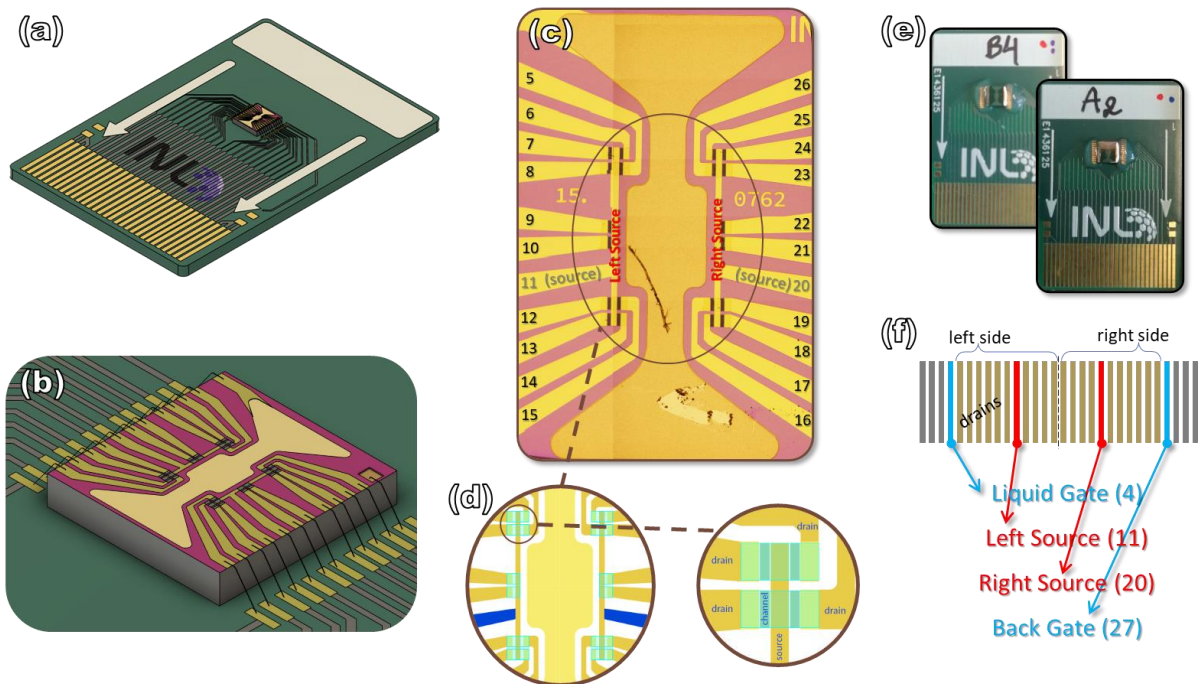


Figure 3.10: a) 3D illustration of the GFETs chip, b) close-up 3D illustration of the 20 GFETs, c) collage of optical microscope images showing the 20 devices with numbers indicating correspondence to pins, d) illustration of the 20 GFETs and close up of the graphene sheets, e) photograph of the chips, and f) pins to electrodes correspondence mapping.

LG-GFETs are commonly manufactured without the reference gate electrode and an external metallic wire is then added for measurements (Figure 3.6). The under-discussion chip allows for flexible transistor layout design and planar technology single-lithographic mask contact fabrication by integrating the gate electrode into the wafer and making it coplanar with the source and drain electrodes [26].

Liquid gating in graphene field-effect transistors involves exposing semiconductor materials to liquid solutions, which are prone to attack semiconductors. To minimize such effects, passivation of all surfaces interfacing with the solutions, excluding graphene, is essential. This passivation not only protects against destruction but also allows the deployment of liquid solution over numerous

devices, ensuring minimal cross-talk, leakage current, drift induced by ion diffusion, and electrode damage [26].

In LG-GFET fabrication, graphene transfer constitutes a pivotal stage. Graphene synthesized via thermal chemical vapor deposition (CVD) on copper catalysts or silicon face of silicon carbide (SiC) wafers stands as the preferred choice, offering high-quality graphene over large areas. Despite wet transfer methods showcasing promise for large-scale GFET fabrication, challenges concerning surface contaminants exist and are often overlooked in biosensing applications. Hence, meticulous attention to surface purity is imperative to ensure the integrity and functionality of GFETs, particularly in biosensing contexts. To avoid such negative effects, it is important to minimize lithographic processes with aggressive patterning steps post graphene transfer on the wafer, as they increase residue accumulation on graphene [26].

Figure 3.11 summarizes the fabrication process of the INL GFETs chip. Initially a hole in the Si/SiO₂ substrate is created to reach the Si and create the back gate contact. Then, the Cr/Au contacts are created, leaving a 75 μm (channel width, W) by 25 μm (channel length, L) gap. After that, a sacrificial layer is deposited on the device, except where the graphene will be. The crucial step of the graphene transfer, with the PMMA on top, is next. Afterwards the PMMA is removed off the graphene and the sacrificial layer is destroyed leaving the chip as it is depicted in Step 4 of Figure 3.11. Following, a stopping layer of Cu is deposited to protect the graphene and the gate contacts from the passivation. Lastly, the passivation layer consisting of SiO₂ and SiN_x interchanging layers is deposited and the stopping layer is removed [26].

3.4 INL GFET chip

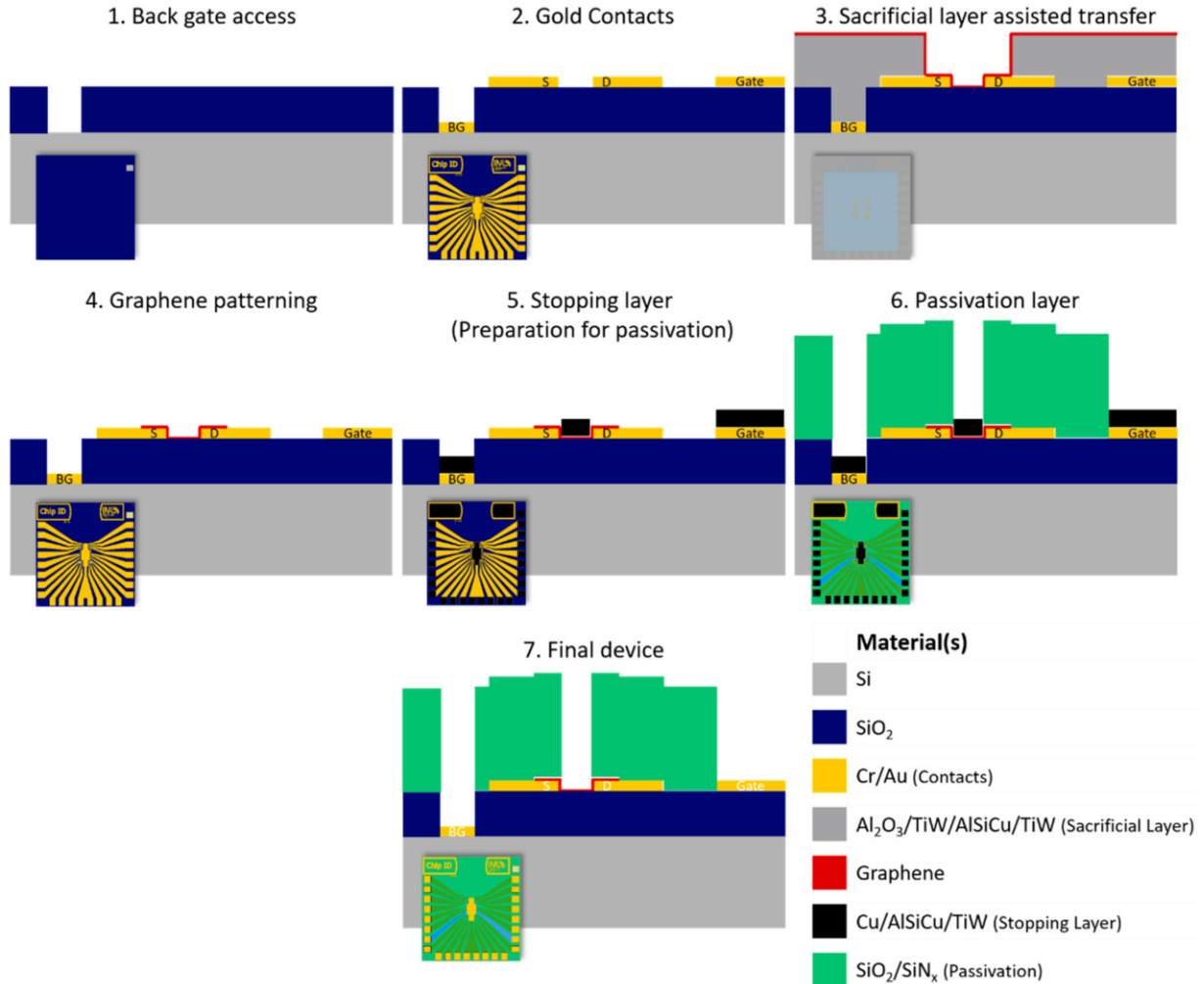


Figure 3.11: Graphical summary of the fabrication process for production of LG-GFETs for biosensing at wafer-scale. In detail: Steps 1 and 2: contact patterning, Step 3: Graphene Transfer (to prevent transfer-borne residues on gold surfaces, a sacrificial layer is used), Step 4: Graphene patterning (Following full transfer and the removal of PMMA, dry etching is used to pattern the graphene and the sacrificial layer is removed), Step 5: Stopping layer; Step 6: Deposition and dry etch patterning of the passivation layer, and Step 7: Remove of the stopping layer [26].

4 Electrical Characterization

In this chapter the focus shifts from the theoretical to the practical field, as the electrical characterization of graphene field effect transistors will be analyzed. The methodology used for electrical measurements is discussed in detail, describing the experimental setup and measurement procedures. In addition, the chapter clarifies how useful quantities extracted from the characteristic curves $I_d - V_d$ and $I_d - V_g$ are, providing information on the electrical performance of the GFET. Parameters such as conductivity, transconductance and graphene resistance are thoroughly examined. Finally, quotes are given on the influence of the present chips on the number of measurements performed on them and the influence of ambient air on them. The chapter lays the foundation for a comprehensive analysis of the electrical behavior and performance characteristics of the graphene transistor.

4.1 Measurements methodology

4.1.1 Experimental Setup

All measurements presented in this thesis are executed in the “*Electrical Characterization Lab*” in the INN of NCSR “*DEMOKRITOS*”. For the $I - V$ curves the HP 4155A Semiconductor Parameter Analyzer (Figure 4.1) was used. The HP 4155A is an electronic instrument for measuring and analyzing the characteristics of semiconductor devices. It can execute full sets of measurements as it can be connected to LabView software or use the preinstalled measurements formats.

For the experiments of this thesis 3 Source Measure Units (SMU): SMU1, SMU2 and SMU3 are used for the source, gate and drain of the GFET accordingly. The SMUs can be set as variables, constants or ground. In total 3 different types of measurements were executed: normal sweep, double sweep and sampling. In the case of sweeps the drain and the gate (SMU1 and SMU2) were set as variables and the source (SMU3) as ground. Both sweeps need a starting point, a step and the number of steps for the variables. There is also a choice for compliance current, which is a current limit where the measurements stop in order not to cause damage to the under-measurement device. For the sampling measurements the gate and the drain were set as constants and the source as ground, while the drain current was measured per time.



Figure 4.1: HP 4155A Semiconductor Parameter Analyzer

The HP4155A was connected to a micromanipulator prober station located inside a dark box (Figure 4.2, Figure 4.3). The prober station offers 4 tungsten probes, of which 3 were used. For the probes to be placed correctly on the sample the offered microscope and placement-adjust screws were used. The base of the probes station has negative pressure pumps that provide the necessary stability to the samples. The dark box offers good light, electromagnetic and humidity insulation for quality measurements.

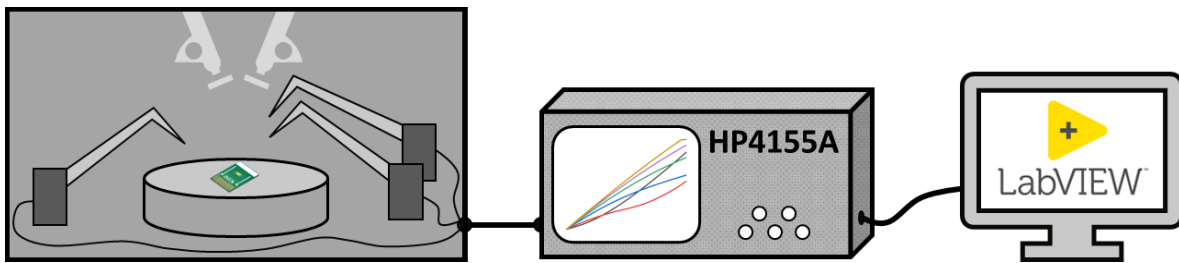


Figure 4.2: Experimental setup for $I - V$ curves.

The data derived from the LabVIEW software were managed through specialized user interfaces (UIs) specifically developed for the purposes of this study. After importing the raw data into the interface, various analyses were conducted, including the generation of plots, processing of data, extraction of parameters, and creation of summary plots. These UIs were constructed utilizing the Python programming language. The code for the UIs as well as supplementary scripts that were used for data analysis are uploaded in [this repository](#).

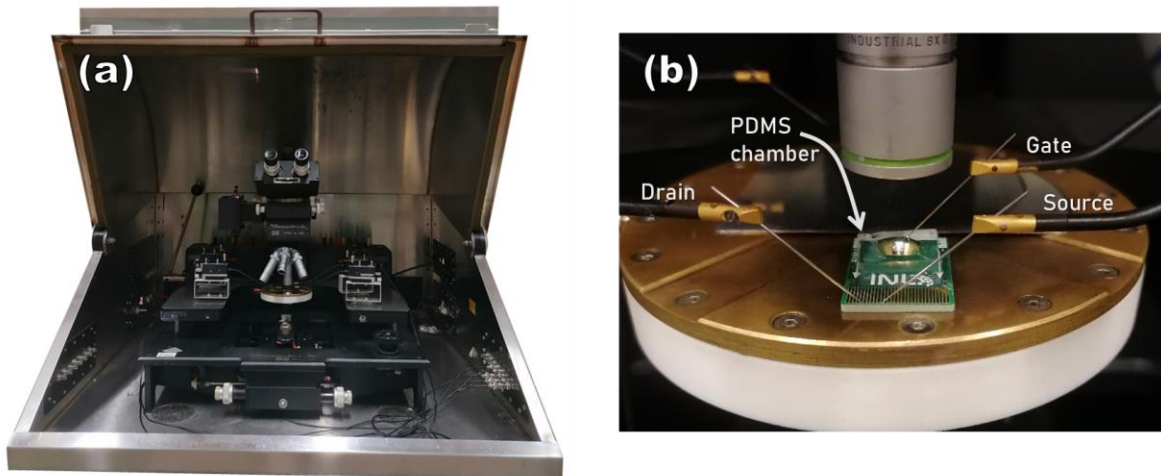


Figure 4.3: (a) Micromanipulator probe station and (b) placement of the probes on the INL chip.

Additionally, $C - V$ curves were retrieved to experimentally measure the capacitance of the top gate liquid to the gate electrode. The HP4284A LCR meter (Figure 4.4) was used to obtain these data. During the measurement a DC voltage is applied, to which a small amplitude AC voltage is added (the amplitude of the AC signal is small so that the response is linear). Applying this voltage causes a change in the load ΔQ of the device and through this the capacitance is calculated. For this kind of measurements only 2 probes were used: one was just touching the liquid and the other was touching the 4th pin of the packaged chip, which is the coplanar top gate electrode pin. The extracted plot is shown in Figure 4.25.



Figure 4.4: HP4284A LCR meter

4.1.2 Experimental details

The source of each FET was taken as a reference point for all measurements. So, when the notation V_d is used, it refers to V_{ds} , when the phrase voltage of the gate is used, it refers to the voltage difference between gate and source, and so on.

After testing the limits of the device used in this work it has been concluded that it is safe to work between $-0.5V$ and $+0.5V$ for drain voltage (V_d) and from $-1V$ to $+1V$ for gate voltage (V_g). As current compliance a limit of $800\mu A$ both for drain and gate current was set.

4.2 INL Chip preparation

The INL chip's soldering points, connecting it to the PCB, are safeguarded by an epoxy resin, forming a protective barrier against damage. This resin naturally forms a slight step, providing a small tank where droplets can rest on the transistor array. However, for the current experimental needs, a larger liquid volume is required. To accommodate this, a custom-made polydimethylsiloxane (PDMS) well with a capacity of 0.3ml was meticulously crafted and securely affixed to the INL chip.

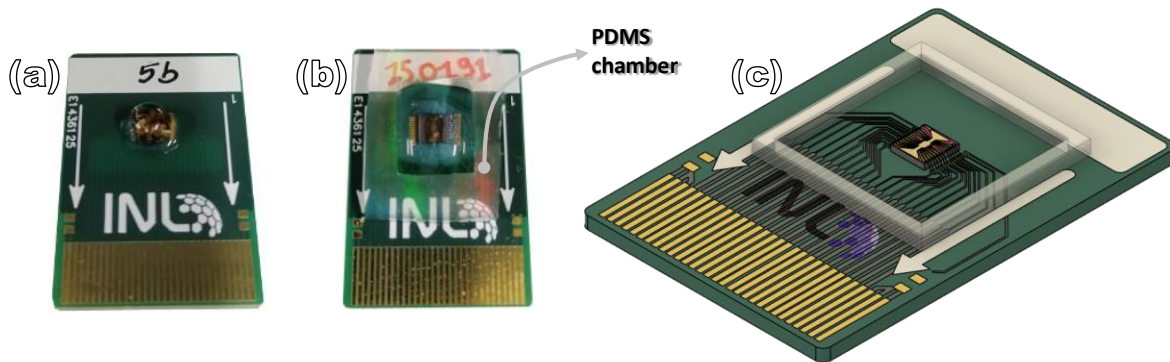


Figure 4.5: (a) INL chip with a drop of distilled water; (b) INL chip with PDMS chamber filled with distilled water; (c) illustration of INL chip with PDMS chamber

Silicone polymer Polydimethylsiloxane (PDMS), sometimes referred to as dimethicone or dimethylpolysiloxane, is a silicone polymer with a broad range of applications, including industrial lubrication and cosmetics. In general, PDMS is non-toxic, non-flammable, and optically clear. Its uses include elastomers, medical equipment, and contact lenses. $CH_3[Si(CH_3)_2O]_nSi(CH_3)_3$, where n is the number of repeating monomer $[Si(CH_3)_2O]$ units, is the chemical formula for PDMS [47].

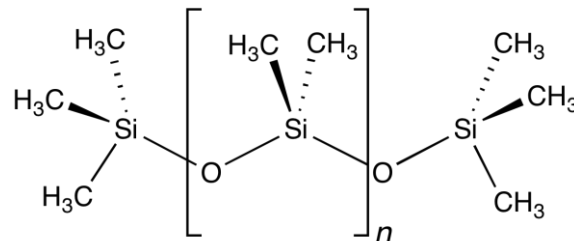


Figure 4.6: Chemical structure of PDMS [47]

4.3 Characteristic GFET curves

4.3.1 Transfer Characteristic ($I_d - V_g$)

To obtain the curves of drain current versus gate voltage ($I_d - V_g$), gate voltage from $-1V$ to $+1V$ was applied for drain voltages $0V$, $0.1V$, $0.2V$, $0.3V$ and $0.4V$. In addition, forward and backward sweep measurements were taken to observe any hysteresis effects.

From the $I_d - V_g$, the Dirac point voltage for every drain voltage and every GFET device can be extracted. The Dirac point voltage is located at the minimum point of the curve. Theoretically this point should be located where V_g is approximately $0V$ due to the symmetry of graphene's energy bands. However, when graphene is brought into contact with the contact's metal, as the Fermi Energies of the materials are equilibrating, the final Fermi Energy is smaller than the initial Fermi Energy of graphene. As a result, positive gate voltage should be applied so that graphene reaches the Dirac point [48]. Rather than that, any polymer residues (positive charges) or pollutants from the water and the air that attach to the graphene's surface are also conducting to the fall of Fermi Energy and consequently the move of the Dirac point as they remove electrons from the graphene [49]. All these lead to the conclusion that the graphene of the chips is slightly p-doped.

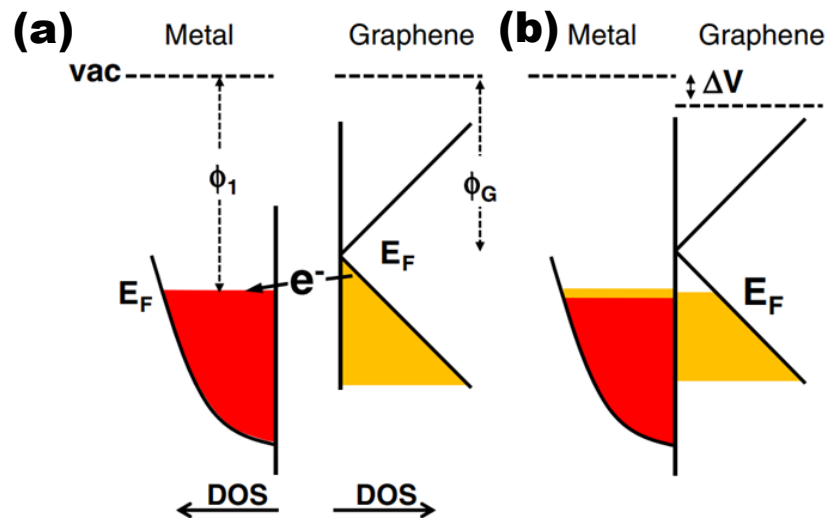


Figure 4.7: The relationship between the DOS¹ and the energy (a) in the contacts and in the graphene separately and (b) "just" at the metal/graphene interface.

¹ The density of states (DOS) is the number of different states at a given energy level that electrons are allowed to occupy.

4.3 Characteristic GFET curves

Figure 4.8 shows the $I_d - V_g$ curves for V_d from 0V to 0.4V for the FET 26_20 with the polymer chamber filled (0.3ml) with distilled water. For $V_d = 0V$ the drain current is, as expected, also 0. The Dirac point moves right with the increase of drain voltage. This is explained also due to the decrease of Fermi Energy as the voltage at the contacts increases. For devices with ambipolar characteristics, such as graphene, the lowest current is spotted where the gate voltage changes the Fermi level to the degree that the carrier injection between the source and the drain balances. Since the V_d modifies the carrier injection, the gate at which the current minimum is spotted will also change [33].

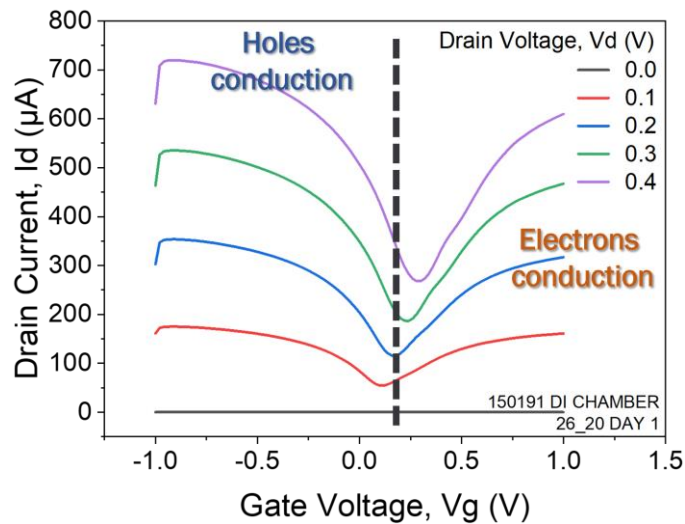


Figure 4.8: $I_d - V_g$ curves for V_d from 0V to 0.4V for the FET 26_20 with the polymer chamber filled (0.3ml) with distilled water.

Additionally, Figure 4.8 shows that the curves are not symmetrical as per the vertical axis that passes from the Dirac point. This asymmetry proves that the concentration and the mobility of electrons, that function as charge carriers for $V_g > 0V$, is smaller from the concentration and the mobility of the holes, that function as carriers for $V_g < 0V$.

Furthermore, in Figure 4.8 “cracks” in the right side of the curves are observed. To determinate the reason for these, measurements were repeated while alternating the source and drain terminals. In Figure 4.9 the same measurements have been made for source grounded (purple line) and drain grounded (grey line). If the phenomenon occurred due to a constructive error of the contacts, then by reversing the probes the “crack” should be transferred to the left branch. In the present measurements the “break” is maintained on the same leg and therefore there is no manufacturing error, but probably during the positive V_g there is a build-up of charges on the contacts.

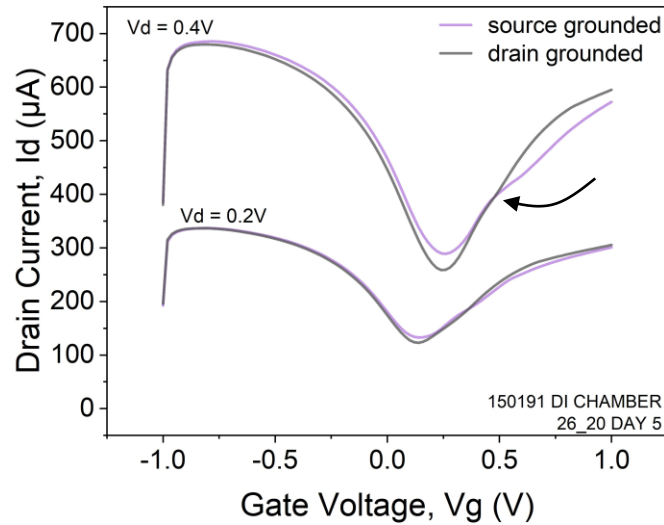


Figure 4.9: $I_d - V_g$ curves for source grounded (purple line) and drain grounded (grey line).

The forward and backward sweep curves (Figure 4.10) show that the devices do have hysteresis phenomena. The fact that during the backward sweep the curve is shifted to the left shows that during the measurements the Fermi energy increases due to the accumulation of negative carriers (electrons) at the graphene – distilled water interface. If the negative charges had accumulated at the graphene – silicon interface, then the hysteresis should be permanent. By repeated measurements it was observed that the hysteresis is not permanent and therefore, the shift is attributed to charge accumulation at the graphene – distilled water interface.

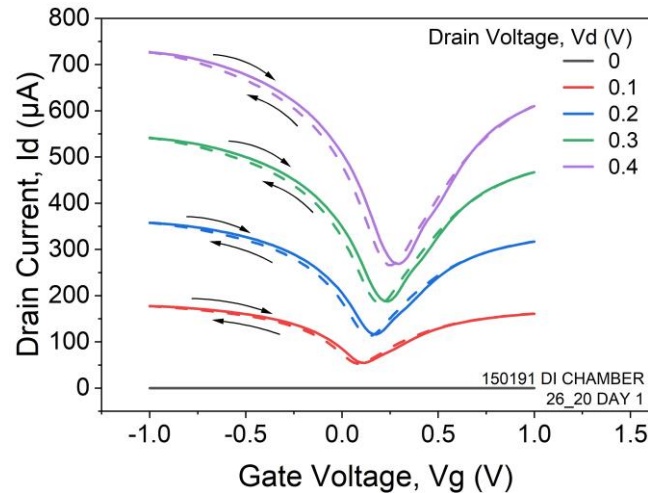


Figure 4.10: $I_d - V_g$ curves for forward and backward sweep.

All the measurements presented on this work are made using an external tungsten top electrode (Figure 4.3.b). However, as mentioned in section 3.4, the INL chip has embedded a coplanar Au/Cr top gate electrode. Figure 4.11 shows how the $I_d - V_g$ curves change depending on which electrode

4.3 Characteristic GFET curves

is used. Different gate electrodes have an impact on the Dirac point's location but not the drain current's magnitude (Figure 4.11.b). The external tungsten electrode has a better behavior while interacting with the distilled water as it is less polarizable and it has a better electrochemical equilibrium compared to the coplanar Au/Cr electrode. The effect of the different electrode materials is also shown in relevant literature [50].

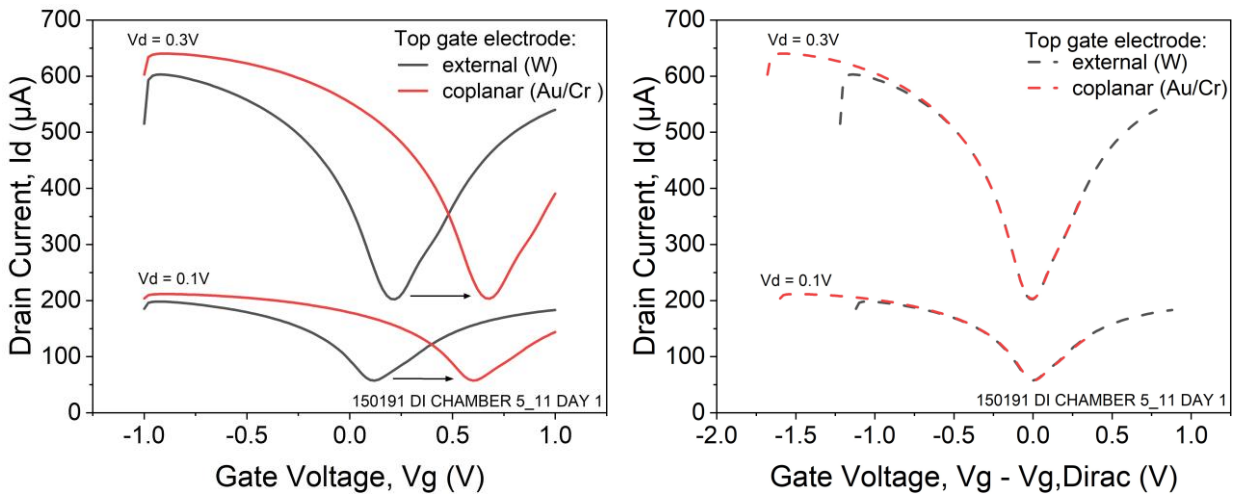


Figure 4.11: $I_d - V_g$ curves for different gate electrodes, in (b) the curves are shifted by $V_{g,\text{Dirac}}$ to show the same profile

Figure 4.12 illustrates the curves for all the devices (FETs) of chip 150191. Though theoretically, all FETs should have the same behavior, actual behavior varies from FET to FET of the same chip due to fabrication variations. One factor to which it could be attributed is wrinkles that are formed in the graphene during the wet transfer process. The FET 10_11 (source_drain) is observed to directly reach the compliance limit ($800\mu\text{A}$) indicating that this pair does not function as a FET. The Dirac points of the FETs typically lie within a narrow range with little variation. Notably the curves of some pairs, that are spatially close at the chip (e.g., 5_11 and 6_11, 18_20 and 19_20) are presenting identical behavior. This supports the claim that graphene regions with spatial proximity exhibit similar behavior.

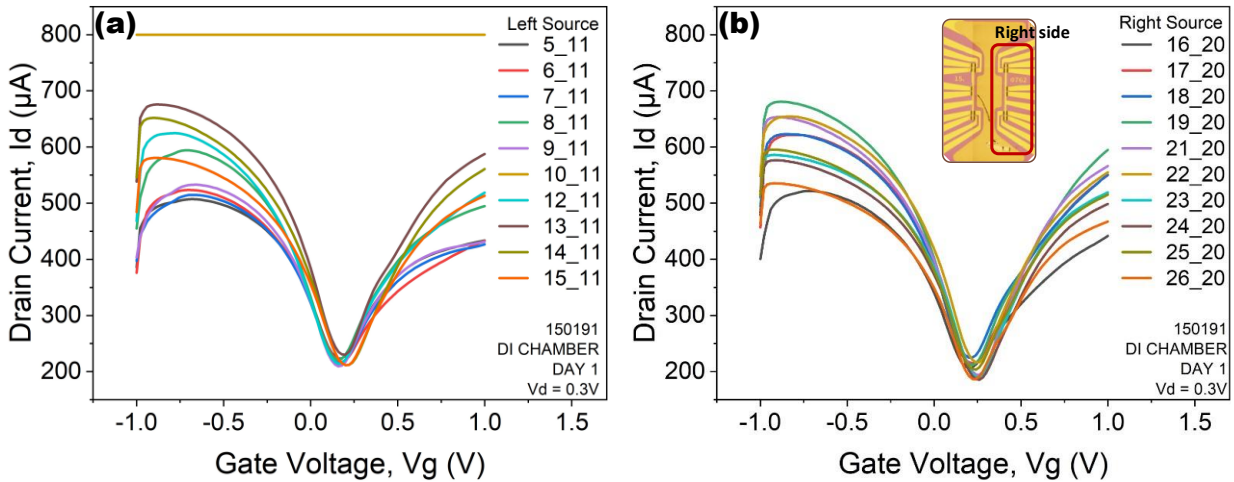


Figure 4.12: $I_d - V_g$ curves for $V_d = 0.3V$ for the left (a) and the right FETs (b) of the chip 150191.

In order to better observe in what interval, the Dirac points lay and what is the drain current at it, box charts were created as shown in Figure 4.13. It is noticed that the variation of the gate voltage and the drain current at the Dirac point increases as the drain voltage increases.

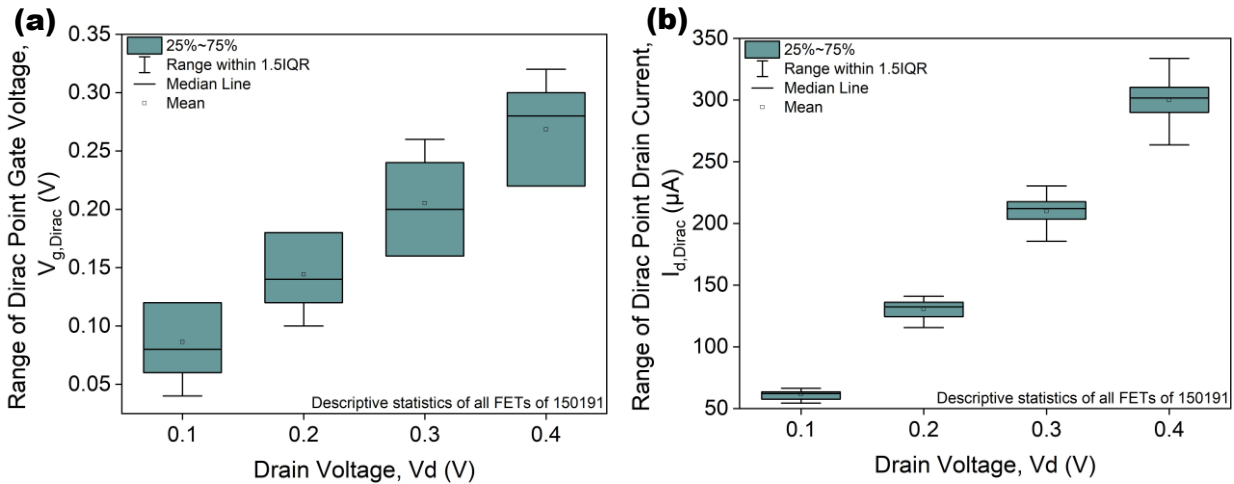


Figure 4.13: Box charts for gate voltage (a) and drain current (b) at the Dirac point.

In Figure 4.14 and Figure 4.15 and the $I_d - V_g$ curves for all the devices (FETs) of chips 150431 and 150439, under the same conditions in which chip 150191 was measured, are presented. In both chips a quite different behavior is noticed between the left and the right side. Particularly, in chip 150431 the curves of the right side seem to be shifted to the right and “unsharpened”, indicating possible positive contamination of the graphene surface.

4.3 Characteristic GFET curves

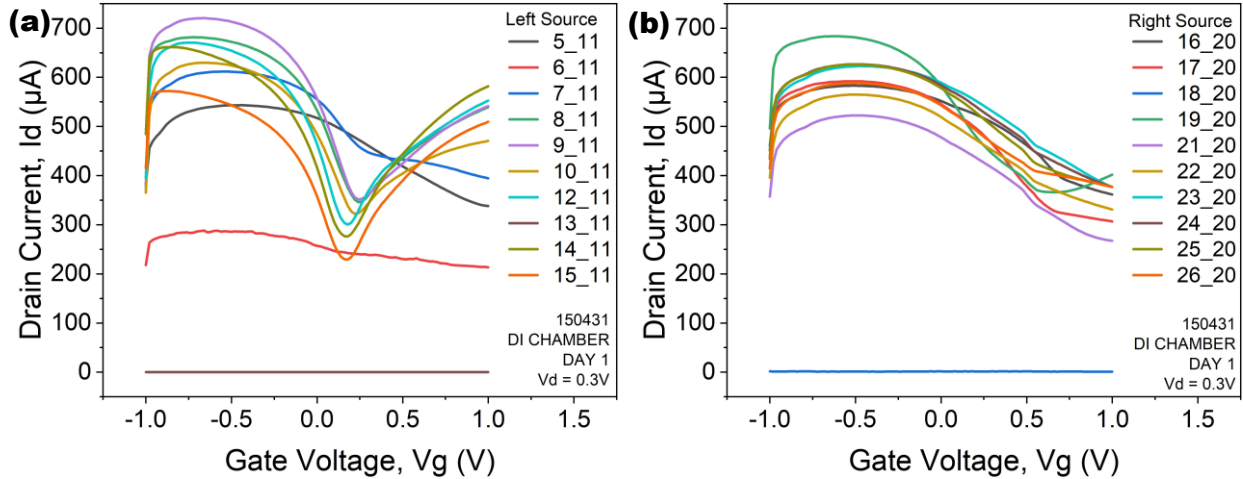


Figure 4.14: $I_d - V_g$ curves for $V_d = 0.3V$ for the left (a) and the right FETs (b) of the chip 150431.

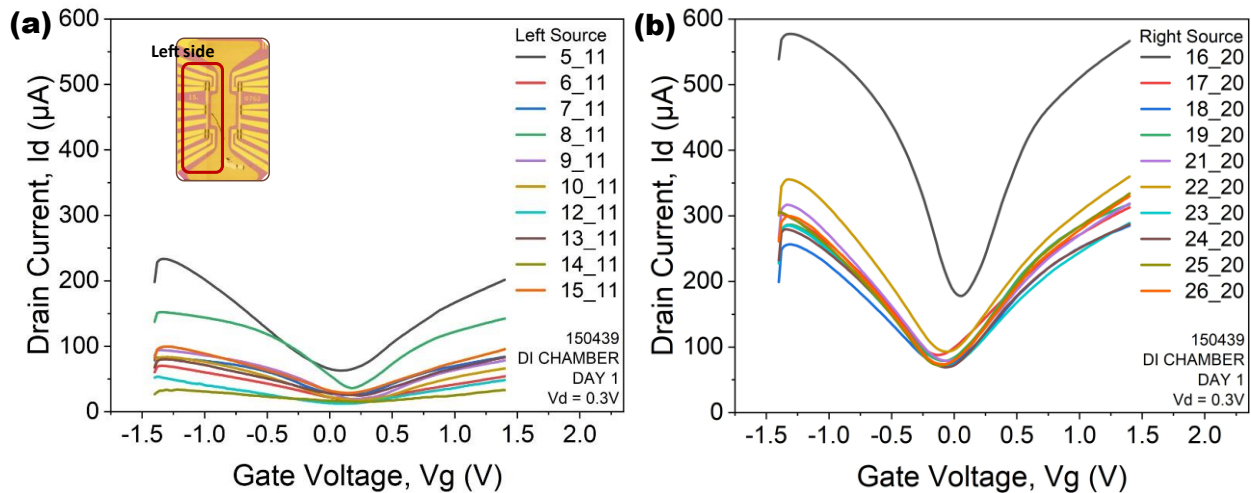


Figure 4.15: $I_d - V_g$ curves for $V_d = 0.3V$ for the left (a) and the right FETs (b) of the chip 150439.

Noticing the curves from all 3 chips a non-uniform behavior is concluded. Small differences during the fabrication, contamination and flaws on the graphene sheet are possible causes for this phenomenon.

As will be discussed later (subsection 4.4.1), from the $I_d - V_g$ curves the transconductance of the FETs can be extracted.

4.3.2 Output Characteristic ($I_d - V_d$)

To obtain the curves of drain current versus drain voltage ($I_d - V_d$), drain voltage from 0V to +1V was applied for drain voltages 0V to 1V with a step of 0.2V. Moreover, to better understand

the different operation for gate voltage before and after the Dirac point ($V_{g,dirac}$), more detailed measurements (smaller step) around the $V_{g,dirac}$ were taken.

Figure 4.16 shows the characteristic $I_d - V_d$ curves for the FET 26_20 with the polymer chamber filled (0.3ml) with distilled water. Generally, excluding the curve for zero gate voltage, upon increase of the gate voltage the slope of the curve, which is equal to the conductivity, increases, i.e. the resistance decreases. This is expected, as the higher the gate voltage is, the greater the concentration of carriers at the graphene is and hence the more conductive it becomes.

More specifically, for different values of V_g different behaviors are observed: for $V_g = 0V$ the curve is convex, for $V_g = 0.2V$ the curve changes its curvature midpoint and for $V_g > 0.2V$ all curves have the same form (concave) and tend to reach a plateau. As the applied V_g increases the behavior of the device becomes more ohmic (more constant slope). The change in behavior of the curve from $V_g = 0.2V$ to $V_g = 0.4V$ indicates that the Dirac point is between these two values.

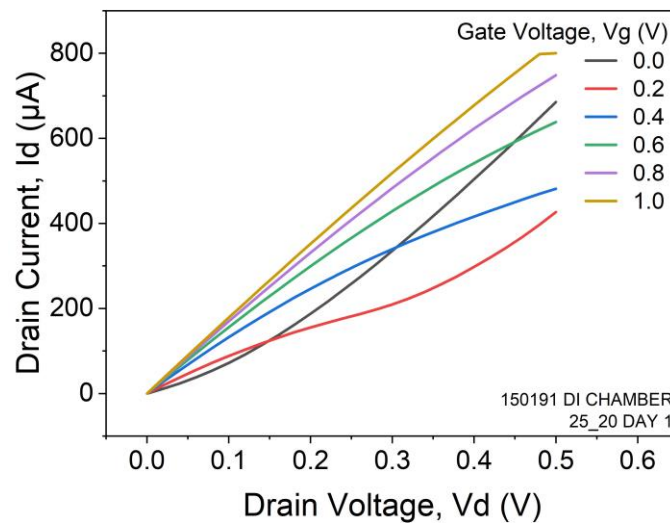


Figure 4.16: (a) $I_d - V_d$ for V_g from 0V to 1V for the FET 25_20 with the polymer chamber filled (0.3ml) with distilled water.

Figure 4.17 shows the different behavior for $V_g < V_{g,dirac}$ and for $V_g > V_{g,dirac}$. The voltage $V_{g,dirac} = 0.34V$ is the first at which the curve does not change curvature, so the Dirac point is between 0.32V and 0.34V. Also Figure 4.17.b indicates the 3 regions of operation of a GFET discussed in subsection 3.1.

4.3 Characteristic GFET curves

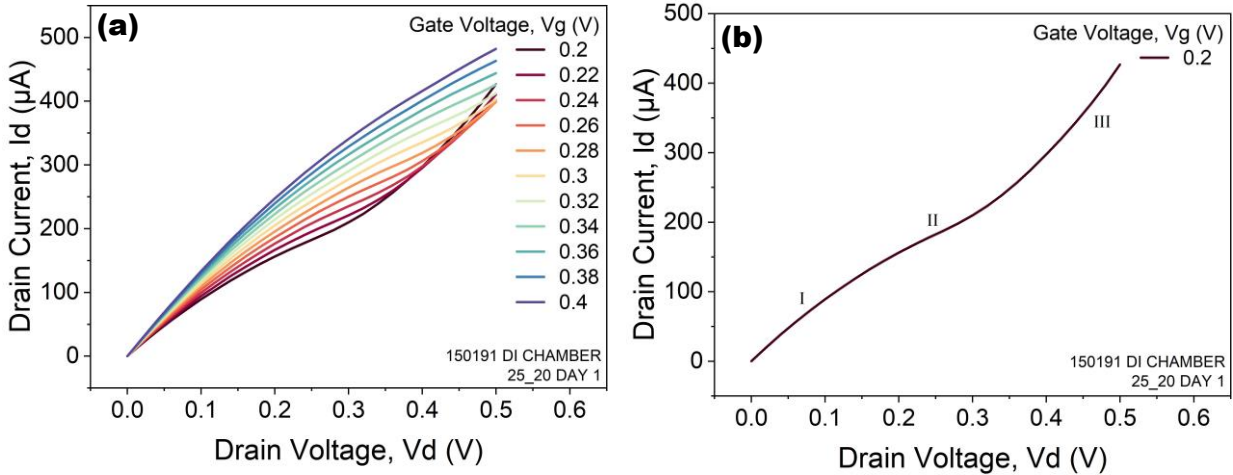


Figure 4.17: (a) $I_d - V_d$ curve for V_g around $V_{g,Dirac}$, (b) $I_d - V_d$ curve for $V_g = 0.2\text{V}$, where the 3 regions of operation of a GFET are shown: I) triode region, II) unipolar saturation region and III) ambipolar saturation region [24].

Figure 4.18 shows the curves $I_d - V_d$ for all FETs of the chip 15019. In theory all pairs should have the same behavior but variations during the fabrication process as well as any graphene wrinkles created during transfer cause different behavior from FET to FET of the same chip.

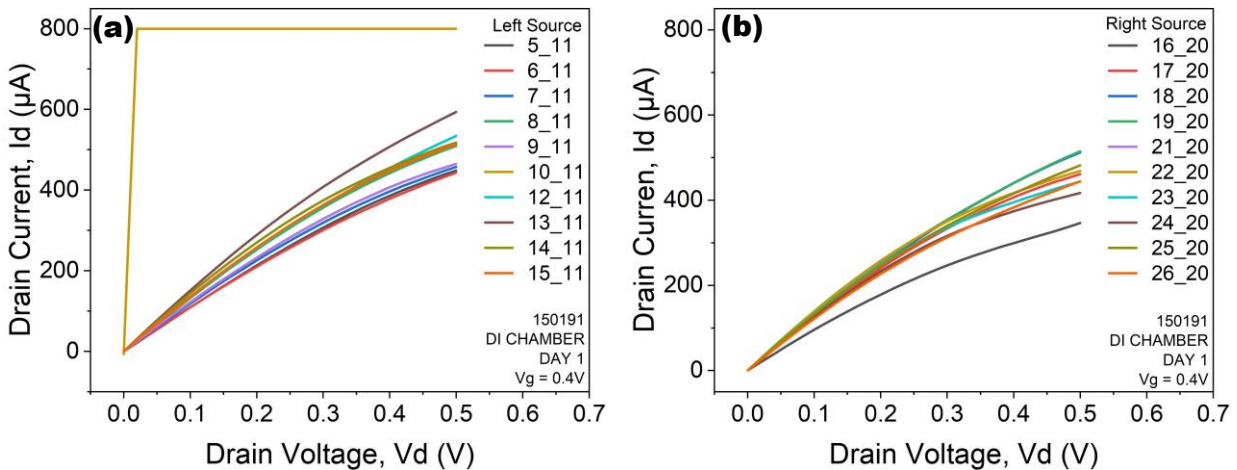


Figure 4.18: $I_d - V_d$ curves for $V_g = 0.4\text{V}$ for the left (a) and the right FETs (b) of the chip 15019.

As will be discussed later (subsection 4.4.1), from the $I_d - V_d$ curves the output conductance (g_d) of the FETs can be extracted.

4.3.3 Gate Leakage Current (I_g)

New effects that are typically not predicted in conventional back-gated or dielectric gated FET devices are introduced by the electrolyte-gated setup, such as low but always present gate/leakage currents (I_g). Both the transistor and the gate can be affected by the existence of gate currents in a

LG-FETs, so it is of high importance that they are monitored. Alongside of all the above measurements the leakage current was also measured to reassure proper functionality of the devices. Figure 4.19 and Figure 4.20 show the leakage current measured during the experiments of sections 4.3.1 and 4.3.2 accordingly. The gate current is significant smaller than the I_d current and into acceptable limits. During all the $I_d - V_g$ scans, the recorded I_g had a similar profile: it was negligible at low positive potentials but rapidly grew in magnitude when a specific gate potential was surpassed.

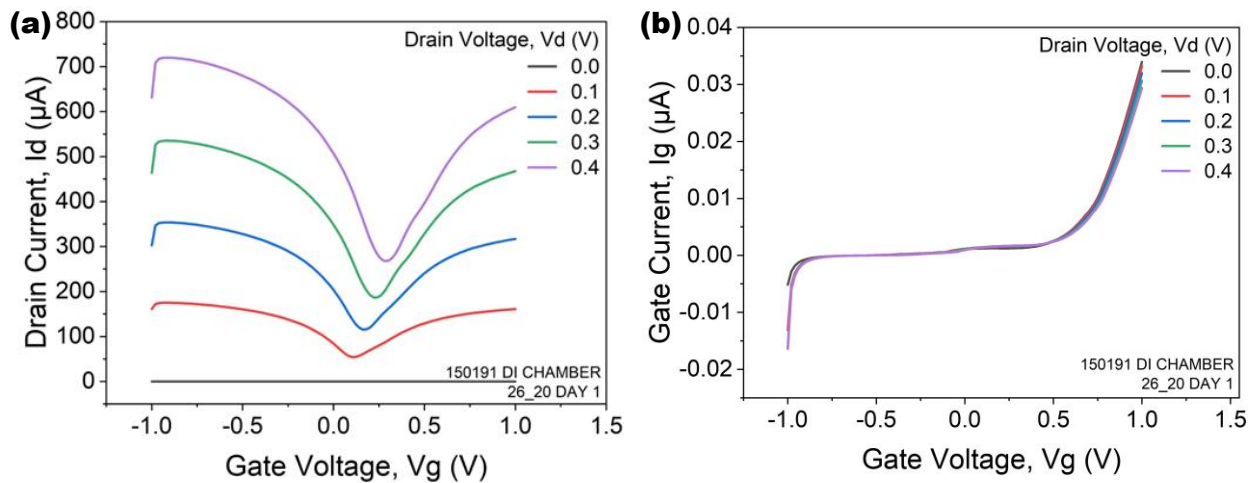


Figure 4.19: (a) $I_d - V_g$ curves for V_d from 0V to 0.4V for the FET 26_20 with the polymer chamber filled (0.3ml) with distilled water; (b) Leakage current during the same measurement

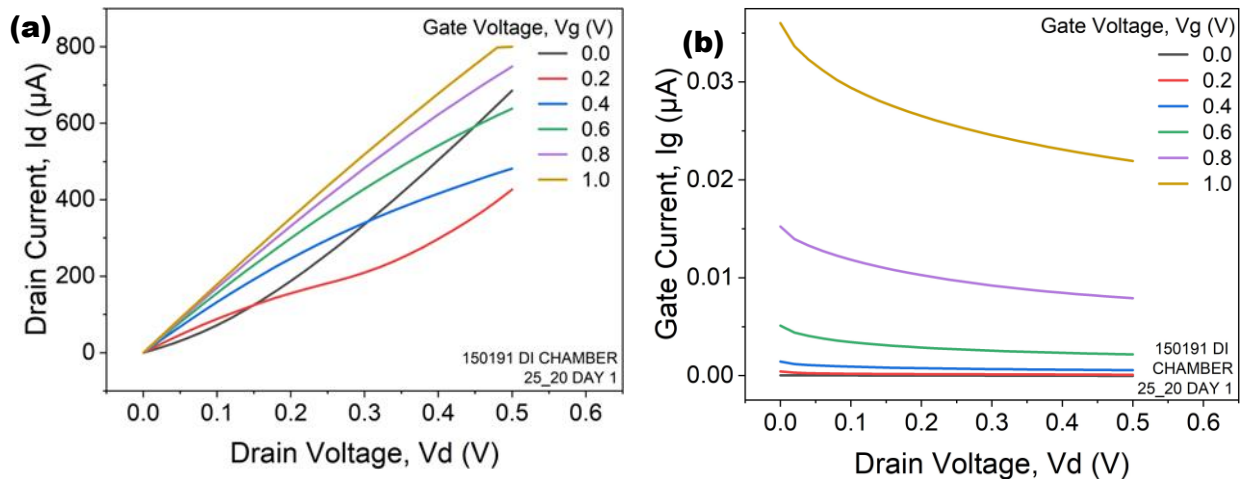


Figure 4.20: (a) $I_d - V_d$ for V_g from 0V to 1V for the FET 25_20 with the polymer chamber filled (0.3ml) with distilled water; (b) Leakage current during the same measurement

4.4 Parameter Extraction

This subchapter marks an important phase of the study, as it delves into the intricate process of parameter extraction from the $I_d - V_g$ and $I_d - V_d$ curves. This section directs its focus towards significant metrics of GFETs such as transconductance, carrier mobility, and carrier concentration. This section aims to provide a comprehensive understanding of the parameters of GFETs' functionality, laying the groundwork for subsequent discussions on optimization strategies and applications.

4.4.1 Transconductance (g_m^1)

Transconductance (also called transfer conductance) is the electrical characteristic that relates the output current to the input voltage of a device. It shows how much the output current (I_d in this work) changes regarding to variations of the input voltage (V_g in this work). It can be extracted from the plots of Figure 4.8 by applying the equation [51]:

$$g_m = \frac{dI_d}{dV_g} \quad (4.1)$$

To calculate the derivative, the *gradient* command of the *numpy*² library in *python*³ programming language was used. Based on the documentation of *numpy* the command *gradient*⁴ calculates the derivative based on Taylor series and concludes to the eq (4.2).

$$\hat{f}_i^{(1)} = \frac{f(x_i + 1) - f(x_i - 1)}{2h} + \mathcal{O}(h^2) \quad (4.2)$$

Figure 4.17 shows the transconductance curves of GFET 25_20 for different values of drain voltage (V_d). All curves have their minimum point at the Dirac point. To the left of the characteristics' peaks there is transconductance due to hole mobility and to the right transconductance due to electron mobility. These values will then be used to calculate the carrier mobility (subsection 4.4.5). Finally, on the right-hand side, after the peaks the curves make a "dent". This "dent" is due to the "break" of the $I_d - V_g$ curves (Figure 4.9).

¹ Transconductance is represented by m since it is also sometimes referred to as mutual conductance.

² <https://numpy.org/>

³ <https://www.python.org/>

⁴ <https://numpy.org/doc/stable/reference/generated/numpy.gradient.html>

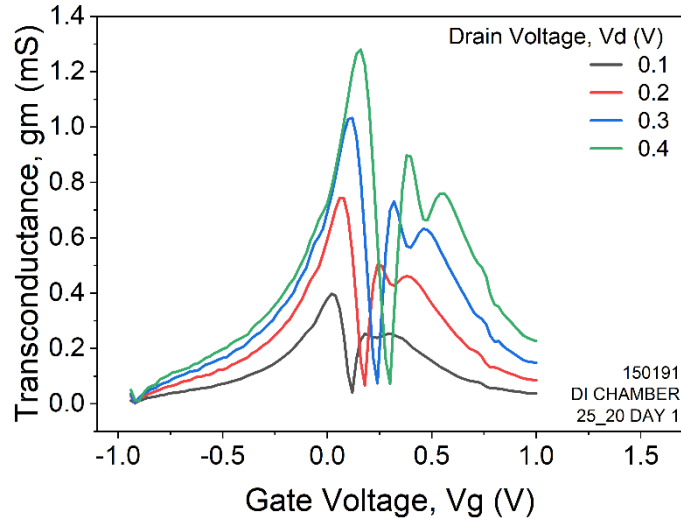


Figure 4.21: Transconductance curves of GFET 25_20 for different values of drain voltage (V_d).

4.4.2 Output Conductance (g_d)

The output conductance is a metric of how much the drain current changes in response to a change in drain voltage. Mathematically it can be derived from the curves in Figure 4.17 through eq. (4.3) [51].

$$g_d = \frac{dI_d}{dV_d} \quad (4.3)$$

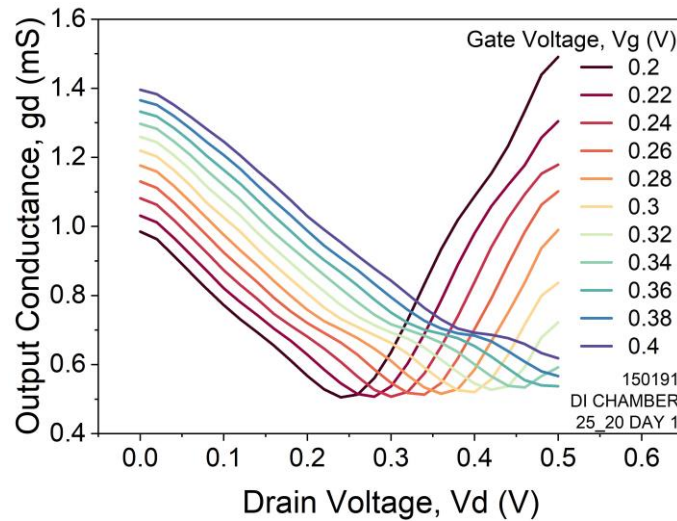


Figure 4.22: $g_d - V_d$ curve for V_g around $V_{g,Dirac}$

4.4.3 Conductance (G) and Resistance (R)

The resistance and conductance curves can also be derived from the $I_d - V_g$ curves (subchapter 4.3.1). The curves of the conductance versus gate voltage are shown in Figure 4.23. The conductivity is derived from the relation:

$$G = \frac{I_d}{V_d} \quad (4.4)$$

if applied to the curves in Figure 4.8.

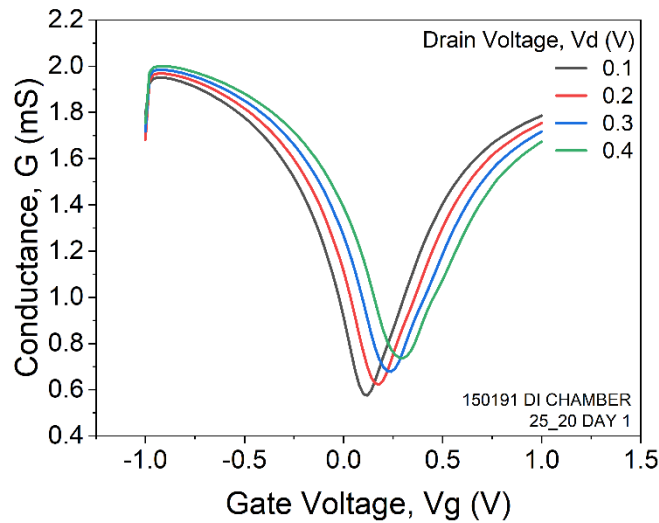


Figure 4.23: $G - V_g$ curves for V_d from 0V to 0.4V.

Similarly, the resistance versus gate voltage curves (Figure 4.24) are derived from the relation:

$$R = \frac{V_d}{I_d} \quad (4.5)$$

if applied to the curves in Figure 4.8. As the gate voltage gets closer to the gate voltage at the Dirac point, the resistance increases due to the decrease of carriers. Figure 4.24.b shows the resistance curves shifted to the left by $V_{g,dirac}$ and indicates that the resistance, in a range away from the $V_{g,dirac}$, does not depend on the applied drain voltage.

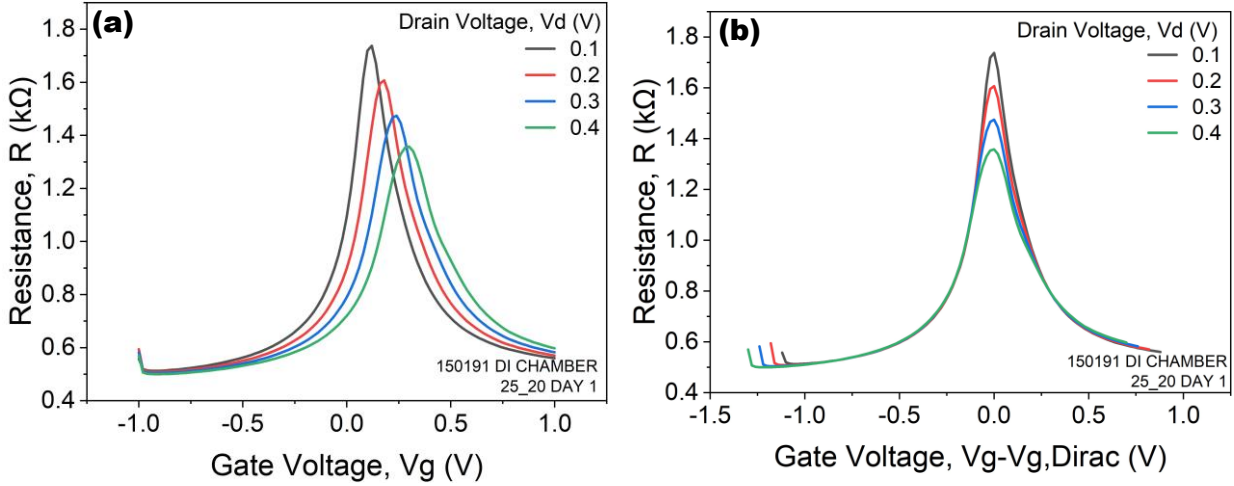


Figure 4.24: Resistance curves versus gate voltage (a) and versus gate voltage $-V_{g,Dirac}$ (b).

The resistance shown in Figure 4.24 is the “full” resistance of the device including the graphene resistance and the contact resistance. In more detail [34] the shown resistance is given by the relationship:

$$R_{tot} = R_{channel} + R_{contact} \quad (4.6)$$

where:

- $R_{channel}$: the resistance of graphene in the area covered by the top gate electrode,
- $R_{contact}$: the resistance of the graphene in the uncovered area plus the resistance of the contacts (graphene-contact interface). In the present arrangement there are 2 contacts and no uncovered graphene so $R_{contact} = 2R_c$, one R_c for each contact.

The resistance $R_{channel}$ is given by the relation:

$$R_{channel} = \frac{N_{sq}}{n_{tot} \cdot e \cdot \mu_{eff}} = \frac{N_{sq}}{\sqrt{n_0^2 + n[V_G^*]^2} \cdot e \cdot \mu_{eff}} \quad (4.7)$$

where:

- N_{sq} : number of squares in the top gated area ($N_{sq} = \text{lenght} / \text{width} = L/W$),
- n_{tot} : the carrier concentrations (electrons and holes) in the graphene channel

$$n_{tot} = \sqrt{n_0^2 + n[V_G^*]^2} \quad (4.8)$$

- e : the charge of electron,

- μ_{eff} : the effective mobility of the carriers,
- n_0 : the residual carrier concentration at the point of minimum conductivity (Dirac point),
- $n[V_G^*]$: the carrier concentration caused by the gate voltage ($V_G^* = V_G - V_{G,dirac}$).

The $n[V_G^*]$ is expressed from the relation:

$$V_G - V_{G,dirac} = \frac{e}{C_g} \mathbf{n} + \frac{\hbar \cdot u_F \cdot \sqrt{\pi \cdot \mathbf{n}}}{e} \quad (4.9)$$

where:

- C_g : the capacitance of the dielectric per surface area (the total capacity of the graphene – water),
- u_F : the Fermi velocity in graphene ($10^6 m/s$),
- \hbar : reduced planck constant.

Solving the eq. (4.9) in terms of \mathbf{n} it is concluded that:

$$\mathbf{n} = \left(\frac{-C_g \cdot \pi \cdot \hbar \cdot u_F / e^2 + \sqrt{C_g^2 \cdot \pi^2 \cdot \hbar^2 \cdot u_F^2 / e^4 - 4 \cdot \pi \cdot C_g \cdot (V_{G,dirac} - V_G) / e}}{2 \cdot \sqrt{\pi}} \right)^2 \quad (4.10)$$

So now by combining (4.9) and (4.10) a relationship $R_{tot} = f(V_G)$ can be derived and thus a fit to the experimental data (Figure 4.24.a) can be done to extract the constants R_C , μ and n_0 .

To make the fitting possible, the capacity C_g is left to be calculated. It is given by the relation:

$$C_g = C_{total} = [1/C_q + 1/C_{dl}]^{-1} \quad (4.11)$$

where:

- C_q : the quantum capacity per surface area due to changes in the total charge in the chemical potential (Fermi level, E_F) dQ/dE_F of the two-dimensional material,
- C_{dl} : the double layer capacitance of the graphene – electrolyte interface per surface area given by:

$$C_{dl} = \varepsilon_r \cdot \varepsilon_0 / \lambda_D \quad (4.12)$$

where:

- ε_r : the relative dielectric constant of the electrolyte,

- ϵ_0 : the dielectric constant of air,
- λ_D : the Debye length.

Table 4.1 contains the constants and the device characteristics used for the fit.

Table 4.1: Constants and device characteristics used for the fit of Figure 4.26.

Parameter	Parameter description	Value
L	graphene sheet length	$81 \cdot 10^{-6}m$
W	graphene sheet width	$25e \cdot 10^{-6}m$
ϵ_r	relative dielectric constant of the electrolyte	78.57
ϵ_0	dielectric constant of air	$8.85 \cdot 10^{-12} F/m$
λ_D	Debye length	$10^{-6}m$
C_q	quantum capacity per surface area	$2 \cdot 10^{-2} F/m^2$ [52] ¹

Based on the above values the capacity is calculated as $C_g = 1.36pF$. This value is confirmed experimentally as shown in Figure 4.25, from which we obtain $C_g \cong 1.35pF$. The capacitance has been measured in $1MHz$, as in this frequency the HP4284A LCR meter give very quick pulses and the measured capacitance is attributed only to effective agile electrons and not to slower traps that would have been measured if slower pulses were given.

¹ The C_q used in the present calculations is the minimum quantum capacity observed at the dirac point.

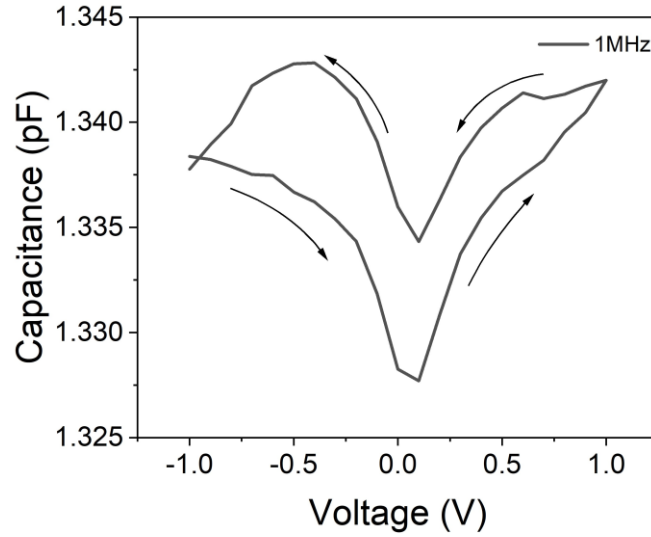


Figure 4.25: Experimental water – graphene capacitance curve as a function of voltage for frequency 1MHz.

Figure 4.26 shows the fit [33] of eq. (4.6) to the experimental data of the resistance curve versus the gate voltage.

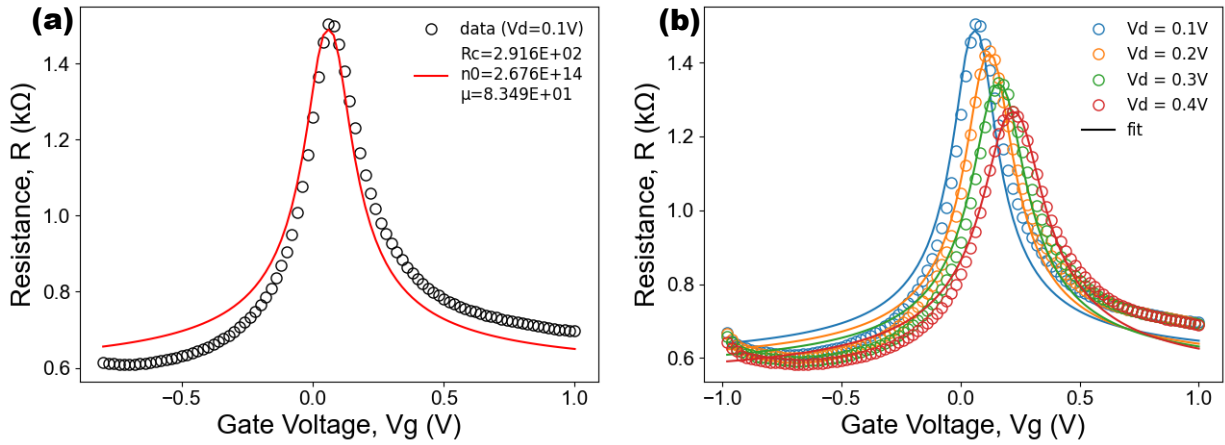


Figure 4.26: the fit [33] of eq. (4.6) to the experimental data of the resistance curve versus the gate voltage for (a) $V_d = 0.1V$ and (b) for all the measured drain voltages of the chip 150191 with the polymer chamber filled with water.

From the fits in Figure 4.26.b the parameters presented in Table 4.2 and Figure 4.27 are extracted.

Table 4.2: Extracted Parameters from the fit presented in the curves of Figure 4.26.b

$V_d(V)$	Contact Resistance – $R_C (\Omega)$	Residual Carrier Concentration – $n_0 (/m^2)$	Effective Mobility – $\mu_{eff} (m^2/Vs)$
0.1	290.2	$3.14 \cdot 10^{14}$	71.29

0.2	282	$3.48 \cdot 10^{14}$	67.79
0.3	274.4	$3.96 \cdot 10^{14}$	64.52
0.4	264.6	$4.62 \cdot 10^{14}$	59.41

The extracted parameters are also plotted, and a linear fit is used to extract a relation between each parameter and the applied drain voltage.

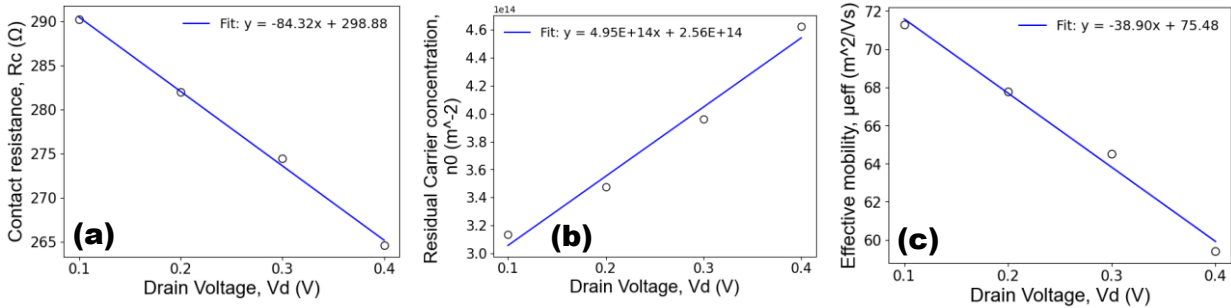


Figure 4.27: The extracted parameters versus drain voltage and a linear fit: (a) Contact resistance, (b) Residual carrier concentration and (c) effective mobility.

It is noticed that as the drain voltage increases the contact resistance and the effective mobility do not present important change while the residual carrier concentration increases as expected. The fact that the contact resistance and the effective mobility do not change indicates that there is no damage in the FET during these measurements.

These values are useful to calculate further characteristics of graphene such as the total carrier concentration (subchapter 4.4.4).

4.4.4 Carrier Concentration

From relation (4.10) the carrier concentration caused by the gate voltage can be derived as a function of the gate voltage. Since this is the carrier concentration of a two-dimensional material, it is measured in $carriers/m^2$ and not in $carriers/m^3$ which is done for three-dimensional materials. Figure 4.28.a shows the carrier concentration of graphene provoked by the applied gate voltage. It is observed that for a gate voltage equal to $V_{g,dirac}$ the carrier concentration is minimized. It is also noticed that the carrier concentration has a constant value, except for the voltage regions around $V_{g,dirac}$. Figure 4.28.b shows the total carrier concentration as obtained from relation (4.8) by substituting $n_0 = 2.67 \cdot 10^{14}/m^2$, that was obtained by the aforementioned

fitting (Figure 4.26). There is again a decrease in voltage but not as large since there is the remaining concentration n_0 .

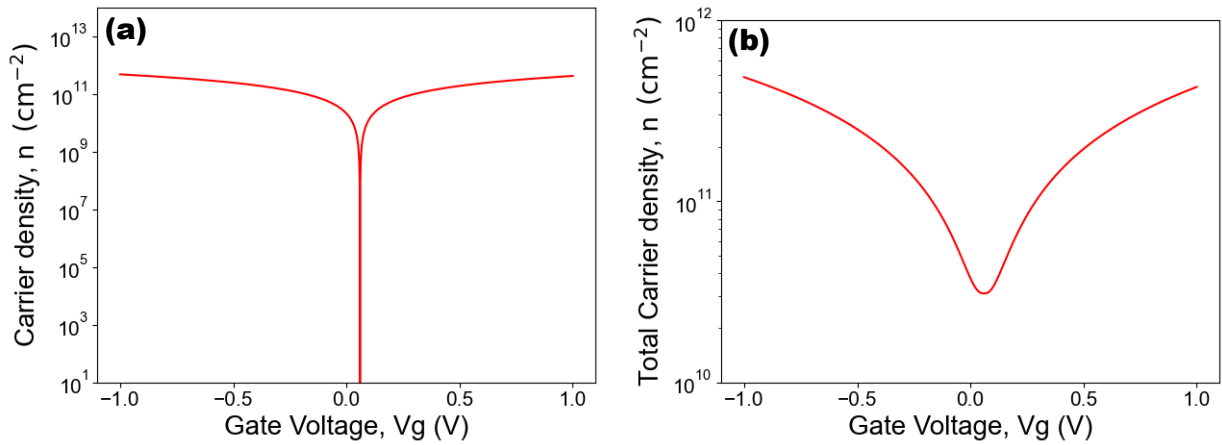


Figure 4.28: (a) carrier concentration of graphene due to the applied gate voltage, (b) total carrier concentration

4.4.5 Field Effect Mobility (μ_{fe})

In this subchapter the field effect mobility (μ_{fe}) will be analyzed. The μ_{fe} is extracted from the transconductance (g_m). In more detail [51]:

$$\mu_{fe} = \frac{L}{W} \cdot \frac{dI_d}{dV_G} \cdot \frac{1}{C_g} \quad (4.13)$$

where:

- C_g : the capacitance of the dielectric per surface area (eq. (4.11)).

Figure 4.29 shows the field effect mobility as a function of gate voltage. At the Dirac points the mobility is zero since there are no field effect carriers. It is also confirmed that the mobility of holes is higher than the mobility of electrons.

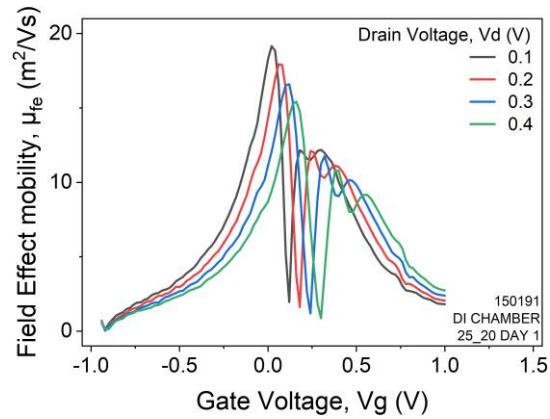


Figure 4.29: $\mu_{fe} - V_g$ curves

4.5 Measurement and time dependent behavior of GFETs

This section explores the behavior of GFET concerning exposure to ambient air and the number of measurements conducted. Initially, unused devices exhibit a suboptimal current response. However, with repeated voltage applications, their performance improves. Figure 4.30 illustrates the $I_d - V_g$ curves for iterative measurements on a first-time-used device, maintaining consistent experimental parameters. Initially, the curve is broader, but it gradually steepens after two voltage sweeps. Notably, after 2 to 3 sweeps, the curve stabilizes, indicating minimal further change. The initial slower response is attributed to organic residues from the fabrication process or ambient air pollutants, which form barriers. Several sweeps effectively “destroy” these barriers. This phenomenon aligns with observations documented in the literature [49], [50].

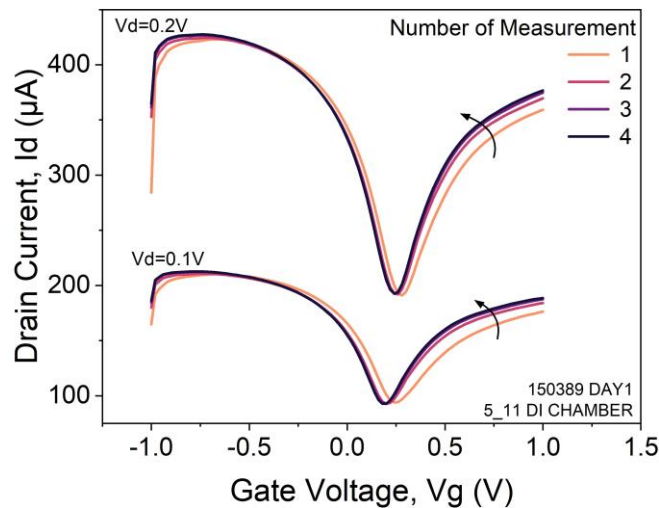


Figure 4.30: $I_d - V_g$ curves for recursive measurements in an unused device.

Moreover, after long lasting measurements a thin membrane is formed on top of the liquid used as top gate. After the removal of the water this membrane can adhere to the surface of the device and cause malfunctions. Figure 4.31.a shows the INL chip clean, before any measurements are executed. In contrast, Figure 4.31.b illustrates the presence of the under-discussion membrane on the device. This membrane initially causes operational issues, but it seems to “break” after some voltage sweeps. The corresponding behavior is depicted in Figure 4.33 and Figure 4.32.

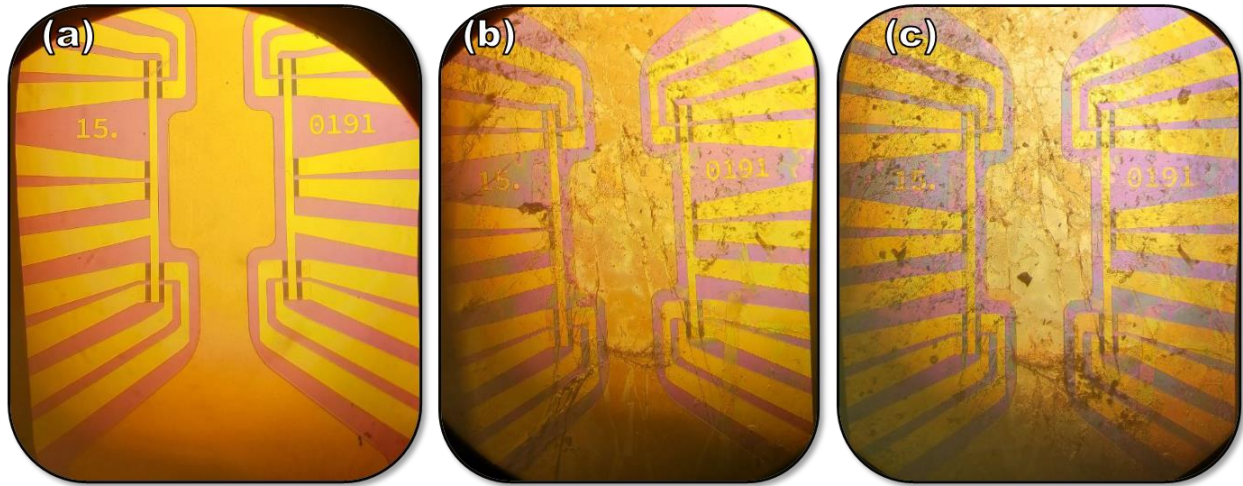


Figure 4.31: The under investigation device (a) before any measurements, (b) with the wet membrane right after measurements and removal of liquid and (c) with the dry membrane 1 day after the removal of the liquid.

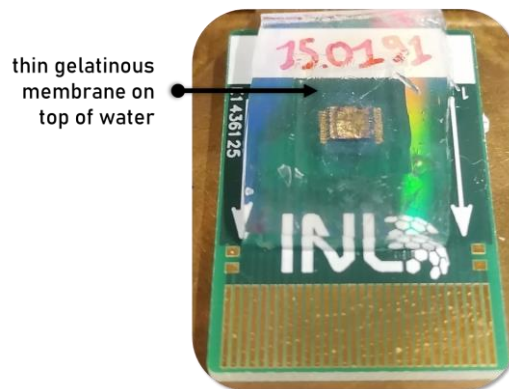


Figure 4.32: The gelatinous membrane is visible on top of the water

The $I_d - V_g$ curves, for the 5_11 device of the chip 150191, across six distinct temporal instances are illustrated in Figure 4.33. Instances 1.1 and 1.2 are derived from measurements taken on the same day. Instance 1.1 represents the initial curve, while Instance 1.2, which reflects conditions after water removal, is measured in the presence of the membrane shown in Figure 4.31.b. Notably, the appearance of this membrane causes a rightward shift of the Dirac point, indicative of the

introduction of positive charges to the graphene. Instance 2 corresponds to measurements conducted on the subsequent day, exhibiting a widened curve and a further rightward shift in the Dirac point, that may be attributed to the formation of a new membrane. Instances 3.1 and 3.2, acquired on the third day, have noteworthy points of difference: while 3.1, taken at the onset of measurements, demonstrates a significant shift and broadening of the curve, 3.2, obtained post-multiple voltage sweeps, demonstrates a restoration of the initial steep curve, suggesting a potential reversal effect achieved by the voltage sweeps. Finally, curve 4, captured on the fourth day of measurements, represents the latest temporal instance.

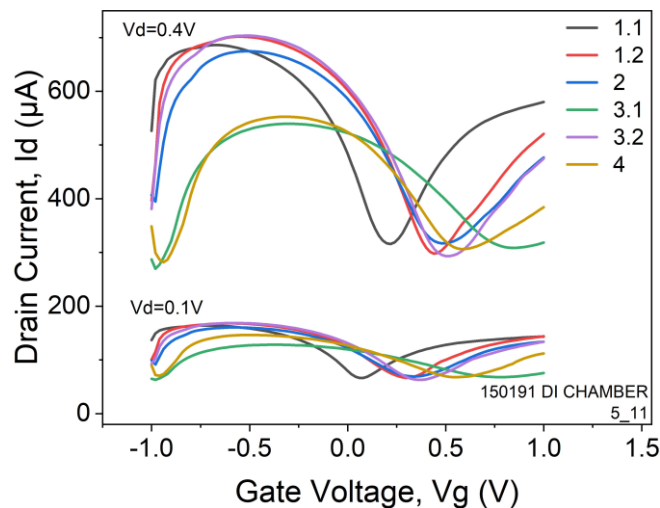


Figure 4.33: $I_d - V_g$ curves, for the 5_11 device of the chip 150191, across six distinct temporal instances. 1.1: start of day 1, 1.2: end of day 1, 2: start of day 2, 3.1: start of day 3, 3.2 end of day 3 and 4: start of day 4

With a closer look at the curves of Figure 4.33, it appears that the membrane adds positive charges to the graphene, causing a characteristic shift of the Dirac point. Although after multiple voltage sweeps the curve steepens again, it never comes back to the initial state. Notably, another intriguing phenomenon showcased in Figure 4.33 is the appearance of a second low point, occurring approximately at $V_g = -0.9V$, in curves 3.1 and 4.

Furthermore, the existence of the membrane causes a notable augmentation in the hysteresis phenomenon. In Figure 4.34 the hysteresis loops are presented both with and without the membrane. It is observed that the hysteresis is magnified by a factor of 3 to 4 with the inclusion of the membrane in contrast to the hysteresis observed in its absence. This phenomenon may be linked to the membrane's enhanced ability to entrap carriers originating from the water utilized as the liquid gate.

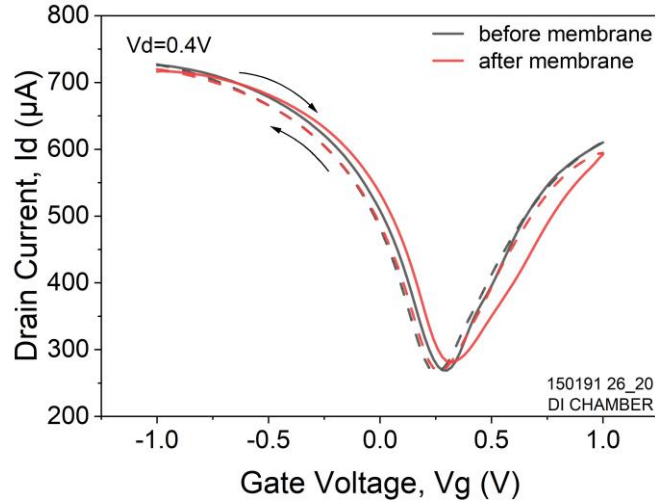


Figure 4.34: $I_d - V_g$ curves for forward (solid line) and backward sweep (dashed line)

Figure 4.35 comes in contrast to the above, as the curves of the device 26_20 of the same chip (150191) seem not to be affected by the formation of the membrane. This may be ascribed to the sequencing of measurements: device 26_20 was the final device to undergo measurement. Consequently, the multiple voltage sweeps conducted prior to its measurement may have effectively “break” the membrane barrier, thereby minimizing its influence by the time measurements were performed on device 26_20.

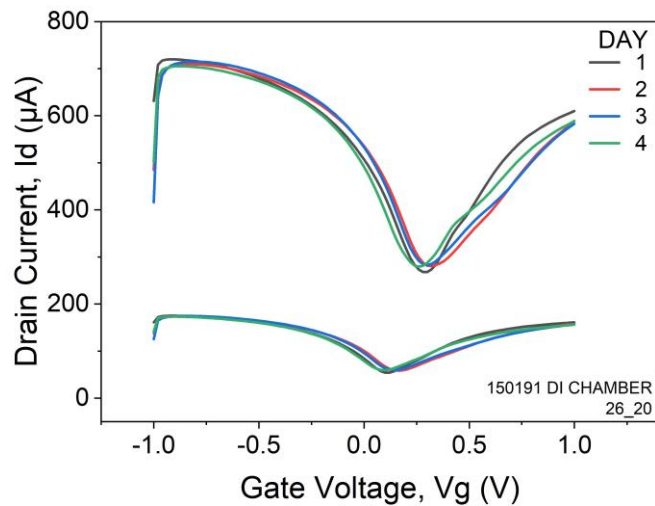


Figure 4.35: $I_d - V_g$ curves, for the 26_20 device of the chip 150191, across 4 days

5 Using the INL chip as a pH sensor

Demonstrating the applicability of the INL chip as a pH sensor constitutes a pivotal advancement for its use in biomedical applications. The discriminative ability of the INL chips to detect differences in pH underscores its ion-sensitivity and sets new basis to use this chip as biosensor.

5.1 pH sensing with LG-FETs

The conductivity of graphene in LG-FETs exhibits a dependency on the pH of the solution used as the gating medium. This phenomenon can be attributed to the fundamental principles of electrochemical equilibrium and the interaction between graphene and the surrounding electrolyte. When an aqueous solution is acidified the concentration of hydronium ions (H_3O^+) increases in accordance with the chemical equilibrium governing the dissolution of the acidic species. An example of this process can be observed in the reaction between hydrogen chloride (HCl) and water:



This equilibrium shift results in a higher density of mobile charge carriers within the solution. Consequently, when a gate voltage is applied, an increased population of charges accumulates at the interface between the electrolyte and the graphene surface. These additional ions effectively modulate the charge carrier density within the graphene channel and so increase its conductivity.

5.2 Experimental Process

Initially, three aqueous hydrogen chloride (HCl) solutions were prepared, exhibiting pH values of 3.4, 4.5, and 5.5. These solutions were derived through the process of dilution from a primary HCl solution characterized by a pH of 1. The dilution was made under continuous stirring and the pH was measured with a pH meter (Figure 5.1). So, by the end of this process, there were 4 solutions available: the 3 aforementioned solutions and the distilled water, the pH of which was measured to be 6.3.

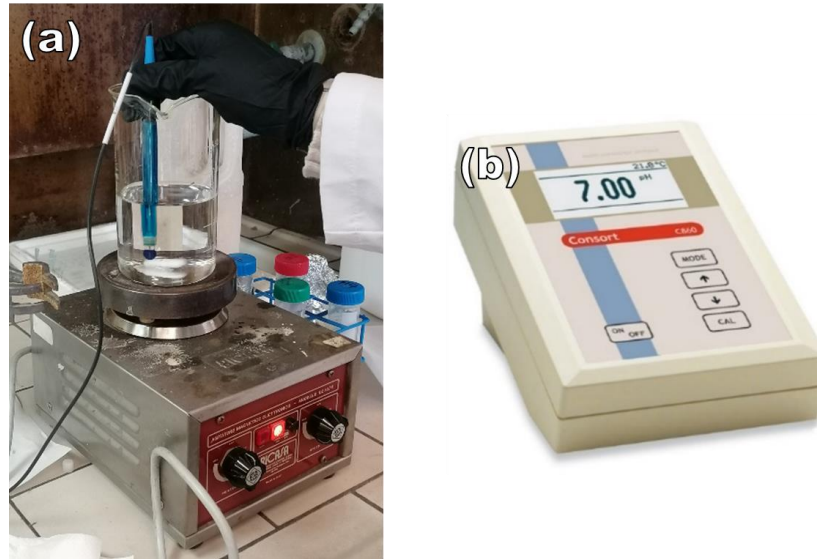


Figure 5.1: (a) Stirring equipment, (b) pH meter C860.

To notice the different response to different solution sampling measurements were executed. In more detail one drop of each solution was placed on top of the chip. The 3 probes were touching the drop (gate), the source and the drain. During the sampling the drain current was measured while a constant gate voltage, to accelerate the movement of the solution's carriers in the graphene's surface, and a drain bias voltage were applied. An important point of the experimental process is that the measurements started first from the solutions with bigger pH, because they have less carriers and therefore less of them would attach to the graphene. If the measurements started from more acid solutions, which are rich in carriers, some of them would adhere to the graphene's surface and the next measurements would be biased. To elaborate, the procedures were as follows:

1. New unused chip
2. For every solution (starting from solutions with bigger pH):
 - i. $I_d - V_g$ measurement for solution before the sampling
 - ii. Finding $V_{g,dirac}$ for certain $V_d = v$ ¹
 - iii. Sampling with solution under $V_g = V_{g,dirac}|_{V_d=v} + 0.1V$ and $V_d = v$
 - iv. $I_d - V_g$ measurement for solution after the sampling
 - v. Triple rinse the chip with distilled water

¹ Not all measurements were taken with the same V_d .

Before and after the sampling, photos were captured to observe any discrepancies associated with the time the solution remained on top of the graphene. Notably, it was found that if the solution stayed on top of the chip for more than 2-3 sampling measurements (each lasting about 10 minutes), the metals were etched, leading to destruction of the whole or the half chip. Such an example of electrochemical etching is shown on Figure 5.2.



Figure 5.2: Chip 150427 (a) before sampling measurements and (b) after sampling measurements, where the electrochemical etching is obvious in many spots.

Due to the above phenomenon, measurements with all the solutions on the same chip under the same conditions were not able. Therefore, the conductance (G) of the device is presented, as it is less biased by the applied drain voltage. To reduce any remaining bias from the drain voltage the conductance (from the initial $I_d - V_g$ curve) at $V_g = V_{g,1}$ and $V_d = V_{d,1}$, under which the sampling was executed, is subtracted. Finally, in order for the conductance to be normalized, it is divided by $G(V_{g,1}, V_{d,1})$ and so the presented data is $\frac{G(t) - G(V_{g,1}, V_{d,1})}{G(V_{g,1}, V_{d,1})}$. After the sampling measurements, the data are combined in Figure 5.3.

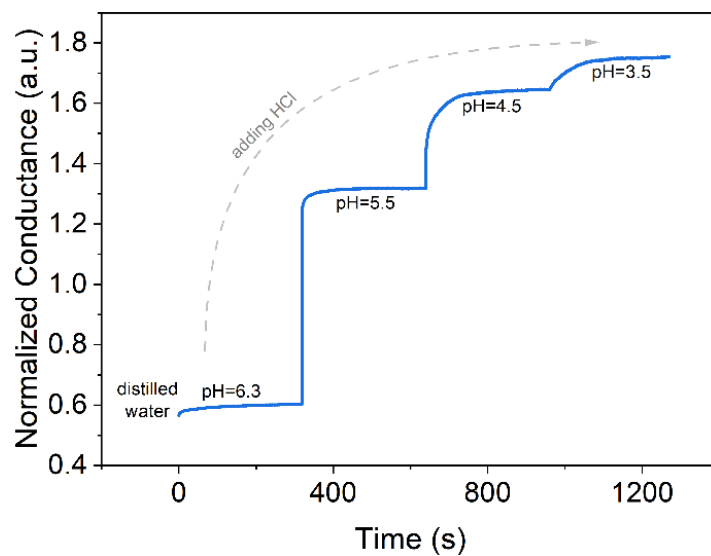


Figure 5.3: Normalized conductance versus time for solutions of different pH values

6 Cells Cultivation

After confirming the ion-sensitivity of the INL chips in subchapter 5.2, the focus now shifts to proving their biocompatibility. To accomplish this, Neuro-2A cells were cultured for 4 days and isolated neurons from the embryonic hippocampal region (E16.5) were cultivated for 10 days on top of graphene, which was transferred to 300nm SiO₂.

In more detail, Neuro-2A cells were cultivated in nutrient medium (DMEM-FBS 2%) supplemented with retinoic acid (10μM) for 4 days and their neural growth was evaluated. The cultivation was made on 5 samples to statistically study the growth of the neural cells. In the 4th day 46.28% of the cells had differentiated with an average neurite outgrowth¹ of 3.027μm. An example picture of the growing neurons is showed in Figure 6.1.

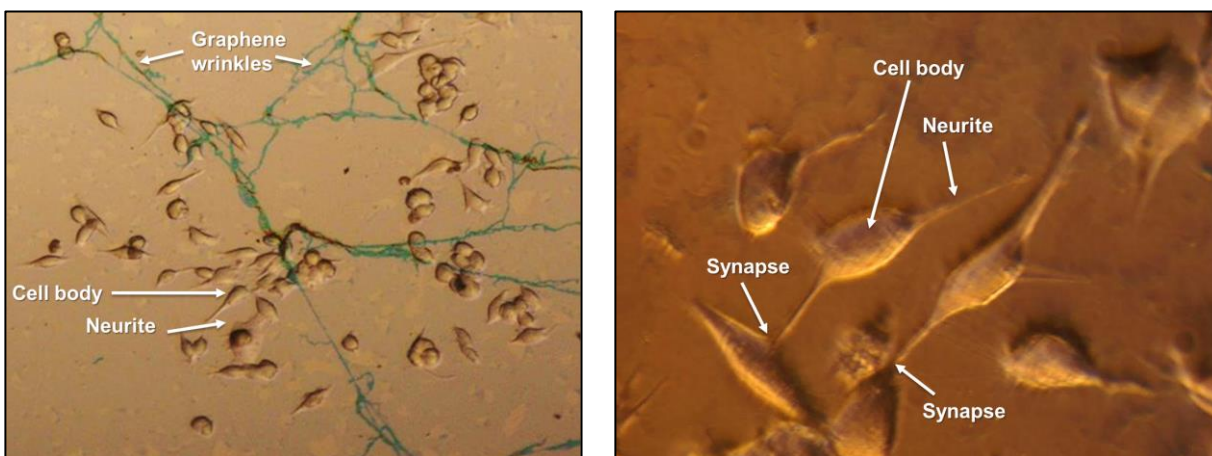


Figure 6.1: Optical microscope images from the cultivation of Neuro-2A cells on graphene

Additionally, isolated neurons from the embryonic hippocampal region were cultivated for 10 days (Figure 6.2). Primary hippocampal neuron cultures exhibited normal development on the graphene sample, confirming its potential as a medium for neuronal cell culture and differentiation. These experiments contribute crucial information towards establishing the biocompatibility of the INL chips, paving the way for their application in neurobiology and related fields.

¹ The neurite outgrowth is calculated by dividing the initial cell body diameter from the neurite grow length.

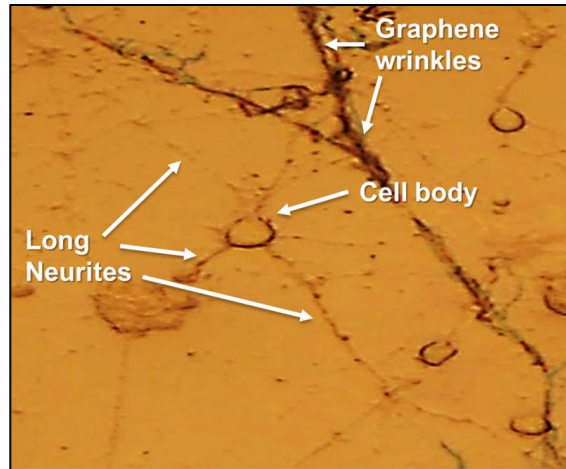


Figure 6.2: Optical microscope images from the cultivation of isolated neurons from the embryonic hippocampal region

7 Conclusions

The purpose of the current work was to electrically characterize arrays of liquid gate graphene field effect transistors. The transfer and output characteristics and proper parameter extraction techniques, like derivation and curve fitting, facilitated the extraction of valuable metrics – such as contact resistance, carrier concentration, effective mobility, and more – for the operation of the INL chips. Repeated measurements on all the LG-GFETs of many chips allowed the statistical assessment of the under-investigation devices and explored how they are affected from conditions, like remain humidity and atmosphere contamination. Moreover, measurements executed for aqueous solutions of different pH values, used as liquid gates, demonstrated a clear ion-sensitivity of LG-GFETs. Finally, the successful cultivation of cells on the graphene opens new paths for applications using this particular chip. The recording of nerve signals and the study of their effect on the characteristic curves is just examples of the research that could follow. The fact that there is an array of transistors and not a single device allows the elimination of noise as well as the simultaneous study of the behavior of the cells from different points.

However, during this work a few misses regarding the chip have been observed. First, the behavior of the LG-GFETs seems to vary a lot from chip to chip and also from FET to FET in the same chip. This does not allow for a coherent study as there is not a common ground when variables are changed. Additionally, the chips seem also to be really sensitive, even with distilled water, having a degrading effect over the span of just a few days. When they come in touch with more acid solutions, electrochemical etching is noticed, indicating poor passivation of the metals. Possible improvements would be, a better and more stable fabrication process, to eliminate variance, and a better more resistant passivation layer. The test of different materials for the coplanar top gate electrode, would also be a good suggestion, as the Au/Cr seem not to interact well with distilled water.

All in all, this work have set the basis for further research and many biomedical applications utilizing the LG-GFET array INL chip. Before use in application noise measurements and study, that are really important when dealing with sensing, should be executed.

Bibliography

- [1] A. K. Geim and K. S. Novoselov, “The rise of graphene.” [Online]. Available: www.nature.com/naturematerials
- [2] M. Terrones *et al.*, “Graphene and graphite nanoribbons: Morphology, properties, synthesis, defects and applications,” *Nano Today*, vol. 5, no. 4, pp. 351–372, Aug. 2010, doi: 10.1016/J.NANTOD.2010.06.010.
- [3] Z. Zhen and H. Zhu, “Structure and properties of graphene,” in *Graphene: Fabrication, Characterizations, Properties and Applications*, Elsevier, 2017, pp. 1–12. doi: 10.1016/B978-0-12-812651-6.00001-X.
- [4] C. Soldano, A. Mahmood, and E. Dujardin, “Production, properties and potential of graphene,” *Carbon*, vol. 48, no. 8, pp. 2127–2150, Jul. 2010. doi: 10.1016/j.carbon.2010.01.058.
- [5] X. Du *et al.*, “Graphene microelectrode arrays for neural activity detection,” *J Biol Phys*, vol. 41, no. 4, pp. 339–347, Sep. 2015, doi: 10.1007/s10867-015-9382-3.
- [6] M. Bramini *et al.*, “Interfacing graphene-based materials with neural cells,” *Front Syst Neurosci*, vol. 12, p. 358913, Apr. 2018, doi: 10.3389/FNSYS.2018.00012/BIBTEX.
- [7] L. H. Hess *et al.*, “Graphene transistor arrays for recording action potentials from electrogenic cells,” *Advanced Materials*, vol. 23, no. 43, pp. 5045–5049, Nov. 2011, doi: 10.1002/adma.201102990.
- [8] A. Armano and S. Agnello, “Two-Dimensional Carbon: A Review of Synthesis Methods, and Electronic, Optical, and Vibrational Properties of Single-Layer Graphene,” *C 2019, Vol. 5, Page 67*, vol. 5, no. 4, p. 67, Nov. 2019, doi: 10.3390/C5040067.
- [9] G. Yang, L. Li, W. B. Lee, and M. C. Ng, “Structure of graphene and its disorders: a review,” *Science and Technology of Advanced Materials*, vol. 19, no. 1. Taylor and Francis Ltd., pp. 613–648, Dec. 31, 2018. doi: 10.1080/14686996.2018.1494493.

- [10] S. M. M. Dubois, Z. Zanolli, X. Declerck, and J. C. Charlier, “Electronic properties and quantum transport in Graphene-based nanostructures,” in *European Physical Journal B*, Nov. 2009, pp. 1–24. doi: 10.1140/epjb/e2009-00327-8.
- [11] Edward McCann, “Electronic properties of monolayer and bilayer graphene,” in *Graphene Nanoelectronics*. [Online]. Available: <http://www.springer.com/series/3705/>
- [12] P. K. Misra, “Basic Properties of Crystals,” *Physics of Condensed Matter*, pp. 1–35, Jan. 2012, doi: 10.1016/B978-0-12-384954-0.00001-3.
- [13] E. Y. Andrei, G. Li, and X. Du, “Electronic properties of graphene: A perspective from scanning tunneling microscopy and magnetotransport,” *Reports on Progress in Physics*, vol. 75, no. 5. May 2012. doi: 10.1088/0034-4885/75/5/056501.
- [14] V. Berry, “Impermeability of graphene and its applications,” *Carbon N Y*, vol. 62, pp. 1–10, Oct. 2013, doi: 10.1016/J.CARBON.2013.05.052.
- [15] E. Pop, V. Varshney, and A. K. Roy, “Thermal properties of graphene: Fundamentals and applications,” *MRS Bull*, vol. 37, no. 12, pp. 1273–1281, Nov. 2012, doi: 10.1557/MRS.2012.203.
- [16] V. B. Mbayachi, E. Ndayiragije, T. Sammani, S. Taj, E. R. Mbuta, and A. ullah khan, “Graphene synthesis, characterization and its applications: A review,” *Results Chem*, vol. 3, p. 100163, Jan. 2021, doi: 10.1016/J.RECHEM.2021.100163.
- [17] K. C. Yung, W. M. Wu, M. P. Pierpoint, and F. V. Kusmartsev, “Introduction to Graphene Electronics -- A New Era of Digital Transistors and Devices,” *Contemp Phys*, vol. 54, no. 5, pp. 233–251, Sep. 2013, doi: 10.1080/00107514.2013.833701.
- [18] L. Sun *et al.*, “Chemical vapour deposition,” *Nature Reviews Methods Primers 2021 1:1*, vol. 1, no. 1, pp. 1–20, Jan. 2021, doi: 10.1038/s43586-020-00005-y.
- [19] D. Reddy, L. F. Register, G. D. Carpenter, and S. K. Banerjee, “Graphene field-effect transistors,” *Journal of Physics D: Applied Physics*, vol. 45, no. 1. Jan. 11, 2012. doi: 10.1088/0022-3727/45/1/019501.

-
- [20] K. S. Novoselov *et al.*, “Electric field effect in atomically thin carbon films,” *Science*, vol. 306, no. 5696, pp. 666–669, Oct. 2004, doi: 10.1126/SCIENCE.1102896.
- [21] M. C. Lemme, T. J. Echtermeyer, M. Baus, and H. Kurz, “A graphene field-effect device,” *IEEE Electron Device Letters*, vol. 28, no. 4, pp. 282–284, Apr. 2007, doi: 10.1109/LED.2007.891668.
- [22] F. Schwierz, “Graphene transistors,” *Nature Nanotechnology 2010 5:7*, vol. 5, no. 7, pp. 487–496, May 2010, doi: 10.1038/nnano.2010.89.
- [23] T. Manimekala, R. Sivasubramanian, and G. Dharmalingam, “Nanomaterial-Based Biosensors using Field-Effect Transistors: A Review,” *Journal of Electronic Materials 2022 51:5*, vol. 51, no. 5, pp. 1950–1973, Feb. 2022, doi: 10.1007/S11664-022-09492-Z.
- [24] I. J. Umoh, T. J. Kazmierski, and B. M. Al-Hashimi, “A dual-gate graphene FET model for circuit simulation - SPICE implementation,” *IEEE Trans Nanotechnol*, vol. 12, no. 3, pp. 427–435, 2013, doi: 10.1109/TNANO.2013.2253490.
- [25] I. Meric, M. Y. Han, A. F. Young, B. Ozyilmaz, P. Kim, and K. L. Shepard, “Current saturation in zero-bandgap, top-gated graphene field-effect transistors,” *Nature Nanotechnology 2008 3:11*, vol. 3, no. 11, pp. 654–659, Sep. 2008, doi: 10.1038/nnano.2008.268.
- [26] P. D. Cabral *et al.*, “Clean-Room Lithographical Processes for the Fabrication of Graphene Biosensors,” *Materials 2020, Vol. 13, Page 5728*, vol. 13, no. 24, p. 5728, Dec. 2020, doi: 10.3390/MA13245728.
- [27] R. Forsyth, A. Devadoss, and O. J. Guy, “Graphene Field Effect Transistors for Biomedical Applications: Current Status and Future Prospects,” *Diagnostics 2017, Vol. 7, Page 45*, vol. 7, no. 3, p. 45, Jul. 2017, doi: 10.3390/DIAGNOSTICS7030045.
- [28] L. Lozano-Chamizo *et al.*, “High enhancement of sensitivity and reproducibility in label-free SARS-CoV-2 detection with graphene field-effect transistor sensors through precise surface biofunctionalization control,” *Biosens Bioelectron*, vol. 250, p. 116040, Apr. 2024, doi: 10.1016/J.BIOS.2024.116040.

- [29] W. Fu, L. Jiang, E. P. van Geest, L. M. C. Lima, and G. F. Schneider, “Sensing at the Surface of Graphene Field-Effect Transistors,” *Adv Mater*, vol. 29, no. 6, Feb. 2017, doi: 10.1002/ADMA.201603610.
- [30] C. Reiner-Rozman, M. Larisika, C. Nowak, and W. Knoll, “Graphene-based liquid-gated field effect transistor for biosensing: Theory and experiments,” *Biosens Bioelectron*, vol. 70, pp. 21–27, Aug. 2015, doi: 10.1016/j.bios.2015.03.013.
- [31] E. Masvidal-Codina *et al.*, “High-resolution mapping of infraslow cortical brain activity enabled by graphene microtransistors,” *Nature Materials 2018 18:3*, vol. 18, no. 3, pp. 280–288, Dec. 2018, doi: 10.1038/s41563-018-0249-4.
- [32] B. M. Blaschke *et al.*, “Mapping brain activity with flexible graphene micro-transistors,” *2d Mater*, vol. 4, no. 2, Jun. 2017, doi: 10.1088/2053-1583/aa5eff.
- [33] A. D. Smith, S. Vaziri, S. Rodriguez, M. Östling, and M. C. Lemme, “Large Scale Integration of Graphene Transistors for Potential Applications in the Back End of the Line.” [Online]. Available: <http://www.graphenea.com/>
- [34] S. Kim *et al.*, “Realization of a high mobility dual-gated graphene field-effect transistor with Al₂O₃ dielectric,” *Appl Phys Lett*, vol. 94, no. 6, 2009, doi: 10.1063/1.3077021.
- [35] J. B. Oostinga, H. B. Heersche, X. Liu, A. F. Morpurgo, and L. M. K. Vandersypen, “Gate-induced insulating state in bilayer graphene devices,” *Nature Materials 2007 7:2*, vol. 7, no. 2, pp. 151–157, Dec. 2007, doi: 10.1038/nmat2082.
- [36] A. A. Balandin, “Thermal properties of graphene and nanostructured carbon materials,” *Nature Materials 2011 10:8*, vol. 10, no. 8, pp. 569–581, Jul. 2011, doi: 10.1038/nmat3064.
- [37] J. S. Bunch *et al.*, “Electromechanical resonators from graphene sheets,” *Science*, vol. 315, no. 5811, pp. 490–493, Jan. 2007, doi: 10.1126/SCIENCE.1136836.
- [38] C. Lee, X. Wei, J. W. Kysar, and J. Hone, “Measurement of the elastic properties and intrinsic strength of monolayer graphene,” *Science*, vol. 321, no. 5887, pp. 385–388, Jul. 2008, doi: 10.1126/SCIENCE.1157996.

- [39] R. R. Nair *et al.*, “Fine structure constant defines visual transparency of graphene,” *Science* (1979), vol. 320, no. 5881, p. 1308, Jun. 2008, doi: 10.1126/SCIENCE.1156965/SUPPL_FILE/NAIR.SOM.PDF.
- [40] G. Eda, G. Fanchini, and M. Chhowalla, “Large-area ultrathin films of reduced graphene oxide as a transparent and flexible electronic material,” *Nature Nanotechnology* 2008 3:5, vol. 3, no. 5, pp. 270–274, Apr. 2008, doi: 10.1038/nnano.2008.83.
- [41] N. A. A. Ghany, S. A. Elsherif, and H. T. Handal, “Revolution of Graphene for different applications: State-of-the-art,” *Surfaces and Interfaces*, vol. 9, pp. 93–106, Dec. 2017, doi: 10.1016/J.SURFIN.2017.08.004.
- [42] C. Casiraghi *et al.*, “Rayleigh imaging of graphene and graphene layers,” *Nano Lett*, vol. 7, no. 9, pp. 2711–2717, Sep. 2007, doi: 10.1021/NL071168M/ASSET/IMAGES/LARGE/NL071168MF00009.JPEG.
- [43] M. Gülcan, A. Aygün, F. Almousa, H. Burhan, A. Khan, and F. Şen, “Graphene Functionalizations on Copper by Spectroscopic Techniques,” *Carbon Nanostructures*, pp. 313–333, 2019, doi: 10.1007/978-981-32-9057-0_13/COVER.
- [44] K. E. Whitener and P. E. Sheehan, “Graphene synthesis,” *Diam Relat Mater*, vol. 46, pp. 25–34, Jun. 2014, doi: 10.1016/J.DIAMOND.2014.04.006.
- [45] Adel S. Sedra and Kenneth C. Smith, *Microelectronic Circuits*. Oxford University Press, 2004.
- [46] R. Campos *et al.*, “Attomolar label-free detection of dna hybridization with electrolyte-gated graphene field-effect transistors,” *ACS Sens*, vol. 4, no. 2, pp. 286–293, Feb. 2019, doi: 10.1021/ACSSENSORS.8B00344/ASSET/IMAGES/LARGE/SE-2018-003448_0004.JPEG.
- [47] M. P. Wolf, G. B. Salieb-Beugelaar, and P. Hunziker, “PDMS with designer functionalities—Properties, modifications strategies, and applications,” *Prog Polym Sci*, vol. 83, pp. 97–134, Aug. 2018, doi: 10.1016/J.PROGPOLYMSCI.2018.06.001.

- [48] K. Nagashio and A. Toriumi, “Density-of-states limited contact resistance in graphene field-effect transistors,” *Jpn J Appl Phys*, vol. 50, no. 7 PART 1, Jul. 2011, doi: 10.1143/JJAP.50.070108.
- [49] P. L. Levesque *et al.*, “Probing charge transfer at surfaces using graphene transistors,” *Nano Lett*, vol. 11, no. 1, pp. 132–137, Jan. 2011, doi: 10.1021/nl103015w.
- [50] A. Svetlova, D. Kireev, G. Beltramo, D. Mayer, and A. Offenhäusser, “Origins of Leakage Currents on Electrolyte-Gated Graphene Field-Effect Transistors,” *ACS Appl Electron Mater*, vol. 3, no. 12, pp. 5355–5364, Dec. 2021, doi: 10.1021/ACSAELM.1C00854/SUPPL_FILE/EL1C00854_SI_001.PDF.
- [51] D. K. Schroder, “Semiconductor Material and Device Characterization: Third Edition,” *Semiconductor Material and Device Characterization: Third Edition*, pp. 1–779, Apr. 2005, doi: 10.1002/0471749095.
- [52] M. V. Cheremisin, “Quantum capacitance of the monolayer graphene,” *Physica E Low Dimens Syst Nanostruct*, vol. 69, pp. 153–158, 2015, doi: 10.1016/j.physe.2015.01.018.